STRIATAL PLASTICITY UPON LEARNING OF A LATERALIZED MOTOR TASK

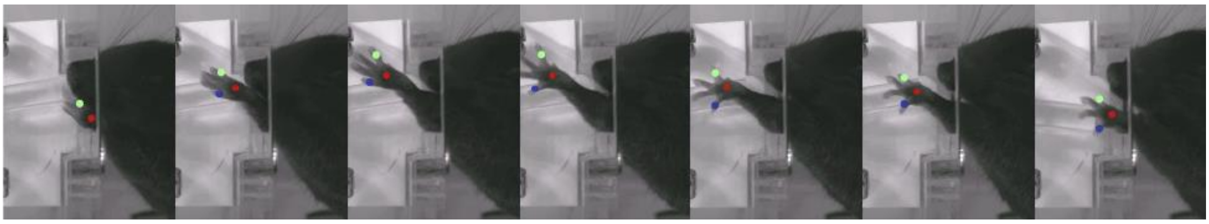

ANA MARGARIDA MARQUES PINTO

A dissertation submitted in partial fulfillment of the requirements for the Degree of Master's in Biomedical Research

Dissertação para obtenção do grau de Mestre em Investigação Biomédica

At Faculdade de Ciências Médicas | NOVA Medical School of NOVA University of Lisbon

February 2021

STRIATAL PLASTICITY UPON LEARNING OF A LATERALIZED MOTOR TASK

Ana Margarida Marques Pinto

Supervisors: Daniela Pereira, PhD; Rui M. Costa, DVM, PhD

Internal co-supervisor: Rita Teodoro, PhD

A dissertation submitted in partial fulfillment of the requirements for the Degree of Master's in Biomedical Research

Dissertação para obtenção do grau de Mestre em Investigação Biomédica

February 2021

Cover image: Video frames of a mouse pressing a lever during a motor task. Videos were labeled for different parts of the mouse paw (represented in green, red and blue).

Imagem de capa: *Frames* de vídeo de um ratinho pressionando uma alavanca durante uma tarefa motora. Os vídeos foram marcados para diferentes partes da pata do ratinho (representadas a verde, vermelho e azul).

Acknowledgments

First, I would like to stress my gratitude to my supervisors, Daniela Pereira, and Rui Costa. You welcomed me into the lab, where I have found not only great science but great individuals as well. This combination makes it feel exciting to come every single day to the lab. With both, I have learned a lot about science and how to do science. Thank you, Rui, for the great leadership of this team which I am truly grateful for having been a part of. I will always cherish your words of reassurance and exciting discussions with the lab. Thank you, Daniela, for trusting me with the development of a new and ambitious project, from which I have learned a lot. You mentored me at every step along the way, and never discouraged my ideas. I am truly lucky to have found a supervisor like you (you have raised the bar high!). I will be forever thankful for not only your exceptional mentorship and all that you have taught me, but also for our friendship.

I want to thank all the Costa lab members that I have had the privilege to work with and learnt from. It is truly an honor to be surrounded and inspired by such great scientists. A special and big thank you Marcelo Mendonça, for being an unofficial supervisor and guiding me through the world of behavior. Thank you for your mentorship. *Gracias* Cristina, for your expertise and kindness. Thanks to Catarina, for taking care of our mice. Thanks to the other master students in the lab, Tatiana, Rodrigo, and Ana, for everything we have learned and laughed at together. I also want to acknowledge our tiny helpers of science, the mice, for which I have great respect and dearly appreciate for allowing me to learn more about the brain.

I would like to acknowledge the Champalimaud Research community for having such a prosperous environment. A special thanks to all the support platforms that have provided expertise and training crucial for this work, and in particular the Microscopy platform - Anna, Leonor, and Davide. Thank you to Alex, for your friendship and crucial IT help. Thank you, Margarida, for the many shared breaks and nights of work at CCU.

Thank you, NOVA Medical School, NBR teachers and colleagues, for this great opportunity of personal and academic growth. A special thanks to Rita Teodoro, not only for being my internal supervisor but also a truly inspiring scientist and teacher. Thank you to Cláudia Almeida, for your mentorship and our exciting discussions about science.

There is a big list of people that would deserve an individual mention here, from friends to family and previous mentors, and for which I am extremely grateful for being or having been part of my life and who I am today. Your presence and contribution in my life, and by extent to this work, are appreciated. Thank you sincerely to each one of you.

For the big finale, I would like to acknowledge and thank my family, for the unconditional support and love. If anything, this thesis is the work of my parents, Isabel and Orlando. Thank you for raising me wholeheartedly, and for giving me and my sisters all the love and the best opportunities you can. I am eternally grateful for your support throughout my entire education path and life. Thank you for always having my back. Thank you to my sisters, Filipa and Matilde, for being a source of motivation and love. I hope this thesis serves as an inspiration for your future studies, in which I am sure you will both outstand me. Thank you to my other half, Lucas, for sharing your life with me, for the inspiration and creativity, and for everything you are. I hope we can continue to grow together and nurture each other. I am truly grateful for having my family and would not pick any other people to share my life with. *Obrigada por tudo, do fundo do coração*. I love you all and dedicate this thesis to you.

Financial Support

All the required financial support in order to perform all experimental and complementary work for the project entitled "Striatal plasticity upon learning of a lateralized motor task" was provided by the Neurobiology of Action laboratory, using funds from internal (Champalimaud Foundation) sources.

Champalimaud Foundation

Abstract

The basal ganglia circuits are critically involved in the acquisition, learning and consolidation of motor skills. The striatum is the major input region of the basal ganglia and is mainly composed of medium spiny neurons (MSNs). MSN dendritic spines represent a major site of synaptic plasticity in the basal ganglia. While MSN functional synaptic plasticity has been shown to occur in the context of motor learning, it remains unknown whether it is accompanied by structural plasticity, i.e., by changes in the number, size and/or spatial pattern of dendritic spines.

In this study, we aimed to characterize motor performance and striatal activity upon motor skill learning, with the ultimate goal of studying structural plasticity upon motor learning. We trained mice in a self-paced operant task where a reward is obtained after pressing a lever four times. As training progresses, the position and retractability of the lever impose laterality, allowing the study of movement sequences performed by a single forelimb. During training, mice improved their performance and learned to perform the task with only one forepaw, increasing the total number of lever presses per minute and organizing their behavior in sequences of lever presses. Using video-based paw trajectory detection, we further dissected movement kinematics during task learning, and found that paw trajectory variability during lever press did not significantly decrease throughout training.

To identify cells that were active in the last session of the motor task, and therefore more likely to have undergone synaptic plasticity, we performed immunostaining against c-Fos, an immediate early gene commonly used as a neuronal plasticity marker. Using a whole-brain cell detection pipeline, we were able to achieve unbiased cell detection and atlas mapping of c-Fos expressing cells, using fixed brain slices of mice sacrificed 1h after the last training session. Our preliminary results suggest that task-trained animals have subtle changes in c-Fos expression in the contralateral hemisphere to the trained paw. These changes appeared to be consistent across regions involved in motor learning and performance in task-trained animals that include the striatum, primary motor cortex layer 5, and upper limb region of the primary somatosensory cortex.

Finally, we sought to establish the tools and techniques needed to study structural plasticity in fixed brain slices. We optimized a novel viral approach to achieve sparse labelling of MSNs, allowing the visualization and reconstruction of the whole dendritic arbor of single MSNs, including dendritic spines. Using high-resolution confocal microscopy, together with deconvolution and spine analysis software, we were able to image and reconstruct MSN dendritic spines and characterize spine morphology. We found that D1-MSNs have a preponderance of mushroom spines, followed by thin and stubby spines, with filopodia making up just a small fraction of overall dendritic protrusions.

Our work has established the basic techniques and methodologies that will allow future studies on dendritic spine density, volume and distribution in neurons that recently underwent plasticity upon motor learning. Those experiments will, in turn, advance our understanding of how MSN input computation changes during motor learning, with important implications for the study and treatment of movement disorders.

Resumo

Os circuitos dos núcleos da base estão crucialmente envolvidos na aquisição, aprendizagem e consolidação de habilidades motoras. O corpo estriado é a principal região de *input* dos núcleos da base e é composto principalmente por neurónios médios do estriado (*medium spiny neurons*, MSNs). As espículas dendríticas dos MSNs representam um importante local de plasticidade sináptica nos núcleos da base. Embora tenha sido demonstrado que a plasticidade sináptica funcional do MSN ocorre num contexto de aprendizagem motora, não se sabe se esta é acompanhada por plasticidade estrutural, ou seja, por mudanças no número, tamanho e/ou padrão espacial das espículas dendríticas.

Neste estudo, o nosso objetivo consistiu em caracterizar o desempenho motor e a atividade do corpo estriado na aprendizagem de habilidades motoras, com o objetivo final de estudar a plasticidade estrutural na aprendizagem motora. Treinamos ratinhos numa tarefa operante individualizada, em que uma recompensa é obtida após pressionar uma alavanca quatro vezes. À medida que o treino avança, a posição e retração da alavanca impõem lateralidade, permitindo o estudo das sequências de movimento realizadas por um único membro anterior. Durante o treino, os ratinhos melhoraram o seu desempenho e aprenderam a realizar a tarefa com apenas uma das patas dianteiras, aumentando o número total de movimentos de pressão sobre a alavanca por minuto e organizando o comportamento em sequências de movimentos. Através da deteção da trajetória da pata baseada em vídeo, examinamos ainda mais a cinemática do movimento durante a aprendizagem da tarefa e descobrimos que a variabilidade da trajetória da pata durante a pressão sobre a alavanca não diminuiu significativamente durante o treino.

Para identificar as células que estiveram ativas na última sessão da tarefa motora e, portanto, com maior probabilidade de terem sofrido plasticidade sináptica, realizamos uma imunohistoquímica contra c-Fos, um gene de expressão rápida frequentemente usado como marcador de plasticidade neuronal. Usando um *pipeline* de deteção de células no cérebro inteiro, conseguimos detetar células que expressam c-Fos e mapeá-las no atlas de uma maneira imparcial, usando fatias de cérebro fixadas de ratinhos sacrificados 1h após a última sessão de treino. Os nossos resultados preliminares sugerem que animais treinados na tarefa apresentam mudanças ligeiras na expressão de c-Fos no hemisfério contralateral à pata treinada. Estas mudanças parecem ser consistentes em regiões envolvidas na aprendizagem e desempenho motor nos animais treinados, e incluem o corpo estriado, a camada 5 do córtex motor primário e a região do membro superior do córtex somatossensorial primário.

Finalmente, procuramos estabelecer as ferramentas e técnicas necessárias para estudar a plasticidade estrutural em fatias fixadas do cérebro. Otimizamos uma nova abordagem viral para obter uma marcação pouco densa de MSNs, permitindo a visualização e reconstrução de toda a árvore dendrítica de MSNs individuais, incluindo espículas dendríticas. Usando microscopia confocal de alta resolução, em conjunto com softwares de deconvolução e análise de espículas dendríticas, adquirirmos imagens e reconstruimos as espículas dendríticas do MSN e caracterizamos a morfologia das mesmas. Descobrimos que os D1-MSNs têm uma preponderância de espículas do tipo *mushroom*, seguidas por espículas do tipo *thin* e *stubby*, com os *filopodia* constituindo apenas uma pequena fração do número total das protuberâncias dendríticas.

O nosso trabalho estabeleceu as técnicas e metodologias básicas que permitirão estudos futuros sobre a densidade, volume e distribuição das espículas dendríticas em neurónios que recentemente sofreram plasticidade após aprendizagem motora. Essas experiências, por sua vez, irão avançar a nossa compreensão de como a computação de *inputs* pelos MSNs muda durante a aprendizagem motora, com implicações importantes para o estudo e tratamento de doenças motoras.

List of contents

List of tables and figures

Figures

Tables

Abbreviations

3D: three-dimensional
A2A: Adora2a
AAV: Adeno-associated virus
ACC: Anterior cingulate cortex
AMPA: α-amino-3-hydroxy-5-methyl-4-isoxazolepropionic acid
AP: Anterior-posterior
BG: Basal ganglia
CA1: Cornu ammonis
CRF: Continuous reinforcement
DA: Dopamine
DAQ: Data-acquisition
DIO: Double-floxed inverse orientation
DLC: DeepLabCut
DLS: Dorsolateral striatum
DMS: Dorsomedial striatum
DV: Dorso-ventral
EYFP: Enhanced yellow fluorescent protein
Flp: Flipase
Fps: Frames per second
FR: Fixed-ratio
GABA: γ-Aminobutyric acid
GPe: External Globus pallidus
GPi: Internal Globus pallidus
IEG: Immediate-early gene
IP: Intraperitoneal
IR: Infrared
IT: Intratelencephalical
LP: Lever press
LTP: Long-term potentiation
MgT: Magazine training
ML: Medio-lateral
MOp: Primary motor cortex
MOs: Secondary motor cortex
MSN: Medium spiny neuron
NA: Numerical aperture
NMDA: N-methyl-D-aspartate receptor
PIR: Piriform cortex
PSD: Post-synaptic density
PT: Pyramidal-tract
SEM: Standard error of the mean
SNc: Substantia nigra pars compacta
SNr: Substantia nigra pars reticulata
SSpll: Primary somatosensory cortex lower limb region
SSpul: Primary somatosensory cortex upper limb region
STD Standard deviation
STN: Sub thalamic nucleus

1. Introduction

1.1. Preamble - Studying motor skill learning at the level of the striatal synapse

Whether tying our shoelaces or scoring a basket on a basketball game, we rely on our brain's ability to learn and reliably generate stereotyped task-specific motor outputs. These processes depend on the interplay between cortical and subcortical brain areas. The striatum is the largest input of the basal ganglia, a site where glutamatergic inputs from cortex and thalamus converge with dense innervation from midbrain dopaminergic neurons[1]. These inputs provide information about current goals, context, alternative actions, and related costs. Previous work suggests that the dorsomedial striatum plays an important role in the early phases of skill acquisition, whereas the dorsolateral striatum is more involved once the skill has been established and the action program becomes more automated[2].

Accumulating evidence has shown that synapses are structurally plastic, and their connectivity is remodeled throughout an organism lifetime to achieve optimal outcomes[3]. However, the contributions of striatal neurons to learning and action selection are still mostly interpreted within the framework of functional plasticity, i.e., in the changes of synaptic currents within a population of synaptic connections. The lack of spatial resolution of classical electrophysiological functional studies hamper synaptic plasticity studies at the single synapse level. Thus, it remains poorly understood how and when new synaptic connections are formed within the striatum, and what is their role in procedural learning and memory. Dissecting the changes in the number, size and spatial pattern of dendritic spines, the post-synaptic sites of synapses, will allow for a better understanding of how striatal input computation is modified to establish long lasting motor skills.

1.2. Neuronal circuits for movement

In our daily life we encounter many stimuli to which we need to react and act upon. Importantly, we must be able to select and learn new actions upon exposure to new contexts, situations or needs. This fundamental, but intricate process, relies on motor centers in the brainstem and spinal cord, which are in turn commanded by supraspinal areas, including the cortex, basal ganglia, and hindbrain (**Fig. 1**).

Precise timings and patterns of locomotion occur in the executive circuits, i.e., circuits able to elicit body movements, located in the spinal cord. Despite not being sufficient to generate sustained movement, these are highly complex circuits that form distinct and spatially separate modules for different muscles[4]. The brainstem is the posterior part of the brain and represents the major source of synaptic contact with spinal circuits, representing an interface between upper motor centers and the spinal cord. Lesion studies have highlighted the role of the brainstem in controlling movement[5]. Importantly, the brainstem has distributed neuronal populations that are important for the regulation of diverse motor behaviors[6]. These populations harbor neurons with different functions that are spatially intermingled but connected to precise circuitry for each behavior role. Together with spinal circuits, these coordinate the generation of naturalistic behaviors, as well as more refined movements such as skilled forelimb behaviours[6].

Still, brainstem and spinal circuits need input from brain areas to evaluate when and how these behaviors should be performed. Central to these processes are the basal ganglia, an interconnected group of nuclei responsible for integrating information from different inputs about internal state, context, and motor plans. Basal ganglia receive excitatory inputs from the cortex and the thalamus, as well as dopaminergic modulation from the midbrain; the output of these areas can modulate brainstem circuits[7]. Combined with the cortex, hypothalamus and superior colliculus, these regions determine when and which commands are active, as well as their vigor. The cerebellum, part of the hindbrain, is a brainstem-associated structure which is responsible for predicting sensory consequences of movement, allowing for its adjustment[8]. As for the cortex, early lesion studies demonstrated that it was not necessary for performing a variety of different motor outputs[9], indicating that subcortical regions should play dominant roles in motor control. Interestingly, cortical neurons are the only class of supraspinal neurons that directly with most other structures, including the basal ganglia, brainstem, and spinal cord. For these reasons, some authors argues that it works as a broadcasting mechanism, that distributes context-dependent and cognitive information through direct projections both to supraspinal and spinal circuits[10].

Figure 1 – Circuits for body movements. Integration of multiple regions from the central nervous system is needed to achieve a variety of different body movements. Adapted from Arber & Costa 2018[10].

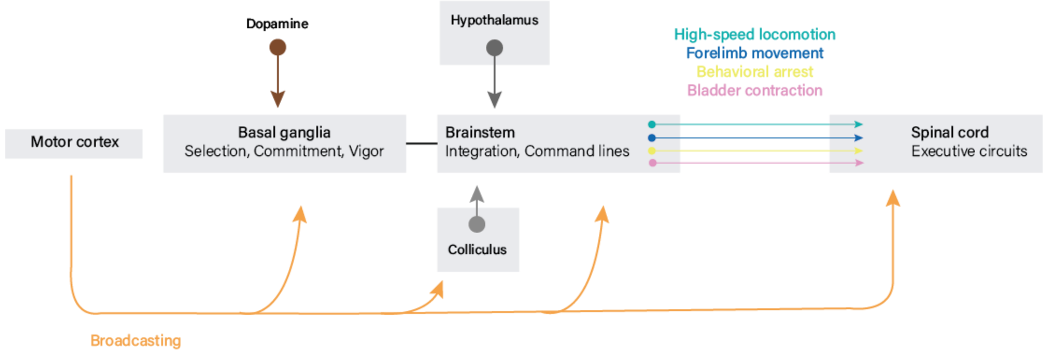

Despite detailed studies on anatomy and function of all these regions, it is still unclear how different regions and its neuronal subpopulations interact and integrate information to reliably produce simple movements, as well as stereotyped, long-lasting motor skills.

1.3. Basal ganglia – anatomy and role in movement

The first description of the basal ganglia is attributed to David Ferrier in his comprehensive 1876 work entitled *The Functions of the Brain*[11]. The epithet ‘basal’ reflected the location of the nuclei at the basis of the forebrain, while ‘ganglia’ referred to the observed large neuronal clusters. In modern literature, neuronal clusters in the central nervous system are commonly referred to as ‘nuclei’, whereas the term ‘ganglia’ is used mostly in the peripheral nervous system[11]. The term ‘basal ganglia’ is still the most commonly used denomination for these brain structures. Santiago Ramon y Cajal published his work on the histology of the nervous system in 1910[11], which included important descriptions of the classification of different cell types within the basal ganglia. However, no staining method at the time allowed tracing of axons over long distances, precluding a full understanding of connections within the different nuclei, which remained mostly unknown until the end of the 20th century[12].

The basal ganglia as we know them today are a group of interconnected subcortical nuclei that play a crucial role in movement control, as highlighted by the motor deficits that occur when these nuclei are pathologically affected, such as in Parkinson’s disease. Functions attributed to the basal ganglia include motor learning, habit formation, and action selection[7,13]. In higher vertebrates and rodents, the basal ganglia can be further subdivided into a dorsal and a ventral aspect. The dorsal aspect consists of four major nuclei: dorsal striatum, globus pallidus (GP), subthalamic nucleus (STN), and the substantia nigra (SN); these structures are involved in motor and associative functions. The ventral aspect of the basal ganglia consists of the nucleus accumbens (ventral striatum), ventral pallidum, and the medial parts of STN and SN, and is involved with limbic or emotional functions[14,15]. Some anatomical differences exist in the basal ganglia between rodents and higher vertebrates, including primates. In rodents, the striatum is a single nucleus often called the caudoputamen. In primates, the dorsal striatum is composed of the caudate nucleus, targeted by prefrontal cortical circuits (associative striatum), and putamen, which is targeted by motor and somatosensory inputs (sensorimotor striatum), and these regions are separated by the internal capsule[16]. Still, the internal capsule does not provide a precise division of functional zones, and some inputs from the prefrontal cortex also project to the putamen[1]. In rodents, there is no structural separation between inputs but there are still anatomical differences determined by the inputs - the dorsomedial striatum (DMS) receives mostly limbic and associative inputs, whereas the dorsolateral striatum (DLS) receives sensorimotor inputs (**Fig. 2.B**). For this reason, some authors consider the DMS homologous to the primate caudate, and the DLS to the putamen[17].

Most cortical areas provide inputs to the basal ganglia. In turn, inputs of the basal ganglia provide outputs to behavior effector systems, including thalamic nuclei that project to frontal cortical areas involved in planning and execution of movement, midbrain regions such as the superior colliculus which contributes to eye movement, the pedunculopontine nucleus which is involved in movement orientation, and hypothalamic circuits associated with autonomic functions[1]. It is important to mention that while basal ganglia connect the cerebral cortex with a wide range of effector systems, there are other parallel output systems of the cerebral cortex, such as direct corticospinal projections.

The canonical organization of the basal ganglia is described in **Fig. 2A**. The major input is provided by layer 5 (and occasionally layer 3 and 6) glutamatergic neurons from nearly all areas of the neocortex. The main input region of the basal ganglia is the striatum, and the principal targets of the cortical input are the medium-size spiny neurons (MSNs), which account for as much as 90% of all neurons in the striatum and use γ-aminobutyric acid (GABA) as a neurotransmitter. All corticostriatal neurons are glutamatergic neurons. Two main subtypes of corticostriatal neurons exist – the intratelencephalic (IT) and the pyramidal-tract (PT) neurons. The first provides axon collaterals that distribute only within the striatum and cerebral cortex and is mostly found in layer 5 and sometimes in layer 2/3 of the cortex. The latter gives rise to projections to the brainstem and spinal cord, as well as collaterals to the striatum, and is in deeper parts of layer 5 and occasionally on layer 6 of the cortex[1,18]. Additionally, while the striatum is a major target of PT neurons, it has been found that these neurons project to other basal ganglia components[19]. Inputs from different cortical areas vary - one work found that neurons in the secondary motor cortex layer 5 have high number of projections both to the ipsilateral (40% 'projection degree', i.e., the percentage of the area occupied by the projection signal relative to the total area) and contralateral (29% projection degree) striatum, in comparison to layer 5 neurons of the primary motor cortex (18% to the ipsilateral side vs 1% projection degree to the contralateral side)[20]. Additionally, there is differential projection of different cortical areas to striatal regions. The DMS receives input from associative cortices, such as the medial prefrontal, orbitofrontal, and anterior cingulate cortices, and thus is often referred to as the associative striatum. The DLS on the other hand, receives input from sensorimotor cortices, including primary motor cortex, and is referred to as the sensorimotor striatum (**Fig. 2B**). Along this medial to lateral gradient exists a topographical dopaminergic input from the SNc[21].

Corticostriatal afferents make synaptic contacts primarily with the head of MSNs dendritic spines (about 90% of all contacts), and less with dendritic shafts and somata[22]. In addition to cortical afferents, there are glutamatergic thalamic projections arising from the intralaminar nuclei, which also provide inputs to the striatum[23]. Midbrain dopamine axons tend to contact with the spines' neck, and one study found that only around ~60% of contacts were made with dendritic spines, 35% with the dendritic shafts and the remaining with the cell bodies[24].

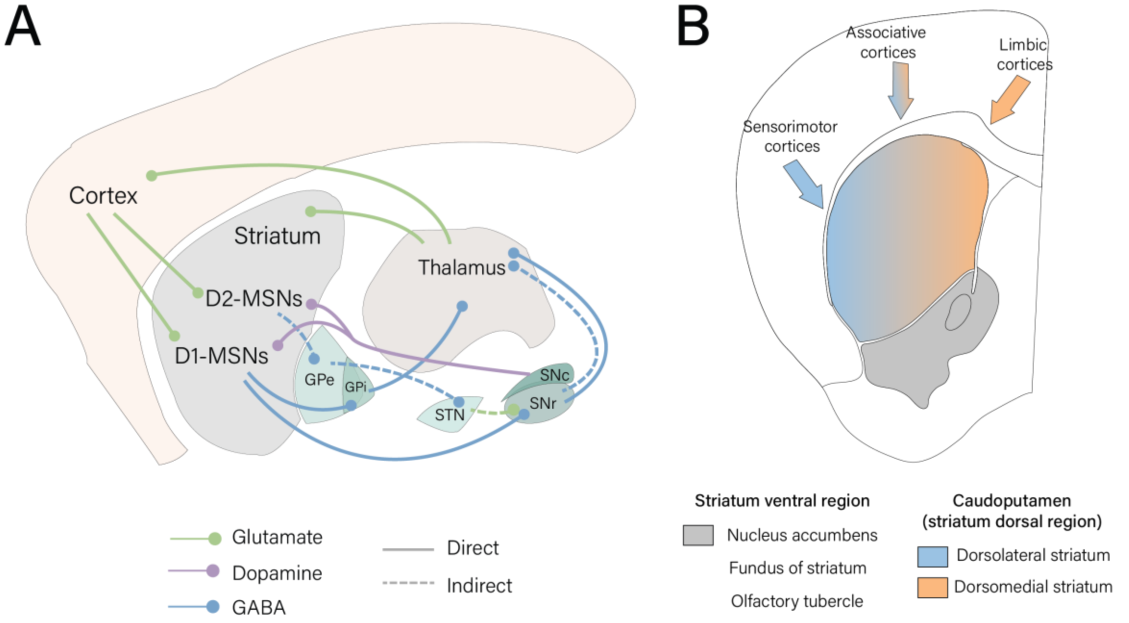

Figure 2 – Basal ganglia organization - major output pathways and striatum anatomy. (A) Scheme of sagittal view of the basal ganglia, composed of the striatum, external and internal globus pallidus (GPe, GPi), subthalamic nucleus (STN), and substantia nigra reticulata and pars compacta (SNr, SNc). Basal ganglia are strongly interconnected with the cortex and thalamus, forming functional loops with these regions. **(B)** Striatum anatomy and nomenclature. Coronal view of the striatum, with subdivision of dorsal and ventral regions. The dorsal region, also named caudoputamen, can be further divided in dorsolateral and dorsomedial striatum. **(B)** adapted from Perrin & Venance 2019[25]. *D1/D2-MSNs – D1- or D2- medium spiny neurons; GPe/GPi – external/internal globus pallidus; STN – subthalamic nucleus; SNc/SNr – substantia nigra pars compacta/ reticulata.*

Striatal MSNs neurons are divided in two types, characterized by their protein expression and projection outputs, which give rise to the two main components of the typical basal ganglia circuit – the 'direct' and 'indirect' pathways (**Fig. 2A** – straight lines are direct pathway, and dashed lines are indirect pathway). Direct pathway neurons provide collaterals to the globus pallidus internal segment (GPi) and SN, and only minor to the globus pallidus internal segment (GPe), thus contacting directly with the output nuclei[1]. The direct pathway is often referred to as the striatonigral pathway. Indirect pathway neurons only have collaterals to the GPe[1], and thus this pathway is frequently referred to as the striatopallidal pathway. Most of the indirect pathway neurons are also characterized by the expression of the neuropeptide enkephalin, the adenosine A2A receptor (encoded by the ADORA2A gene), and the D2-dopamine receptor. On the other hand, most of the direct pathway neurons contain the neuropeptides substance P and dynorphin, and the D1-dopamine receptor[26,27]. The distribution of different types of MSNs lacks distinct cytoarchitectural organization. Still, older studies have shown that, in rats, D1 receptor expression is slightly more prominent in ventrolateral and ventromedial striatum than in the DLS, whereas D2 receptor expression is more abundant in dorsolateral striatum[28,29].

In addition to MSNs, there are other striatal neurons, which are inhibitory interneurons of two main subtypes – the large aspiny neuron which uses acetylcholine as a neurotransmitter, or the medium-sized aspiny GABAergic interneuron. These cells are capable of integrating synaptic inputs over relatively large regions[30], do not project out of the striatum, and exert complex modulation of striatal synaptic transmission locally[1]. In addition, cortical neurons have been shown to interact with GABAergic and cholinergic interneurons to modulate MSN activity[31].

Self-paced movement is attributed to the tonic (sustained) activity of SNc dopaminergic neurons (DANs), while phasic changes in DAN activity are linked to reward prediction[7]. Recent studies have also shown transient DAN activity changes before and during self-paced movement initiation, relating with vigor of future movements and is encoded by neurons different to that encoding reward[32]. In the classical basal ganglia model, dopamine projections from the SNc will release dopamine at MSNs synapses, and have an opposite effect on the two MSNs types – when dopamine binds to D1 receptors, this leads to excitation of direct pathway neurons, whereas binding to D2 receptors will lead to inhibition of indirect pathway neurons[33]. Thus, activation of GABAergic inhibitory direct pathway neurons (as when dopamine from the SNc is bound) will inhibit neurons in the GPi and SNr, which tonically inhibit the thalamus. This will lead to disinhibition of the thalamus, which has excitatory glutamatergic projections to the cortex, leading to activation of cortical areas. On the other hand, activation of GABAergic inhibitory indirect pathway neurons (when dopamine is not bound), will lead to inhibition of the GPe, which has inhibitory projections to the STN. The STN will be disinhibited, which will disinhibit GPi and SNr projections to the thalamus, sustaining its tonic inhibition (**Fig. 2A**).

According to the classic model of the basal ganglia function, movement occurs during pauses in the tonic inhibitory activity of the basal ganglia output nuclei, which is generated by activity in the direct pathway[34]. However, while direct and indirect pathway where classically viewed as having opposing roles on action initiation and selection[35,36], recent work has demonstrated that activation of both pathways is concurrent, complementary and necessary for movement[37–39].

Selective optogenetic control of the direct and indirect pathway in vivo has shown that bilateral excitation of the indirect pathway in the DMS of healthy mice elicits a ‘parkinsonian’ state, characterized by instant freezing upon excitation, bradykinesia (slowness of movement), and decreased locomotor initiations[36]. On the other hand, stimulation of the direct pathway leads to reduced freezing and increased locomotion, and rescues motor deficits in dopamine-depleted mice[36]. The emerging idea is that both pathways are concurrently active to generate desired movement. In a lever-pressing operant task in mice, *in vivo* calcium imaging showed transient increases during the initiation of the session in both pathways in the dorsal striatum, as well as during the performance of different actions[37]. Both direct and indirect pathways were more active during ‘active’ states, than during ‘inactive’ states, and the strongest phasic increase occurred before the initiation of a set of actions or sequences[37]. In a lever pressing task, optogenetic inhibition of the direct pathway was shown to lead to a slowed/paused initiation and execution, while inhibition of the indirect pathway led to aborted initiation and execution[38].

Therefore, balance between the direct and indirect pathway is crucial. Hypokinetic disorders, such as Parkinson’s disease, are a consequence of overactivity of the indirect pathway, given that degeneration of SNc dopaminergic neurons will lead to disinhibition of D2-MSNs. Hyperkinetic diseases such as dystonia are produced by overactivity of direct pathway neurons[33].

1.4. Striatal function in motor and action learning

The striatum, the main input nucleus of the basal ganglia, has been implicated in a variety of different functions. In addition to the concurrent involvement of the direct and indirect pathway in movement[37,38], recent studies have implicated the striatum as having a variety of roles within motor and action learning (**Fig. 3**).

Figure 3 – Overview of the different roles of the striatum in motor and action learning. D1 and D2 refer to D1- and D2-MSNs, respectively, and their selective function within each role. References refer to selected

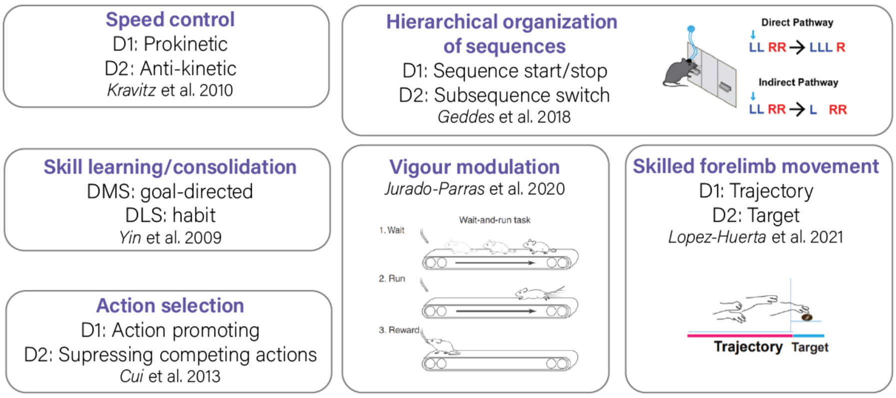

studies that support, through neuronal recordings and manipulation studies, the mentioned role. *DMS – dorsomedial striatum; DLS – dorsolateral striatum.*

An important component of behavior is its organization in sequences of actions, which requires precise timing and ordering of each movement. In one study, researchers trained mice on a lever press task and measured activity by electrophysiology in the dorsal striatum. This study found that MSNs show phasic increases in firing rate preceding the first and last presses of a sequence, and not so much in middle presses[40]. This was termed 'start/stop' activity, and was observed to increase consistently with sequence learning, and more prominently in the DLS than in the DMS. Disrupting N-Methyl-D-aspartate (NMDA) receptors in the striatum lead to a decrease in the percentage of neurons with start/stop activity as well as sequence learning[40]. This study demonstrates that MSNs are active at the beginning and end of particular action sequences and, importantly, that postsynaptic plasticity at MSNs is necessary for sequence learning. In fact, motor sequence learning is known to be disrupted in disorders affecting basal ganglia and striatal circuits[41].

A following study looked at the role of the direct and indirect pathway during learning of action sequences by performing optogenetic manipulations in the dorsal striatum. In the operant task, mice were trained to press the left and right levers in the specific spatiotemporal combination left-left-right-right (LLRR). At the behavioral level, this could be organized as a sequence of 4 elements, or as a hierarchical structure where left (L) or right (R) action elements are organized in two subsequences, which are then concatenated. Researchers observed that animals tended to learn the task in chunks of RR and LL, and mice with striatal knockout of NMDA receptors could not learn to chunk action elements into the correct subsequences. Activity recordings showed that D1-MSNs had sequence start/stop-related activity, while D2-MSNs were active during subsequence-switch. When D1-MSNs were optogenetically activated on the first L press, animals would perform an additional L press, forming a sequence of L-L-L-R. If D2-MSNs were activated instead, animals would perform one less L press, forming a sequence of 3 presses L- -R-R. These experiments showed that the striatal direct pathway seems to facilitate actions and control sequence start/stop, whereas the indirect pathway seems to inhibit actions and mediate subsequence switch[42].

The indirect pathway has been implicated in response flexibility in two recent studies from the Balleine lab. In one study, through genetic ablation in hybrid mice, they demonstrate that D2-MSN ablation has no effect on learning a regular lever press task, but affects extinction learning, given that recurrent responding persists[43]. The other work uses a two lever press task with rats, and shows that goal-directed learning is affected by chemogenetic inhibition of D2-MSNs in the DMS (and not D1-MSNs), given that animals were slower to learn to press the new lever associated with reward upon devaluation of the previously rewarded lever[44].

Procedural memories are long-term memories that store information on how to perform motor skills. Manipulations of the dorsal striatum have been shown to impair the execution of procedural memories and/or controlling movement kinematics but dissecting these two components is hard since procedural memories are expressed through movement. In a recent study where rats were lesioned in the dorsal striatum, the ability to remember a motor procedure was not affected[45]. Animals that learned a treadmill 'wait-and-run' routine were able to recover their performance and complete the task with similar proficiency a few sessions after lesion. In contrast to the transient deficits on procedural memory, running speed during the task decreased and remained low upon dorsal striatum lesioning. The magnitude of this decrease correlated with the size of the lesion, suggesting that the dorsal striatum is necessary for controlling movement speed or vigor. These animals were however capable of running at larger speeds when tested outside the task, highlighting that in-task deficits were due to a deficit in invigoration of the procedural memory during the task[45].

During motor skill learning, there is an initial phase of rapid improvement, followed by a phase of more gradual improvement as skills become automatized[46]. Using rotarod training in mice, it has been shown using *in vivo* striatal recordings that the DMS is particularly engaged early in training, while the DLS is mainly active at a later phase[2]. This was also observed at the level of synaptic strength, as long-term depression (LTD) saturation experiments, measuring how far synapses are form their lowest strength level, showed that corticostriatal synapses onto MSNs are more potentiated in the DMS of early-trained animals and in the DLS of late-trained animals. Training induced changes in the DLS specifically in D2-MSNs, and not in D1-MSNs. Interestingly, D1 receptor antagonists did not affected performance of the skill upon extensive training, whereas D2 blockade did. Overall, this work suggests that potentiation of excitatory transmission onto MSNs occurs in the DLS upon extended training preferentially in D2 receptor-expressing striatopallidal neurons[2].

Inputs to the dorsal striatum have been differentially implicated in the integration of task-relevant features. A study has investigated the activity of motor cortex projections (sensorimotor) to the DLS, and of medial prefrontal cortex (associative) projections to the DMS, in a rotarod task[47]. The authors found that associative projections were weakly engaged in naïve animals (first sessions), increased activity during training ('early trained' animals) and decreased it until the end of training ('late trained' animals). Sensorimotor projections showed high activity during first sessions (naïve and early trained animals) that then decreased until late training but at a slower pace then what was observed for associative projections. The authors observed that activity of DLS inputs correlated with rotarod velocity, and that disengagement (lower activity) of the DMS inputs were predictive of higher performance gains and maximum performance[47]. Interestingly, a different study found that after extensive training the DLS still revealed continuous representations of speed, position and time in rats trained in a treadmill task that had a spatiotemporal rule[48]. These representations were found to be weak in naïve rats and increased slowly with training. Inactivating the DLS in well-trained animals preserved the structure of the learned sequence but disrupted trial-by-trial variability[48]. These studies seem to suggest that DLS integrates task-relevant information to constrain the execution of learned motor skills.

Activity of the direct and indirect pathway has been shown to sustain different learning strategies. A study investigated the role of the two pathways in animals trained in a lever pressing task where self-stimulation was performed by optogenetics in either D1- or D2-MSNs[49]. In this task, two levers were available but only one led to optogenetic stimulation of the designated pathway in the DLS. Mice lever pressing for stimulation of D1-MSNs acquired lever pressing rapidly and pressed the active lever more often. Mice lever pressing for D2-MSN stimulation were slower in acquisition of lever pressing and pressed both lever presses almost equally, indicating that D2-MSN self-stimulation leads to generalization, consistent with the role of the DLS in habit learning[49]. Interestingly, a previous report showed that self-stimulation of D2-MSNs in the DMS leads to avoidance of actions[50], which could reflect a differential role of each MSN type in different striatal regions (i.e., DMS vs DLS). Another study using a lever pressing task, demonstrated that the acquisition of goal-directed behavior led to increased activity of D1-MSNs, but not D2-MSNs, in the DMS[51]. Moreover, D1-MSNs also displayed a higher α-amino-3-hydroxy-5-methyl-4-

isoxazolepropionic acid (AMPA)/NMDA ratio at goal-directed stages of training, suggesting that corticostriatal synapses onto D1-MSNs were potentiated[51].

MSNs have also been directly implicated in skilled forelimb movement. In a recent study, mice were trained in a single-pellet 'reach-to-grasp' task, and optogenetic manipulation of the ipsilateral and contralateral dorsal striatum to the trained paw was performed during training[52]. Inhibition of ipsilateral D1-MSNs, as well as excitation of contralateral D1-MSNs, were found to lead to increased trajectory errors. On the other hand, inhibition of D2-MSNs on both hemispheres led to higher success during task performance, whereas excitation led to increased target errors. *Ex vivo* electrophysiological experiments on striatal slices from trained mice showed increased inhibitory control of D1-MSNs over D2-MSNs ipsilaterally and of D2-MSNs to D1-MSNs contralaterally. These experiments demonstrate that both pathways differentially affect skilled movements, and that performance modifies striatal synaptic connectivity. The authors hypothesize that D1-MSNs are mainly involved in initiation of reach and control of its initial trajectory, whereas D2-MSNs are involved in accuracy of attaining the goal[52].

Two recent reports from the Ölveczky lab have investigated the role of the striatum and of its cortical and thalamic inputs in motor skill learning[53,54]. Researchers trained rats in a lever pressing task in which rats had to press a lever twice with a fixed inter-press interval. This generated a sequence of stereotyped movements, which included the two lever presses and other forelimb stereotypies. Lesions were performed, and the authors observed that both the projection from motor cortex to the DLS, as well as the DLS region itself, are necessary for animals to learn this two-step lever press task[53]. Activity of DLS, but not DMS, covers the whole motor sequence in a pressing task in a motor cortex-independent manner, given that lesions in the motor cortex did not affect movement encoding upon learning. Using a neural network to try to decode kinematics from DLS population activity, the authors found that forelimb vertical velocity could be well predicted from DLS activity[53]. Given the evidence and previous work from the laboratory that indicated that the motor cortex was necessary for the learning phase but not for performance of learned motor skills[55], the authors studied the contributions of the thalamus for this role. Indeed, silencing thalamostriatal synapses disrupts motor skill learning, and forelimb trajectories become identical to the ones performed by animals with a DLS lesion[54]. The authors suggest that upon learning, cortical projections are no longer necessary and the thalamostriatal circuitry is the one responsible for execution of learned motor skills[54].

All these hypothesized functions attributed to striatal neurons, highlight the possible existence of different neuronal ensembles responsible with different functions, even within the same pathway and/or functional domains. Recent molecular mapping studies have highlighted the neuronal diversity of striatal neurons, including the identification of a new subpopulation of striatonigral MSNs[56]. Future experiments of molecular functional mapping of different subpopulations within the striatum will help disentangle previously observed results and help define the role of different populations of striatal neurons in motor and action learning.

1.5. Immediate early gene expression in motor learning

Immediate early genes (IEGs) are genes that are activated rapidly and transiently in response to extracellular stimuli, without the need of new protein synthesis. IEGs were first characterized in non-neuronal cells through studies trying to identify genes that respond to growth factors and control the reentry of cells into the cell cycle[57]. The involvement of IEGs in non-dividing cells was first described in 1983 for *c-myc* in spleen cells[58], and in cells differentiated into neurons for *c-fos*[59]. Many IEGs encode DNA-binding proteins that function as transcription factors and mediate the expression of long-term responses by regulating the expression of late-response genes (LRG)[60].

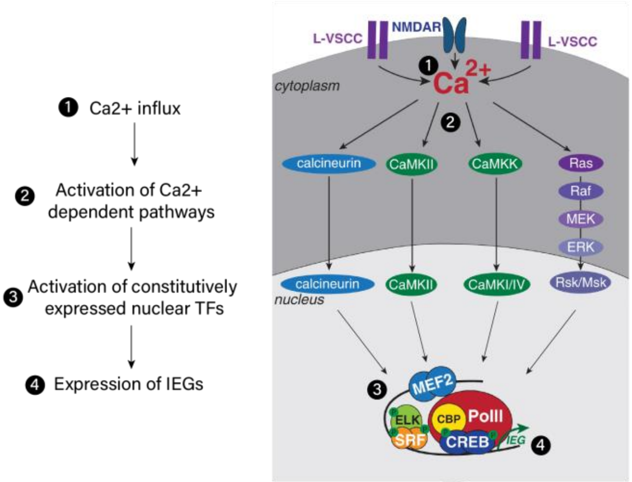

Figure 4 – Molecular mechanisms driving the expression of immediate early genes (IEGs). 1) Calcium (Ca^{2+}) influx will lead to the activation of different calcium-dependent pathways 2), which will activate pre-existing nuclear transcription factors 3). These will lead to immediate early gene expression 4), which function as transcription factors, modulating the expression of late response genes. Schematics adapted from Yap & Greenberg, 2018[60].

The mechanisms behind IEG expression are mostly neurotransmitter dependent, requiring an influx of extracellular Ca^{2+} [60]. Neurotransmitter released from the presynaptic terminal binds to its receptors on the postsynaptic neuron and triggers membrane depolarization, leading to an activation of Ca^{2+} channels. It has been shown that Ca^{2+} entry through L-type voltage-sensitive calcium channels (L-VSCCs) preferentially drives gene transcription, due to their location and intrinsic properties (**Figure 4** - 1)[61]. The resulting increase in intracellular Ca^{2+} stimulates a cascade of events, which the Ras - mitogen-activated protein kinases (MAPK) pathway, calcium/calmodulin-dependent protein kinases (CaMKII/ CaMKK), and calcineurin-dependent signaling (**Figure 4** - 2)[60]. In turn, these pathways lead to the activation of constitutively expressed TFs in the nucleus, including cyclic adenosine monophosphate (cAMP)-responsive element binding protein (CREB), serum response factor (SRF/ELK), and myocyte enhancer factor 2 (MEF2), through post-translational modifications (**Figure 4** – 3)[60]. These TFs will in turn trigger the transcription of activity-regulated genes such as IEGs (**Figure 4** - 4)[60]. Once in the nucleus, the IEGs Fos and Jun will form the the major heterodimer of the activating protein complex 1 (AP-1), also composed of other TFs of the highly redundant Fos (which includes *c-fos*) and Jun family[60]. Other IEG families exist, such as the *EGR*-family, which includes Zif-268 protein. The Fos family has been shown to differentially bind to DNA and lead to the expression of LRGs[62]. LRGs typically encode effector proteins that regulate cellular processes such as dendritic growth, spine maturation, synapse pruning and the excitatory/inhibitory balance[63]. Recent studies have shown that the AP-1 complex despite having a large repertoire of enhancer binding sites, shows cell type-specific binding[60].

In the late 1980s, multiple studies showed that c-Fos is rapidly induced in different brain nuclei after pharmacological convulsive stimulation and electrical stimulation[64,65]. Because of these findings, the field characterized and studied IEGs as a tool to visualize neuronal activity in the brain. Worley's group identified more than ten novel IEGs through identification of complementary DNA (cDNA), including activity-regulated cytoskeleton-associated protein (*ARC*)[66] and homer protein homolog 1 (*HOMER1a*)[67]. The resulting gene products of these genes are proteins that have been shown to function as negative regulators of AMPA receptor expression at synapses[60]. These differ from the gene products of the Fos and Jun families, which are TFs, and are considered 'effector proteins' given their direct involvement in synaptic functions[60]. The expression patterns are also different, given that TFs are found in the nucleus while Arc for instance, is enriched in neuronal dendrites. Multiple models of IEG knockout mice share similar behavioral and synaptic abnormalities[68,69], which highlights IEG functional relevance in long-term synaptic plasticity and memory processes.

IEGs have been used since as markers of recent activity and/or plasticity in a variety of different contexts, including stress and sensory stimulation paradigms, and behavioral training[70,71]. Different IEGs can have differential expression patterns within the same context. In one study, rats were subjected to spatial and non-spatial water mazes and protein levels of c-Fos, Zif-268 and Arc were found to be similar in the hippocampus, entorhinal and primary visual cortices upon training[72]. Though there seems to be differential expression of IEGs, one feature appears to be common: while initial exposure to novel stimuli leads to an increase in IEG expression, upon repeated exposure there is a decrease in IEG expressing cells. This seems to correlate with the consolidation of neuronal ensembles. For instance, one study found that rats exposed to repeated restraint stress across days show less *c-fos* mRNA than animals that were exposed to acute restraint stress, and upon 9 days of exposure no significant levels of *cfos* mRNA were found in repeatedly restrained rats[71].

Some studies have reported IEG expression in the context of motor learning, particularly in the cortex. In an early study, Fos expression was studied upon acrobatic training (obstacle task) in female rats[70]. Researchers found an increase in the number of Fos-positive cells in layer II/III of the primary motor cortex when compared to controls not trained in any task ('inactive') and controls that were forced to transverse a runway only ('motor' controls). The percentage of Fos-positive cells was higher in the first 3 days of training, and decreased rapidly until day 10, from which point onward it plateaud[70]. More recently, a study using *in vivo* two-photon microscopy showed that mice trained in a rotarod task have significantly more cells expressing Arc in the secondary motor cortex when compared with homecage controls, on the first day of training[73]. However, in subsequent days of training, the number of cells expressing Arc significantly decreases. Interestingly, mice consecutively trained in a rotarod and a wheel running task show distinct Arc-expressing neuronal ensembles, with partially overlapping neurons[73]. Lastly, researchers also found that initial high intensities of Arc-promoter activation predict that the same neuron will be Arc-positive upon further training in the rotarod task[73]. A study using a skilled reaching task in rats, found increased levels of Arc in the contralateral primary motor cortex to the trained limb[74]. Interestingly, this increase was not observed in other regions, including the striatum, rostral motor area, primary somatosensory cortex and cerebellum[74].

Striatal immediate early gene expression studies have mostly been performed in drug and pharmacological studies. In the 1990s, different groups worked on the effect of D1- and D2-agonists and antagonists in the striatum. In one study, rats treated with selective D1- or D2-agonists showed small increases in the expression of Fos-like antigens[75]. Simultaneous administration of the two agonists lead to robust expression of Fos-produced patches of intensely stained nuclei[75]. A different study examined the effect of the same agonists in the striatum of dopamine-depleted rats and found that injection of D1-agonist produced a dose-dependent increase in *c-fos* and *zif-268* mRNAs, as assessed by in situ hybridization[76]. The D2-agonist, on the other hand, led to decreased expression of *zif-268*. Similarly to the previous study, combined administration led to enhanced IEG expression[76].

A group of studies studying *c-fos* expression using *in situ* hybridization have shown that, in rats injected with cocaine (to achieve acute induction of *c-fos*), *c-fos* expression in the striatum is higher in rats trained in a running wheel than in rats placed in a locked wheel[77,78]. Interestingly, this expression is already visible after 1 day of training and is higher and more widespread at day 2 of training. The effect was higher in caudal sections, and maximal in the dorsal sensorimotor region of the striatum that receives inputs from the primary and secondary motor cortices, as well as the sensorimotor cortex, and was the weakest in striatal regions receiving input from the anterior cingulate cortex. Upon 8 days of training, researchers observed no significant difference between rats that were trained on the running wheel vs the ones placed on the locked wheel[77,78].

Two recent studies from the Balleine lab address plasticity markers' expression in the context of motor learning[43,44]. One study used immunodetection of phosphorylated histone H3 on serine 10 (P-H3), a ubiquitous transcriptional activation marker induced in MSNs in response to dopamine[43]. This phosphorylation has been shown to occur in the *c-fos*-associated nucleosomes[79]. They show that MSNs were transcriptionally active during learning of a lever pressing task, and that early trained mice have higher levels of expression in the DMS striatum, while late trained mice have higher levels of expression in the DLS[43]. The other study uses a lateralized lever press task with rats, and shows a modest contralateral increase in the expression of plasticity marker Zif268 in D1-MSNs, but not D2-MSNs (~5% increase in % of D1-MSNs co-localizing with the marker)[44].

Very few studies address immediate early gene expression at the whole-brain level, and to our knowledge, only one study performed this type of experiment in the context of motor learning[80]. In her dissertation, M. Mathis describes that mice trained in a head-fixed forelimb reaching task have a higher expression of c-Fos in multiple brain regions, when compared with mice placed inside the box but that did not perform the task[80]. These regions include the rostral primary and secondary motor cortex, forelimb somatosensory cortex, dorsolateral striatum, and gustatory areas. However, it was not reported whether these changes are contralateral to the trained paw[80].

Thus, immediate early gene expression and characterization upon motor learning remains a highly unexplored area. Characterization at different time points of learning, as well as *in vivo* studies for different IEGs (including continuous imaging across training and neuron tagging and reactivation experiments) are crucial to expand our knowledge of how neuronal ensembles are activated and consolidated to establish long-lasting motor skills.

1.6. Motor learning and dendritic spine plasticity

Dendritic spines are small protrusions that arise from dendrites of many neurons. These small dendritic appendages are composed of a spine head, which typically accommodates an excitatory synapse, and a spine neck that connects to the dendritic shaft (**Fig. 5.A**). Ramón y Cajal was the first to acknowledge dendritic spines and proposed that these structures serve to connect axons with dendrites, increasing the amount of dendritic membrane available for synaptic contacts when compared to direct connections of presynaptic terminals on dendritic shafts[81]. Indeed, most excitatory contacts terminate on spines rather than on dendritic shafts, as is the case of glutamatergic cortical inputs to the striatum, as mentioned on **Section 1.3**, and practically all spines have an excitatory synapse on their head[82]. Dendritic spine plasticity, or structural plasticity, is defined as the short- and/or long-term dynamic changes in spine morphology and density led by persistent neuronal activity. In a simplistic view, while functional synaptic plasticity properties refer to changes in synaptic strength of existing connections, structural plasticity entails changes in the number and morphology of synaptic connections[83].

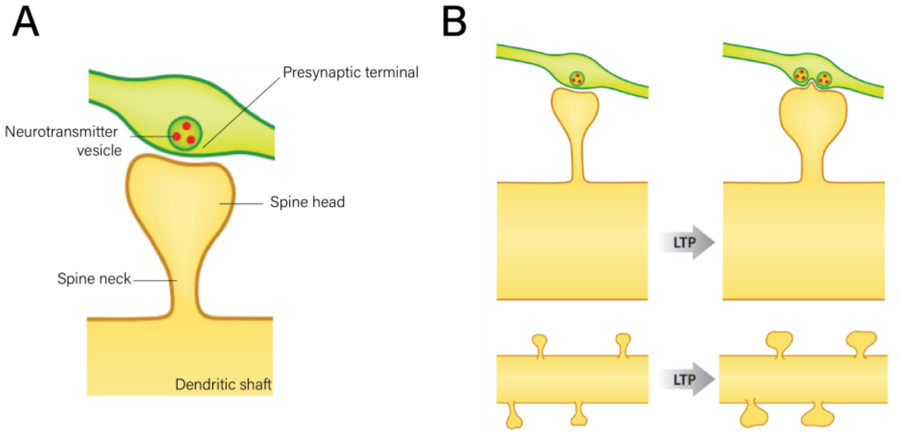

Figure 5 – Dendritic spine nomenclature and plasticity. (A) Schematic diagram of a dendritic spine with basic nomenclature. **(B)** Changes in spine morphologies during synaptic plasticity – the spine head and neck suffer morphological alterations with long term potentiation (LTP) mechanisms. Adapted from Yuste 2013[84].

Glutamatergic synapses mediate most of all excitatory neurotransmission in mammals. Glutamate is released from presynaptic terminals and activates AMPA and NMDA receptors at the spine head surface[82]. Receptors are concentrated close to the presynaptic element, a zone that forms the post-synaptic density (PSD), a membrane-associated 'mega-organelle' that contains a high concentration of glutamate receptors[85]. While only AMPA receptors that lack the GluR2 are permeable to Ca^{2+}, permeability to Ca^{2+} is a feature of NMDA receptors[86]. In addition to glutamate, NMDA receptors require membrane depolarization to open with high probability because of voltage-dependent Mg^{2+} block[86]. With synaptic activity, AMPA receptor-mediated depolarization of the postsynaptic membrane facilitates activation of NMDA receptors by removing the Mg^{2+} block that usually prevents NMDA receptor currents at resting membrane potentials[87]. This activates calcium-dependent signaling pathways that modulate AMPA receptor insertion at the surface of the post-synaptic compartment[86]. Increasing AMPA receptor levels at the postsynaptic membrane leads to changes in synaptic strength, which can lead to long-term potentiation (LTP) of synapses[86,88], a process which is widely considered to be a substrate of learning and memory. NMDA receptors are thus usually assigned a regulatory role, whereas AMPA receptors have an effector function, and a high AMPA/NMDA ratio is associated with increased plasticity[86].

Theories about the special role of spines have been centered on potential functions of spines in enhancement of structural connectivity or biochemical compartmentalization, particularly Ca^{2+} compartmentalization. Local calcium influx upon neuronal depolarization is aided by the diffusional barrier of the spine neck, generating isolated Ca^{2+} accumulations[81]. The other hypothesized function is that spines are electrical compartments, enabling inputs to generate and experience different membrane potential dynamics due to their special morphology. While input-specific biochemical isolation has been shown to occur without spines[89], spines can sustain membrane potential that differs to that of the dendrite[84].

Spines display a large diversity of morphologies, and many researchers have tried to classify spines according to their morphological features. Others suggest that spine diversity rather forms a continuum without clear distinction of different types of spines[90]. The most accepted classification of spines proposes three spine types: thin (thin long neck with a small head), mushroom (large head), stubby (no neck)[81,91]. In addition, thin long protrusions with no clear head are considered filopodia, and these are mostly found during development. The majority of spines have single heads, but a small proportion of spines are branched, having two spine heads[81]. Spine morphology and geometry is thought to correlate with function. For instance, one work using two-photon glutamate uncaging has shown that hippocampal cornu ammonis (CA1) neurons have AMPA-type receptors more abundantly in mushroom spines, considered to be mature spines, in contrast with thin spines or filopodia[92].

Experimental evidence shows that long-term synaptic plasticity mechanisms are associated with morphological changes in spines. For instance, long term potentiation (LTP) leads to increases in spine head size and to spine neck dynamic changes[93] (**Fig. 5.B**). One study has found that upon minimal extracellular stimulation, spine neck length correlates inversely with synaptic efficacy, as measured by the excitatory postsynaptic potentials generated by individual spines[94]. Further, spine necks have been shown to isolate inputs electrically, and lead to higher potentials upon spine glutamate uncaging in the soma of spines composed of smaller necks[95]. On the other hand, spine head volume has been shown to be well correlated with PSD area[90]. Upon two-photon glutamate uncaging, enlargement of spine heads upon was observed to colocalize with potentiation of AMPA-mediated currents[96].

Historically, many researchers studied spine plasticity in fixed tissue using light microscopy, by impregnating neurons with Golgi-Cox stain[81]. Recent common techniques include DiOlistics, microinjections of fluorescent dies (such as lucifer yellow), and viral approaches (as in neuronal tracing). Each technique has its advantages, but Golgi-cox staining is less used nowadays given that it is difficult to use in conjunction with other labeling methods[97]. As for DiOlistics, a ballistic delivery of the lipophilic carbocyanine dyes - the most widely used, DiO and Dil[98]- is advantageous given that different lipophilic dyes with different spectra can be mixed[97]. However, it may leak out of membranes upon tissue permeabilization, when immunostaining is needed for co-labeling with other proteins[99]. With the development of transgenic mice and new viral approaches to achieve specific labelling of neuronal populations, as well as high-resolution fluorescence microscopy, viral approaches have become increasingly popular in anatomical studies. The latter can be advantageous, given that i) high signal specificity can be achieved when using viral approaches that make use of gene targeting systems, ii) other immunostaining techniques can be performed in parallel, and iii) it's compatible with tissue clearing, which allows imaging at the full depth of thicker tissue samples. Currently, high-resolution confocal microscopy in fixed tissue and two-photon microscopy in the living brain are considered state-of-the-art in structural plasticity studies, and detailed protocol guides that provide step-by-step guidance have been described[100].

Structural plasticity has been shown to occur upon exposure to a variety of stimuli. An *in vivo* study has shown that there is increased spine density of somatosensory cortical neurons in mice that were born in environmentally-enriched cages, in comparison to single housed mice in standard cages[101]. Other studies in fixed slices have also demonstrated increased spinogenesis in environmentally-enriched animals, including in striatal MSNs[102]. Drugs of abuse, such as cocaine and amphetamine, have also been shown to lead to increases in MSN spine density in the nucleus accumbens and pyramidal cells of the prefrontal cortex[103]. Alcohol has been shown to lead to increases in mushroom-shaped spines in D1-MSNs, but not D2-MSNs, in the DMS and induce long-lasting increases in AMPA receptors[104]. On the other hand, a study using methamphetamine found that drug consumption led to an increase in mushroom and thin spines in the DLS, but a decrease in mushroom spines in the DMS (without distinguishing between MSNs types)[105]. Importantly, spine plasticity has been shown to occur in several synaptic and behavioral plasticity paradigms, leading to the hypothesis that they may form a structural basis for long-term memory. A lot of these works have studied CA1 neurons spine plasticity in memory-based paradigms, a structure well-known to be involved in memory processes[106,107].

In vivo imaging studies have highlighted that there is dendritic spine turnover and clustering processes, which influence learning and memory. A recent study has shown that, during performance of contextual or spatial learning, in the retrosplenial cortex (involved in these types of learning), spine turnover before learning predicted future learning and memory performance, as well as localization and rates of spine clustering[108]. Using a transgenic mouse with a mutation that leads to increases in spine turnover (C-C chemokine receptor type 5 null heterozygous mice), researchers found that both performance and spine clustering were enhanced. The authors hypothesize that spine dynamics follow a 'hotspot' model, where spine turnover is a driver for clustering of spines[108].

Two *in vivo* studies have highlighted the role of structural plasticity in motor skill acquisition in the primary motor cortex[3,109]. Remarkably, in one study mice were trained in an accelerated rotarod and spine dynamics were followed over weeks upon training. Researchers found that training leads to increased spine formation (~5% of total spines) in both young and adult mice, when compared to non-trained animals[3]. Only a small fraction of these newly formed spines (0.04% of total spines) persists two weeks upon end of training, but they are stably maintained later in life. Interestingly, resuming motor training after a 3-month interval in training leads to spine formation only on a new training regime. The authors propose a mechanism where there is lifelong maintenance of a small subset spines induced by novel experience that provide a structural basis for lifelong memory storage[3]. In the other study, researchers developed a genetic tool able to label newly formed and recently potentiated spines and specifically induce their shrinkage *in vivo*. Using this tool, the authors found that specific shrinkage of spines formed or potentiated during rotarod training leads to decreases in task performance, and that re-training on the rotarod induces re-potentiation of those same spines[109].

To our knowledge, only two studies have addressed MSN dendritic spine plasticity upon action selection in fixed slices. These reports used lateralized T[110] and plus[111] maze paradigms to investigate learning-related MSN dendritic changes. Even though animals in these tasks need to perform an action (walking to a location), neither can be considered a motor task given that no specific skill is developed. Rather, these tasks are cognitive-based navigation tasks that probe the animal's ability to memorize the location of a reward. The plus maze study found significant dendritic spine changes during a goal-directed phase of training, showing an increase in dendritic spine density in the DLS, but not DMS, and particularly in mushroom spines[111]. In this study, researchers also compared the differences in spine density in Zif-268 positive vs negative neurons, and in contralateral vs ipsilateral hemisphere to the location of the reward, i.e., the turning side, and found a similar increase in mushroom spines in all conditions. The other study, using a plus maze, also compared spine density in the contralateral vs ipsilateral hemisphere to the turning side, as well as in DMS vs DLS, and found no significant effect of training on spine number in any of these regions[110]. Neither of these studies distinguished between D1- and D2-MSNs. While these results are apparently contradictory, they may reflect methodological differences, such as the assessment of primary[110] versus higher order dendrites[111].

Overall, while several studies suggest a fundamental role of structural plasticity in learning and memory in several regions of the brain, few studies document dendritic spines changes in the striatum upon learning paradigms. Additionally, no studies have yet addressed spine plasticity upon motor learning tasks. Thus, while multiple studies demonstrate the role of the dorsal striatum in different aspects of motor skill learning (see **Section 1.4**), it remains unknown whether motor skill learning affects structural plasticity in MSNs. This hinders a full understanding of striatal and MSN function, and how plasticity is achieved in this region to establish long-lasting motor skills.

2. Objectives

Recent evidence highlights the important role of structural plasticity, i.e., changes in the number, size and/or spatial pattern of dendritic spines, in learning processes. The striatum is known to be a key player in skill learning and consolidation, however not much is known about how its neurons compute input information at the level of the synapse to establish skills.

This work is part of a larger project aimed to unravel the role of striatal medium spiny neuron (MSN) dendritic spine plasticity in motor learning. In this dissertation, we aimed to investigate changes in a marker of activity upon motor learning, and establish the tools and techniques needed to study dendritic spine plasticity in fixed brain slices.

For that purpose, the specific objectives of this study were:

1. Establish a lateralized lever pressing task to study motor learning in mice and analyze performance and movement kinematics throughout training.

2. Establish a candidate immediate early gene as a marker of neuronal activity and characterize the pattern of active cells in motor-related brain regions upon motor learning.

3. Optimize a viral sparse labelling technique to allow visualization of the whole dendritic arbor of single MSNs and design a dendritic spine analysis pipeline, using high-resolution confocal microscopy, deconvolution and 3D reconstruction and analysis.

3. Methodology

Acknowledgments

I would like to acknowledge Doctor Daniela Pereira, for providing the expertise on the sparse labelling technique previously developed by her, performing all the stereotaxic surgeries as well as for conducting the behavior experiments alongside me. I would like to thank Doctor Marcelo Mendonça for his help, and expertise throughout the behavioral experiments, for providing the behavioral setup and a significant part of the custom scripts both for the behavioral software setup and general performance analysis. I would like to thank Doctor Luke Hammond for early access to the pipeline used for cell detection and atlas mapping (*BrainJ*).

3.1. Animals

All procedures, as well as housing and breeding, were performed at Champalimaud Center for the Unknown (Lisbon, Portugal). The institution's vivarium is licensed for animal experimentation by the Portuguese Directorate-General for Animal Welfare (DGAV – Direção Geral de Alimentação e Veterinária) and complies with European guidelines (Directive 2010/63/UE of September 22, 2010), National laws (Decree law 113/2013 of August 7, 2013), and Federation of European Laboratory Animal Science Associations (FELASA) recommendations. All experiments were conducted in accordance with protocols approved by DGAV, the Rodent facility of the Champalimaud Center for the Unknown, and the Ethical Committee at NOVA Medical School (Lisbon, Portugal).

Mice (Mus musculus) of the inbred strain C57BL/6 were housed at 19°-22°C with 30-70% relative humidity in a light cycle of 12h light/12h dark, with ad libitum access to food (except when submitted to food deprivation) and water and changed into new cages every other week. Mice were housed at 2 to 4 animals per cage and experiments/procedures were performed on the light cycle.

Experiments were conducted in A2A-Cre (B6.FVB(Cg)-Tg(Adora2a-cre)KG139Gsat/Mmucd), D1-Cre (EY217 line: Tg(Drd1a-Cre)EY217Gsat/Mmucd) and wild-type

mice. The transgenic animals were originally obtained from The Jackson Laboratory and were backcrossed to C57BJ/6J background for at least 6 generations. Additional information regarding mice strains can be found on **Annex I**.

3.2. Striatum viral injections by stereotaxic surgery

Stereotaxic brain surgeries were performed in D1-Cre and A2A-Cre mice (expressing Cre recombinase specifically in D1-MSNs and D2-MSNs, respectively) to deliver adeno-associated viruses (AAVs) at target brain regions. All surgeries were performed under anesthesia (5% isoflurane by inhalation for induction followed by 1-2.5% isoflurane with 1.5-2% oxygen during surgery). Mice were placed on a stereotaxic apparatus (David Kopf Instruments, #962LS) equipped with a thermostatically controlled heating pad (World Precision Instruments, #ATC1000) kept at 37˚C, and their eyes were covered with an eye gel (Visidic gel) to prevent drying. The head was shaved and cleaned with 70% ethanol and iodine. The skull was exposed with an incision through the midline, allowing Bregma and Lambda identification, reference points used for stereotaxic surgeries. Bregma is the point in which the sagittal and coronal sutures of the skull converge, while Lambda is the point of convergence between the sagittal and lamboid suture. After alignment of the head, holes were drilled in the skull (Henry Schein, tungsten drills #1/4) in the desired locations, according to anterior-posterior (AP), mediolateral (ML) and dorsoventral (DV) coordinates estimated from the Paxinos Mouse Brain Atlas[112].

To achieve sparse specific labelling of D1- and D2-MSNs with enhanced yellow fluorescent protein (EYFP), a previously tested mix of adeno-associated viruses was injected in the striatum of D1-Cre and A2A-Cre mice. This viral suspension is a mixture of AAV1-Ef1a-DIO-Flpo-WRPE (AAV-DIO-Flp) and pAAV8-hSyn-Con/Fon-EYFP (AAV-Con/Fon-EYFP; **Table 1**).

Table 1 – List of AAV's used in this study.

Full name	Short name	Reference	Vendor & Reference number	Protein encoded	Dependencies	Original titer vg/ml
AAV1-Ef1a-DIO-Flpo-WRPE	DIO-Flp	Zingg et al, 2017[113]	Duke University Viral Vector Core #193	Flipase	Cre recombinase	$8x10^{12}$
pAAV8-hSyn-Con/Fon-EYFP	Con/Fon-EYFP	Fenno et al, 2014[114]	Addgene 55650-AAV8	EYFP	Cre recombinase Flipase	$2.4x10^{13}$

Abbreviations: *vg/mL – viral genomes per milliliter; Flp – flipase; AAV – adeno-associated virus.*

A detailed explanation of the molecular events leading to EYFP expression can be found on **Box 1**. An appropriate dilution of AAV-DIO-Flp ensures that only a few neurons will express both Flipase (Flp) and Cre, and therefore, EYFP. On the other hand, AAV-Con/Fon-EYFP is used undiluted to yield high EYFP expression in the Flp and Cre-positive cells (**Box 1**)[114].

Box 1 | Sparse labelling approach

A population of Cre expressing neurons needs to be transfected with both DIO-Flp and Con/ Fon-EYFP viral constructs for the expression of EYFP to occur, as a result of consecutive recombination events. This will lead to the expression of the fluorophore in a small fraction of neurons, resulting in a sparsely labelled population.

In the DIO-Flp construct, Flp is encoded in an inverted, inactive orientation, and flanked by double-floxed inversed orientation (DIO) loxP sites, comprised of inverted terminal repeats. These loxP sites are recognized by the Cre recombinase, resulting in an inversion of the DNA region in between (when lox sites are in opposite orientation), followed by a second event of excision (when lox sites are in the same direction), leading to the correct orientation of the construct. Inversion occurs via either loxP or lox2272, followed by the excision of the other two lox sites (here shown in one possible combination).

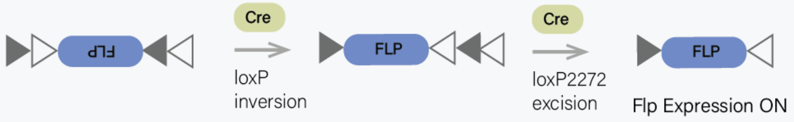

In the Con/Fon-EYFP construct, EYFP is encoded in a bipartite and inversed manner, and flanked by both loxP and FRT sites. Neurons now expressing Flp and Cre, if transfected with this construct, will undergo four recombination events in a similar manner. In this construct, Cre-dependent directional control of the exon coding the N-terminal region of EYFP and Flp-dependent directional control of both C- and N-terminal regions of EYFP are necessary for all exons of the construct to be in the sense direction. Each inversion event can occur in either Cre/Flp recognition sites, followed by the excision of two lox sites (here shown in one possible combination).

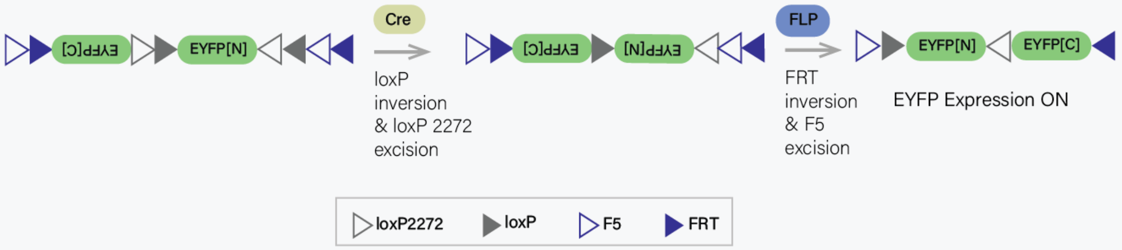

Different formulations of the AAV mix as well as different injection coordinates were tested for troubleshooting the ideal MSN labelling density (**Table 2** and **Fig. 6**). The mix was prepared every surgery day in a cell culture hood, by adding 0.75µL of the diluted AAV-DIO-Flp virus (20% v/v; the different dilutions are described above) to 3µL of the Con/Fon-EYFP virus (80% v/v), for a total volume of 3.75µL. In two of the subject groups, two different mixes were prepared, with different AAV-DIO-Flp virus dilutions, and 2 animals were injected with each dilution.

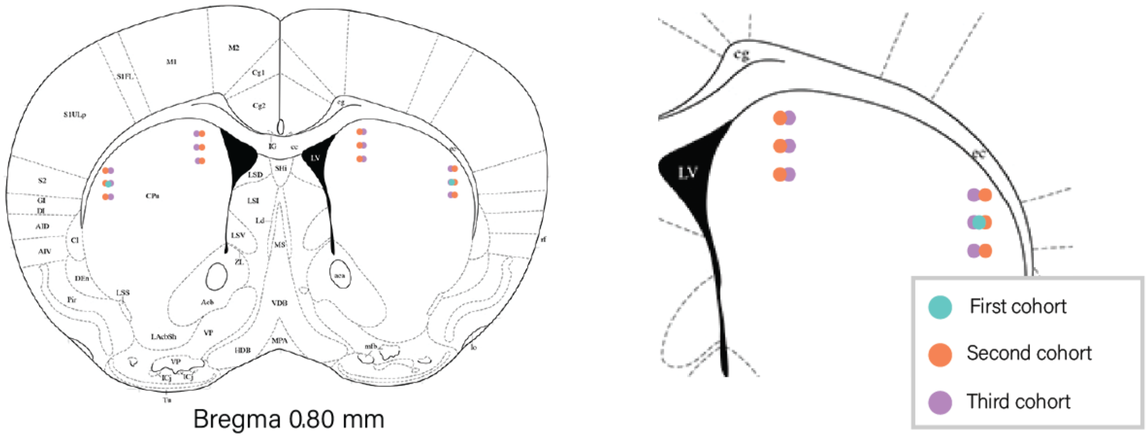

Figure 6 - Scheme of the approximate injection sites of the first (blue), second (orange) and third (purple) cohorts of animals. Reference image from Paxinos brain atlas[112].

Table 2 – List of the viral injections performed for each subject group. In the first group, 1:400 dilution of the AAV-DIO-Flp component was performed and there was only 1 injection per hemisphere. In the following 2 groups, two different dilutions of the AAV-DIO-FLP component were tested (2 animals/ dilution) and 2 injections per hemisphere, divided by 3 DV locations were performed, to target the DMS and DLS and achieve a better spread of the virus. Coordinates were estimated from the Paxinos Mouse Brain Atlas[112].

Group	Subjects	Age (weeks)	AAV-DIO-Flp dilution	Coordinates (mm)			Injections/ hemisphere	Volume injected/ position
				AP (+)	ML (+/-)	DV (-)		
1	2 ♀, 2 ♂ D1-Cre	8-11	1:400	0.8	2.35	-2.0	1 at 1 DV location	100 nl
2	4 ♂ D1-Cre	5-7	1:400 and 1:800 (2 mice/ dilution)	0.8	DMS		2 injections, each divided by 3 DV locations	75 nl
					1.2	2.0, 1.7, 1.5		
				0.8	DLS			
					2.4	2.2, 2.0, 1.75		
3	4 ♂ A2A-Cre	9	1:1000 and 1:2000 (2 mice/ dilution)	0.8	DMS			
					1.25	2.0, 1.7, 1.5		
				0.8	DLS			
					2.35	2.2, 2.0, 1.75		

Abbreviations: *AP- anterior-posterior, ML - mediolateral, DV- dorsoventral.*

The mix was injected at each site, at 4.6 nl/pulse (total volume either 75 or 100µL, as described in **Table 2**), using a glass micropipette attached to a nanojet II auto-nanoliter injector (Drummond Scientific). To minimize backflow of the AAV mix, the pipette was kept in place for 2 minutes after the last pulse between DV positions (when injections at multiple DV locations were performed for the same ML location) and for 5 minutes after the last pulse of the most superficial DV position, and only then slowly withdrawn. For all cohorts, AP and ML coordinates are relative to Bregma, while DV coordinates are relative to the brain surface at the given ML location.

Following all injections, the scalp was closed with Vetbond tissue adhesive (3M) and the analgesic carprofen mouse mix was administered subcutaneously, at 5 mg/kg body weight, prior to recovery from anesthesia. After surgeries, animals were closely monitored, kept in a cage with heating until they regained conscience and checked for recovery before being returned to their home cages. Animals were subjected to further experiments only after an adequate time for surgery recovery and viral expression, i.e., 3 to 4 weeks post-injection.

3.3. Apomorphine experiments

The D1-Cre mice subjected to AAV injection surgeries (group 1 and 2; **Table 2**) were further treated with either an apomorphine intraperitoneal injection (IP) at 10mg/kg or injected with a corresponding volume of control saline/vehicle solution (4 mice/condition), 2h before being sacrificed with a sodium pentobarbital lethal injection (see **Section 3.5**). The timepoint for lethal injection was determined according to previous literature[115,116]. Brain slices from these animals were used for optimization of the sparse labelling technique (**Figs. 27-29**) and for troubleshooting the immediate early gene staining (**Figs. 18-20**).

For the experiments depicted in **Section 4.2.**, 6 wild-type mice of 8 to 9 weeks of age were handled and habituated to IP injections for 10 consecutive days, corresponding to the lateralized task duration (see **Section 3.4.2.**). During this time, mice were subjected to a daily IP saline injection, as their task trained counterparts (to minimize the confounding effect of the terminal pentobarbital injection). At the seventh day of habituation, each mouse started receiving 2 saline injections separated by a 2-hour interval, to habituate for the apomorphine (or vehicle) injection on the last day. At the tenth day, animals (3 in each condition) were subjected either to an apomorphine or vehicle injection.

The apomorphine solution consisted of 1 mg/mL apomorphine and 0.2 mg/mL ascorbic acid in 0.9% NaCl at pH 7.4. Controls were injected with a saline solution (0.9% NaCl) for the first group, and the other groups were injected with vehicle solution containing 0.2 mg/mL ascorbic acid in 0.9% NaCl.

3.4. Lateralized motor learning assay

3.4.1. Experimental setup

Animals were subjected to a self-operant lateralized motor learning task. In this task, animals are rewarded when they press a lever once or 4 consecutive times, as explained in the **Section 3.4.2**. Due to the position of the lever at a corner of the behavior box and to its gradual retraction, the task becomes achievable with only one forepaw as training progresses, thus becoming a lateralized task.

Training and habituation procedures were carried out in 6 identical custom-made acrylic 14x16 cm boxes. These boxes are placed inside of larger sound attenuating boxes, isolating exterior lights and noise from the setup. The main areas of the box are:

- The lever area, located to the right or left of the reward-delivery magazine. The lever is mobile in the vertical axis, made of clear acrylic, and its retraction is achieved by increasing the length of the screws that set the distance from the lever module to the acrylic wall.
- The magazine area, where reward is delivered. This area has a small cavity in the acrylic wall, from which reward is delivered via a perfusion system controlled by the solenoid valve.

Prior to training and after every lever retraction, the lever poke infra-red (IR) detectors were calibrated to ensure that accurate LP detection was achieved. Solenoid valves were calibrated prior to and occasionally during training, to always deliver a similar volume of 10% sucrose solution.

A computer running Pycontrol (**Fig. 7;** https://pycontrol.readthedocs.io/en/latest/), a Python based behavioral experiment control software, was used to control the related hardware breakout board, Pyboard (**Fig. 7**; Open Ephys, USA). This board is connected to different components of the box, via small devices called pokes (Open Ephys, USA). We used 2 pokes in each box:

- A poke that controls the box illumination by turning on and off an LED strip.
- A poke that detects lever presses and controls reward delivery. Reward delivery is achieved opening a solenoid valve (The Lee Company, USA) that is connected to the poke. The solenoid is in turn attached to a tube that connects to a syringe filled with a 10% sucrose solution. This poke has an IR beam break detector, composed of an IR LED emitter and an IR LED receiver facing each other, on each side of the back of the lever, to detect each lever press.

As illustrated in **Fig. 7**, the box is also composed of:

- A side camera (Point Grey Flea3, FLIR, USA), which records at a high frame rate (100 frames per second - fps), controlled by the data acquisition (DAQ) board (WEAR Basestation, made by the Champalimaud Research Hardware Platform) and the Bonsai software (https://open-ephys.org/bonsai).
- A top camera controlled only by Bonsai, which records at a regular frame rate (30 fps).

Besides controlling the acquisition by the side camera, the DAQ board is also connected to the Bonsai computer and the Pyboard, which is connected to Pycontrol on a different computer and can potentially synchronize the timestamps coming from Bonsai and Pycontrol (this feature was not used in our study).

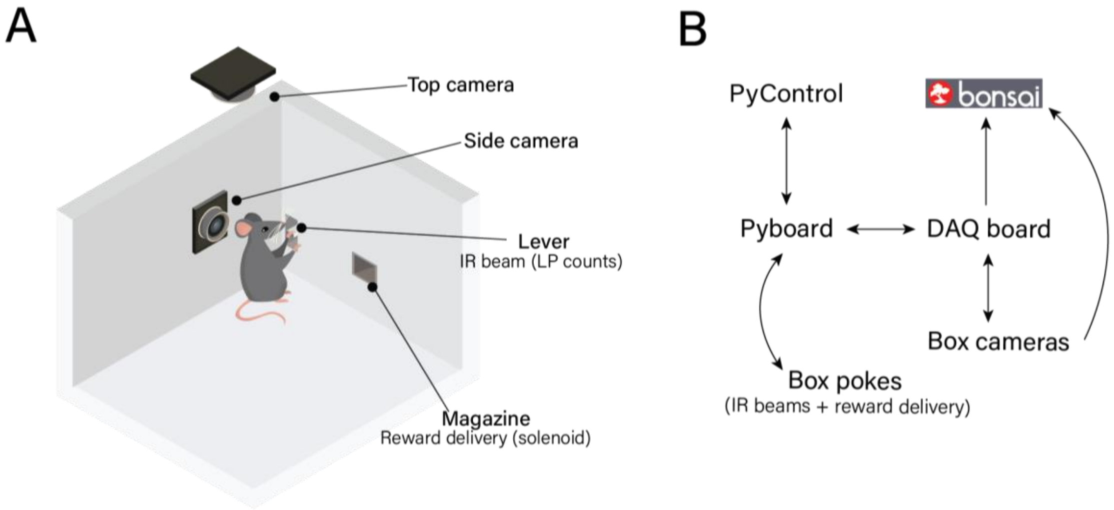

Figure 7 – Hardware and software schematics of the behavior box. (A) The box is composed of two cameras and two main areas – lever and magazine area. In the lever area, an IR beam detects LPs. In addition, in the magazine area reward is delivered through a small cavity in the wall. **(B)** The Pycontrol computer is used to control the related hardware breakout board, Pyboard. This board is connected to different components of the box, registering incoming input and delivering output through the reward delivery solenoid in the box magazine. The box also has a side camera, controlled by the DAQ board. The DAQ board (also connected to the Pyboard) and output of the cameras are registered by the Bonsai computer, which simultaneously captures the videos from the two cameras, and can align incoming timestamps from the two computers. Arrows denote incoming input and output to each component. *LP – lever press; IR – infrared.*

Bonsai is a modular open-source software for real-time video analysis and processing heterogeneous streams of data[117]. In this experimental setup, Bonsai collects the video data coming from both cameras, having no influence on the box hardware. It also processes incoming video, and outputs different data such as mouse location and presence in different areas of the box.

As for reinforcer delivery, this occurred automatically upon the lever press contingency was reached. This means that if a fixed-ratio 4 (FR4) schedule were being used, the reinforcer would be delivered upon the 4th lever press was detected by the IR detectors on the lever poke. It is important to point that Pycontrol will not consider lever presses during the time in which the reinforcer is being delivered at the magazine for its definition of sequences. Nevertheless, during performance analysis, described in **Section 3.6.1.**, all presses are counted and determined to be part of a sequence. This explains why, in our results (**Fig. 12.D**), the average number of LPs performed is higher than 120, the total number of presses needed to complete FR4 sessions.

3.4.2. Task schedule and performance

Twelve wild-type mice aged 10 to 11 weeks of age at the beginning of the experiment were used. Before training started, mice were placed on a food-deprivation schedule for 7 days, which continued for the following 10 days of training. Food deprivation protocols are frequently used in behavioral studies to initiate or maintain motivational states that are required during training. On the 7 days of food deprivation prior to training, mice were handled and habituated to the behavior box for a brief period, after which they were weighted and fed. This was achieved by providing mice with reduced portions of standard food pellets, weighing between 1.8 and 2.75 g, depending on the animal's weight changes from day to day, to maintain ~85% normal body weight (i.e., relative to their initial weight). Mice were divided in two groups of 6 animals, and each group was handled by a designated researcher throughout the whole experiment.

Mice were then subjected to training in the lever press task, performing two training sessions per day for 10 consecutive days (**Fig. 12.A**). Each morning, mice performed the first daily session, and were subjected to a saline (0.9% NaCl) habituation injection approximately one-hour post-training. This habituation was done to minimize the stress caused by the pentobarbital injection after the last day of training, which could affect IEG expression. In the afternoon, mice performed a second session, and were subsequently weighted and fed accordingly.

Training began with a session of magazine training on the first day, where mice were placed on the training chamber for 30 min during which 30 reinforcers (35 µl of 10% sucrose solution each) were delivered at the magazine at random times. In the following four training sessions a schedule of continuous reinforcement (CRF; one reinforcer delivered for each lever press) was applied. All CRF sessions lasted a maximum of 30 minutes or until 5 (first session) or 15 (second to fourth sessions) reinforcers were delivered. Mice then started a fixed ratio (FR) reinforcement schedule in which they received one reinforcer after every 4 lever presses (FR4), regardless of the time they took to do so. Fixed-ratios schedules of reinforcement are usually advantageous, given that they can achieve a higher number of responses in a shorter amount of time[118]. These sessions lasted a maximum of 30 minutes or until 30 reinforcers were retrieved. The first 2 sessions of FR4 had the lever completely extended (similar to CRF, protruding ~6mm from the lever window), the following 2 sessions presented the lever half retracted (leveled with the back opening of the lever window), and the final 10 sessions had the lever fully retracted (~6 mm retracted from the back opening of the lever window) (**Fig. 10**). The last lever position allows pressing with only one forelimb due to the position of the lever recess adjacent to one of the chamber walls (**Fig. 12.A**).

On the last day of the schedule, animals completed the last training session and were subjected to a lethal pentobarbital injection. This injection was given one hour after the last training session to maximize immediate early gene expression, according to previously established timelines[70,111].

3.5. Mouse perfusion and brain slice preparation

Behavior and pharmacologically treated mice were intraperitoneally injected with a lethal dose of the anesthetic sodium pentobarbital (100 µl/animal at 60mg/ml), 1h after the end of the last training session or 2h after apormorphine/saline injection. Once completely insensitive to a toe-pinch, mice were perfused through the heart with cold 4% paraformaldehyde (PFA). First, a cut on the skin was made, exposing the diaphragm. After cutting the diaphragm, the ribs were exposed, and the bottom ribs were cut until the heart was completely accessible. A small caliber needle (Terumo AGANI 23G or AgnThos 7900 feeding needle) connected to a pumping system was then inserted in the left ventricle. The right atrium was cut, a motorized pump was turned on and PFA was delivered for 5 minutes at a flux of 20 ml/min. Afterwards, the head was cut, the brains were dissected out and further fixated overnight in PFA before processing.

Brain coronal sections were cut using a Leica VT 1000S vibratome (Leica, Germany). All brains were processed within the following days of the perfusion. In brains of task trained animals, a cut on the right hemisphere cortex was manually performed with a blade throughout the entire anterior-posterior axis prior to brain slicing, for contralateral vs. ipsilateral hemisphere identification. The speed and vibration at which the slices were cut, as well as the section thickness, are described in **Table 3**. In general, thicker slices were cut for dendritic sine analysis and sparse labelling assessment, while 50µm slices were used for c-Fos expression analysis. Slices were stored in 12-well plates filled with an anti-freeze solution (30.6mM Na_2HPO_4, 11.4mM NaH_2PO_4, 20% ethylene glycol, 30% glycerol and 0.01% sodium azide) at -25°C, or with PBS with 0.01% sodium azide at 4°C, and covered in aluminum foil, until further use.

Table 3 – Details of brain slice preparation for each subject group.

Subjects	**Section thickness**	**Cutting speed and vibration**
D1-Cre (group 1; **Table 2**)	100µm	Speed – 6.5 Vibration – 4.5
D1-Cre (group 2; **Table 2**)	150 and 250µm	
A2A-Cre (group 3; **Table 2**)	200µm	
Behavior and apomorphine/saline injected controls	50µm	Speed - 4.5-6.5 Vibration – 6.5

3.6. Motor behavior analysis

To assess the level of learning and skill development during training, different metrics were extracted from camera and software data.

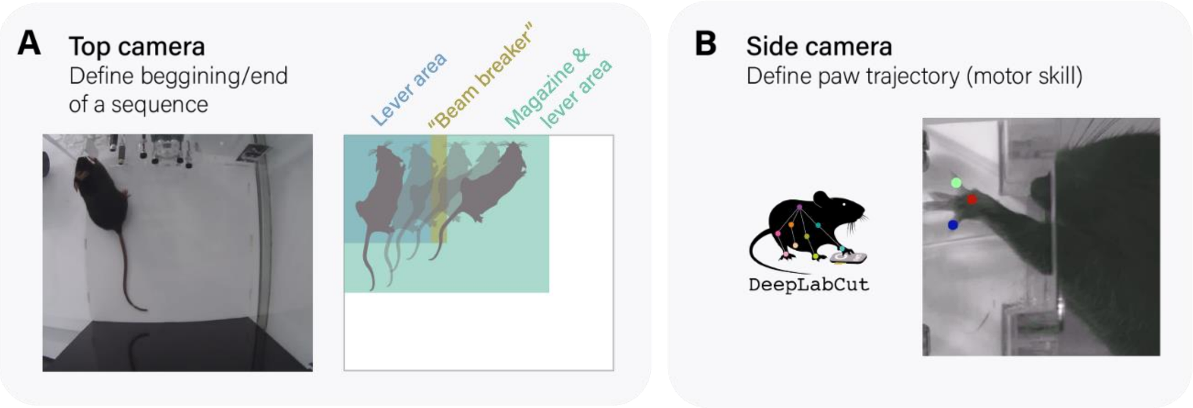

Figure 8 – Top and side camera data analysis. (A) Different areas of the box were defined on Bonsai, as well as the centroid of the mouse, allowing mouse tracking to define lever press sequences; the end of a sequence was defined as the last lever press prior to crossing the "beam breaker", while the beginning of a sequence was defined as the first press after the end of the prior sequence. **(B)** Side camera data was used to estimate paw trajectory using DeepLabCut. Forepaw labelling: paw centroid in red, first digit in blue and fourth digit in green.

3.6.1. General measures of performance

For the Bonsai workflow, two different source nodes were defined – one for the side camera, and one for the top camera. For the side camera, two 'Frame Counter' nodes output information into a 'CsvWriter' node. This information includes the index of each frame acquired as well as its timestamp, and information relative to frame loss during video acquisition. For the top camera, multiple nodes were defined sequentially to analyze incoming video on the position of the mice within the box. Briefly, the video was transformed into grayscale and a threshold was defined, such that a binary region corresponding to the mice could be defined using a 'BinaryRegion Analysis' node. By doing so, a centroid of the mice and its orientation could be determined. In addition, different regions of the video were cropped as to obtain different box areas, the lever area, the 'beam breaker', and a larger area containing the magazine and lever areas, as shown in **Fig. 8.A**. Both the centroid coordinates and the pixel intensity information relative to the different areas defined were then saved to two different comma-separated values (CSV) files. For both cameras, a 'VideoWriter' node outputs the incoming video into videos. A third input node was defined as the DAQ board, which could integrate the Pycontrol computer timestamps with the Bonsai computer (not acquired during this experiment). From Pycontrol, a text file was automatically created with timestamp information relative to each press and reward delivery at the end of each session.

All performance data were analyzed in MATLAB 2019a (https://www.mathworks.com) using previously custom-built scripts. Data from each video (CSV files from Bonsai and text files from Pycontrol) were used to determine the length of each sequence (number of presses), as well as total number of presses, session duration, and other measurements. First, the start and end of each session were defined as the highest increase and decrease difference, respectively, in pixel brightness, respectively, between two given frames of the top camera video. These signal the exact start and end of the session, as they correspond to the turning on and off of the box LED (controlled by PyControl). These start and end timestamps were then used to align all the lever press frames in each session between Bonsai and PyControl. The start and end of each lever press sequence, on the other hand, were defined using the 'beam breaker' area, where a difference in pixel brightness occurred every time the mouse centroid crossed it. Thus, each sequence starts at the first lever press after the mouse crosses the 'beam breaker' and ends at the last lever press before it crossed the 'beam breaker' again. Multiple videos across trials were manually revised to make sure that the threshold for this analysis allowed for accurate results. In some sessions, due to inadequate closing of the boxes, light was lower/higher inside the box; in these situations, analysis was run individually with different thresholds to achieve accurate results (as determined by the experimenter by video inspection). Intersequence inter-press intervals were calculated as the time interval between the last lever press of one sequence and the first lever press of the following sequence. Intra-sequence inter-press intervals were calculated as the time interval between each lever press in a sequence.

Plotting of the results was done using both MATLAB and GraphPad Prism 8 (https://www.graphpad.com/).

3.6.2. Paw trajectory analysis using DeepLabCut

As this task involves learning of a motor skill, we further inspected skill refinement by analyzing paw trajectory variability across different FR4 sessions with the lever fully retracted. All animals were considered for this analysis, except for two – one that learned the task with the wrong paw, and another one that was able to initially associate lever pressing with reward delivery, but that stopped being able to obtain rewards as the task became more challenging (performing no presses upon full lever retraction).

To analyze paw trajectories, we used DeepLabCut (DLC; https://github.com/DeepLabCut/DeepLabCut), a software used for pose estimation based on transfer learning with deep neural networks[119,120]. This tool allows for a fast, unbiased and efficient labelling of video frames based on a frame-by-frame identification of the body parts of interest, which in our case is the forepaw pressing the lever.

Videos from the side camera were horizontally flipped for the boxes bearing the lever window to the right of the reward delivery magazine. This ensured that the lever was always on the left side during video frame analysis, for all boxes. For this, we used ffmpeg (https://ffmpeg.org/) with a 'veryslow' preset to avoid losing frame information. Some videos were not analyzed due to incorrect angle and/or camera displacement throughout the session.

Video frame selection for training of the neural network was achieved by using the methods provided on the DLC graphical user interface. Over 300 frames were extracted from across all sessions (of all individuals) for the full duration of each session, to capture different light conditions, camera angles and individual variability. Images were extracted using both 'k-means' and 'uniform' algorithms, resulting in enough frames that capture the full breadth of the behavior repertoire. Each frame was labelled by the same experimenter, using the same criteria throughout the entire process. We chose to label 3 parts of the forepaw – the paw centroid, the first digit (as viewed from the camera side), and the fourth digit (**Fig. 8.B**). On a given frame, labelling for each marker was only done if the body part was clearly visible and distinguishable.

Training was performed on the Google Colab platform (https://colab.research.google.com/). A notebook (web application for creating and sharing documents that contain live code) created by DLC was used with minor alterations to its code. A training dataset was created using the default ResNet-50 convolutional neural network and imgaug library for image augmentation. The default data shuffle was used for network training, and this step was run for over 1 million iterations, until the cross-entropy loss plateaued at 0.0012. In machine learning, the cross-entropy loss measures the performance of a classification model, and its output is a probability value between 0 and 1; a perfect model would have a cross-entropy loss of 0. At the end of training, the classification error of the model on the same data it was trained on, known as train error, was of 1.54 pixels. This value was the same with and without a p-cutoff (threshold for the likelihood of the detection, ranging from 0 to 1) of 0.6, indicating that a good generalization and accuracy (pixel error below 2 pixels) was reached[119]. At last, videos were analyzed based on the last training checkpoint ('snapshot') of the trained network, either on Colab or on the Champalimaud Research Cluster (https://www.fchampalimaud.org/platforms/single/scientific-software). Total trajectories and the final labeled videos were created inside Colab.

Output files from DLC were then further analyzed on Matlab using custom built scripts. Briefly, 70 frames around the lever press frame (corresponding to the lever press detection timestamp by the lever poke) were analyzed to determine the paw centroid X and Y coordinates (**Fig. 8.B** – red circle). First, points with a p-cutoff smaller than 0.8 were linearly interpolated based on adjacent points. Then, trajectories were aligned to their minimum value on the X axis and trimmed to account only for paw movement inside the lever press area, by limiting the X axis of the video on the right side to the acrylic wall. If after this, a press had less than 10 coordinate points in X and Y, it was not analyzed further; only few presses were lost in some videos and represented less than 2% of all presses. For presses in sequences, trajectories were further trimmed to isolate each press correctly by identifying data points where movement direction was reversed in the X axis, which indicates the beginning of a new lever press. Each trajectory was then linearly interpolated in X and Y to have 45 trajectory points. Velocity in each axis was calculated as the mean of the absolute value of displacement (in pixels) between consecutive frames.

Trajectory variability was analyzed by different measures:

- Standard deviation was calculated in each point to every other corresponding point in all trajectories, in each axis.
- Frechet distance, a measure of similarity between curves, was calculated in a similar manner (point-by-point). Given two sets of points, A and B, that define curves on the same axis, the Frechet distance is the minimum cord-length sufficient to join a point traveling forward along A and one along B, although travel rate may not be necessarily uniform. We

measured the Frechet distance in each axis using a Matlab implementation of discrete Frechet distance (https://www.mathworks.com/matlabcentral/fileexchange/31922-discrete-frechet-distance) [121].

- Sum of Euclidean distances was calculated using the Dynamic Time Warping function available on the Matlab Signal Processing Toolbox. This function stretches two vectors onto a common set of instances such that the sum of Euclidean distances between corresponding points is smallest. A mean trajectory was calculated for each session using all trajectories; the Euclidean distance was then measured between every non-interpolated (raw) trajectory to the mean session trajectory upon interpolation.

For the single press versus sequence press analysis, depicted in **Fig. 16**, if the number of presses in sequence was higher than the number of single presses, then a number of presses in sequence equal to the number of isolated presses was randomly selected for analysis (using the Matlab 'rand' function). If the number of single presses was higher, the opposite was done. Then, each measurement was calculated as mentioned above, within all presses in sequences and within all single presses.

Plotting was done using both MATLAB and GraphPad Prism 8.

3.7. Immunostaining and imaging

3.7.1. IEG immunostaining

Throughout this work, different immediate early genes (IEGs) and antibodies against them were tested. The staining protocol and antibody concentrations were optimized to achieve the best signal to noise ratio. The optimized protocol was the following: slices were washed three times at room-temperature (RT) with Tris-buffered saline (TBS) for 10, 20 and 30 minutes, after which the slices were blocked in TBS 0.3% Triton-X1000 (TBS-T) containing 10% bovine fetal serum albumin (BSA, Sigma Aldrich) and 2% normal goat serum (NGS, Sigma Aldrich) for 1 hour. Incubation with the primary antibody (**Table 4**) was done in TBS-T with 10% BSA and 0.01% sodium azide (Sigma Aldrich) for 24 or 48 hours at 4°C. After this period, slices were washed with TBS for three consecutive washes of 10, 30, and 40 minutes at RT. A second blocking step was done by incubating slices in TBS-T with 10% BSA for 2 hours at RT. Then, slices were incubated with the respective secondary antibody at 1:1000 in TBS-T with 10% BSA and 0.01% sodium azide for 2 hours at RT. Three consecutive washes with phosphate buffer (PB) were then performed for 10, 30 and 40 minutes. At last, slices were stained for 15 minutes with DAPI (4′,6-diamidino-2-phenylindole) at 1:1000 in PB. After a brief rinse in PB, slices were mounted on glass coverslips (Deckglaser, 24x50mm, #1.5 thickness) with Mowiol mounting medium (refractive index 1.41-1.49). Slides (Superfrost PLUS, Thermo Scientific) were then mounted and sealed with clear nail polish and stored in an opaque box at 4°C. Slices from task trained animals were mounted in order to have the right hemisphere (identified with a cut) aligned to the right side.

Table 4 – Primary antibodies optimal concentration for the detection of IEG's.

Primary antibody	Concentration	Secondary antibody partner
Rabbit anti-c-Fos monoclonal (Cell Signalling, #2250)	1:500	Goat anti-rabbit Alexa Fluor 647, 594 or 488
Rabbit anti-c-Fos polyclonal (Synaptic systems, #226003)	1:1000	
Rabbit anti-Arc polyclonal (Synaptic systems, #156003)	1:500	
Mouse anti-Arc monoclonal, pre-conjugated with Alexa Fluor 647 (Santa Cruz, #17839)	1:100	None

3.7.2. Confocal microscopy

Images were acquired using a Zeiss LSM 710 confocal microscope. As for the laser settings, the pinhole was kept between 1-1.54 Airy Units. When acquiring red or far-red wavelengths (IEG detection using Alexa 647 or Alexa 594), simultaneous acquisition was performed on the red and blue (DAPI) channels, and detection spectra were defined with no overlap between the different fluorophores (**Table 5**). The blue laser (Diode 405-30) power was kept at 1-6%, while the red (DPSS 561-10), far-red (HeNe633) and green (Argon 488) lasers, were kept at 25-50%. Overview images of whole slices were done using a Plan-Apochromat 10x lens of NA 0.45 (Zeiss), by acquiring a tiling of the best focused slice in Z, with a pixel size of 790nm and a dwell time of 1.79 µsec. Image stacks at higher resolution were done using a Plan-Apochromat 20x lens of NA 0.8 (Zeiss): for sparse labelling z-stacks (**Fig. 29**), acquisitions were performed with a pixel size of 470 nm, Z-step of 10 µm, 2x zoom and a dwell time of 1.08 µsec; for IEG visualization (**Fig. 20**), acquisitions were performed with a pixel size of 690 nm, Z-step of 0.5 µm and a dwell time of 1.58 µsec. All acquisitions were acquired using bidirectional laser acquisition and a frame averaging of 2.

Histogram adjustments for final image exports, maximum intensity projections of Z-stacks, as well as stitching of tiling acquisitions, were done using the Zeiss ZEN Blue software (https://www.zeiss.com/microscopy/int/products/microscope-software/zen.html) or ImageJ (https://imagej.net/Fiji). Brain atlas alignment was performed by aligning the best corresponding slice vector available on the Allen Mouse Brain Atlas application program interface (http://help.brain-map.org/display/mousebrain/API).

Table 5 –DAPI and secondary antibody fluorophores excitation and emission peaks.

Flurophore	Excitation peak (nm)	Emission peak (nm)
Alexa Fluor 488 (Goat anti-rabbit, Invitrogen #A21245)	490	525
Alexa Fluor 594 (Goat anti-rabbit, Invitrogen #A11037)	590	617
Alexa Fluor 647 (Goat anti-rabbit, Invitrogen #A11034)	650	665
DAPI	358	461

For dendritic spine acquisition, we used a Plan-Apochromat 63x oil-immersion (refractive index – 1.51) lens of NA 1.4 (Zeiss). This allowed for a Nyquist sampling, i.e., the minimal sampling density needed to capture all information from the microscope into the image, of 45mm and 137nm Z-steps when imaging EYFP[122]. The typical dimensions for the head, width and neck dendritic spine are around 0.2-1µm[81]. Thus, with our setup, we were able to achieve the resolution needed to accurately image these small structures. The final sampling dimensions used in this work were optimized for best results and speed. First, a neuron was selected following visual inspection to ensure it was isolated enough from other neurons and its projections were healthy looking. Then, a low-resolution image stack, with a pixel size of 220 nm and 1.5 µm Z-steps, was acquired to obtain an overview of the neuron. Dendritic segments were then acquired in an unbiased way, by randomly choosing segments at different distances to the soma, whenever these were distinguishable from other neurons projections. These images were taken with a pixel size of 50 nm and 100 nm Z-steps, and laser acquisition was unidirectional. The pinhole was kept at 1.01 Airy Units in both overview and segment acquisitions. Additionally, dwell time was set at 1.45 µsec, frame averaging at 2, digital zoom at 3, and the laser power at 30-35%. The frame size was kept at 45x45 µm, and thus, different segments had different lengths depending on their trajectory. A few segment acquisitions had more than one segment from the same neuron and were later cropped for separate analysis using Fiji (https://fiji.sc/).

3.7.3. Slidescanner microscopy

Images were acquired using the Zeiss AxioScan Z1 microscope. For this type of acquisition, the Plan-Apochromat 10x lens of NA 0.45 (Zeiss) was used. The far-red wavelength laser (Colibri.7 630) exposure time was kept at 400ms, for c-Fos imaging. Tiling images of whole slices were done by acquiring with a resolution of 0.6µm per pixel on the full depth of the slice (50µm) with 2.5 µm Z-steps. The output images were transformed into a 2D maximum intensity projection images automatically by the microscope software.

3.8. C-fos expression analysis

Upon acquisition, output images from the Axioscan microscope, which are stored in a single file for each microscope slide, were separated into individual files to obtain a single brain slice per file using the ZEN Blue software. Files were named individually in ascending order from anterior to posterior location and stored in a different folder for each brain.

Cell detection and analysis was performed using BrainJ (https://github.com/lahammond/BrainJ), a macro for ImageJ which combines a series of software tools[123]. This software allows for multi-step pre-processing and alignment of the slices, followed by re-scaling and alignment of the dataset to a brain atlas, and cell detection and registration to each brain region (**Fig. 9**).

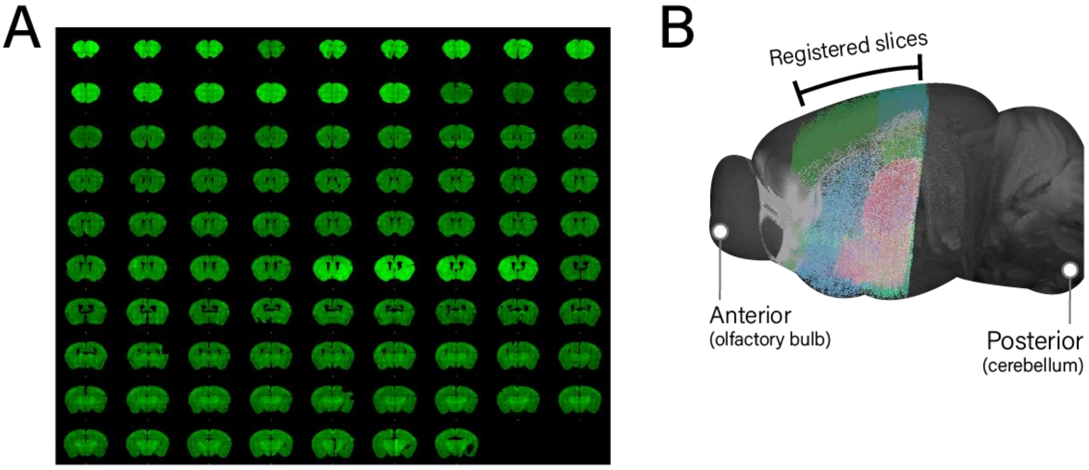

Figure 9 – Processing and atlas registering of brain slices in the BrainJ pipeline. (A) Auto-generated montage of ordered brain slices of a single brain (prior to further processing), showing c-Fos expression. **(B)** Anterior-posterior span of registered slices of a single brain, corresponding to ~5 mm; the small colored dots correspond to detected c-Fos positive cells.

On the first step (‘Set Experiment Parameters’), experiment parameters were set according to the characteristics of our datasets: ‘Lateral resolution’ – 1 µm, ‘Final resolution’ – 2 µm, ‘Section thickness’ – 50 µm, ‘Background Intensity’ – 100, and the ‘Reformat Sections’ step was run. After this step, images were corrected when needed if debris/parts of neighbouring slices were present in the c-Fos channel. Additionally, false positive staining of the tissue bordering the ventricles was removed by manually removing them at this stage. Badly damaged slices were replaced during the third step (‘Section Flipper and Replacer’). Differences in intensity (as observed in **Fig. 9.A**) are corrected later in the pipeline through the Attenuation Correction plugin (https://imagejdocu.tudor.lu/plugin/stacks/attenuation_correction/start).

The analysis settings (step 4) were set as follows: ‘Reference section for registration’ – 40, ‘Background removal prior to segmentation’ – 7 pxs. For cell detection, the ‘Machine Learning Segmentation with Ilastik’ method was used for channel 2 (c-Fos), with the following settings: ‘Minimum intensity threshold’ – 20, ‘Minimum cell area’ – 30.

The chosen method of cell detection allows for pixel-to-pixel classification and cell detection according to a trained classifier. The ‘Ilastik_Project_Channel_2’ file, available on the BrainJ github repository, was trained on Ilastik (https://www.ilastik.org/) using images obtained from BrainJ (on ‘Other tools’). This way, Ilastik training images were pre-processed for background removal (with a radius of rolling ball with 7 pixels) using the same settings as images that were later used for cell detection. Two images from each condition were uploaded to this file (task-trained, apomorphine, saline; total of 6 images), and corresponded to images equally spaced in the anterior posterior axis in all conditions. No alterations were made to the default ‘Feature Selection’ already in the project file. The classifier was trained for the ‘Background’ and ‘Cells’ labels already in the file, by two different researchers, to try to achieve a more unbiased training of the classifier. After this, the project was saved and copied to the ‘Ilastik_projects’ folder created by BrainJ in each brain folder. For the ‘Registration and Atlas Analysis’ step, the template atlas used was the default Allen Brain Atlas Common Coordinate Framework 2017 (ABA CCF 2017, Allen Institute). The resulting registration of cells to the atlas can be observed in **Fig. 9.B**.

Posterior analysis and plotting were done using both MATLAB and GraphPad. The number of cells detected in each mouse was automatically pulled from BrainJ output CSV files using custom built Matlab scripts. The ABA CCF region ID numbers for each of the regions studied in this project can be found on **Annex II**. For regions containing more than 1 layer, values displayed are the sum of all cells in all layers. Percentage of cells expressing c-Fos in each hemisphere (contra vs ipsi for task trained, left vs right for controls) (**Figs. 25 & 26**) were calculated as a ratio of the number of positive cells in one hemisphere divided by the total number of positive cells. Differences in expression of c-Fos between hemispheres (**Figs. 25 & 26**) were calculated in reference to the number of cells expressing c-Fos in the contralateral hemisphere versus the ipsilateral hemisphere in task trained animals, as follows:

$$\%\ difference = 100 - \frac{(nr\ cells\ contralateral/left \times 100)}{nr\ cells\ ipsilateral/right}$$

3.9. Dendritic spine image analysis

Dendritic segment images were deconvolved using the Huygens software (https://svi.nl/Huygens-Professional). Deconvolution is a process that improves signal and resolution by making use of the theoretical point spread function offered by the microscope lens and image acquisition parameters. A custom deconvolution template was used with the following settings: ‘Algorithm’ – Good’s roughness maximum likelihood estimation; ‘Maximum iterations’ - 40; ‘Mode’ – optimized; ‘Signal to noise’ - 25; ‘Background’ - auto; ‘Bleaching correction’ – no; ‘Brick mode’ – slice by slice. After deconvolution, images were manually adjusted in Fiji for optimal brightness and contrast before spine reconstruction was performed.

Two softwares were tested for dendritic spine reconstruction – the open source Vaa3D (https://github.com/Vaa3D/release/releases/) - and the commercially available Neurolucida360 (https://www.mbfbioscience.com/neurolucida). A total of 15 segments from 2 mice were used for spine reconstruction – 10 from 3 different neurons of one animal, and 5 from one neuron of a different animal. Both animals were D1-Cre mice (**Table 2** - group 1 and 2), consisting of saline controls used for apomorphine experiments.

On Vaa3D, dendritic segments were automatically traced using the ‘Neuron2’ tracing method. ‘Background threshold’ was set at 20-40, depending on image contrast, and ‘Length-threshold’ at 25-60, depending on whether the segment had bifurcations or not. After achieving a good segment detection, spine detection was performed according to the spine detector tool user guide[124]. Briefly, dendrite traces were sorted and resampled. Afterwards, a new project was created, and the following parameters were used for spine detection: ‘Background threshold’ – 35, ‘Maximum spine volume’ - 8000 voxels, ‘Minimum spine volume’ - 30 voxels, ‘Maximum spine distance to surface’ - 60 pixels, ‘Maximum spine width’ - 100 pixels. These parameters were used throughout all segments and usually detected 3 times more putative spines than the accepted spines after visual inspection. Incorrect detections, usually consisting of portions of dendritic shaft and/or spines from neighboring dendrites to the one being analyzed, were removed. Detected spines with incorrect volume were adjusted manually. After proofreading, an excel file containing the accepted spine parameters was saved automatically. Dendritic segment information was retrieved from the ‘Global features’ tool.

With Neurolucida360, imported images were scaled manually, according to acquisition settings. On the 3D environment, dendrites were traced with an automatic detection tool using the ‘Voxel Scooping’ method. For a more accurate detection, detection seeds were manually adjusted (added/removed) prior to tracing. After this, tracing was manually adjusted with point precision if detection was inaccurate. Then, spines were reconstructed using the automatic spine detection tool. For this, the following parameters were used: ‘Outer range’ - 3.5µm, ‘Minimum height’ - 0.3µm, ‘Detector sensitivity’ - 125%, ‘Minimum count’ - 10. After visual inspection, a small number of spines were manually removed or added if necessary. Additionally, detected spines were manually merged whenever these corresponded to different parts of the same spine. After saving the dendrite and spine tracing, the file was opened in Neurolucida Explorer and Batch analysis was performed for the following options: 'Segment – Dendrites', 'Tree spines – Dendrites', 'Spine details – Automatic'.

Data from all segments was analyzed using custom-built scripts in MATLAB 2019a. For morphological classification of spines (**Fig. 34**), spines were classified into each subtype based on previously established ratios in hippocampal CA1 neurons[125], that have also been applied to studies in MSNs[105,126], using Neurolucida320 output data. Briefly, spines with less than 3μm in length were classified as mushroom if the length>neck and head>neck; stubby if the length≤neck; thin if length>neck and head≤neck. Spines longer than 3μm were classified as filopodia. Plotting was done using both MATLAB and GraphPad Prism 8.

3.10. Statistical analysis

Statistical analysis was performed using GraphPad, to determine the significance of differences found between groups/conditions. Data is presented as mean ± standard error of the mean, unless otherwise stated. Normal distribution of data analyzed by parametric tests was confirmed using one-sample Kolmogorov-Smirnov test with a 5% significance level whenever possible, or otherwise assumed to be normal without a formal test. When analyzing task parameters, normal distribution was assumed, and one-way repeated measures ANOVA was performed when comparing all sessions of task performance. Mixed effects test was performed whenever there was missing data. The statistical test used in each experiment is defined in the corresponding figure legend. Differences were considered statistically significant when the calculated p-value was <0.05.

4. Results

4.1. Lateralized lever press motor learning task

4.1.1. Mice learn a lateralized lever pressing task

In this experiment we measured the ability of mice to learn a lateralized lever pressing task, in which a reward is obtained upon pressing a lever for a contingent number of times. The task is designed to allow only for one paw to reach the lever, which allows for the study of movement sequences performed by a single forelimb. Prior to training, mice were placed in a food deprivation schedule to maintain exploratory behaviors and motivation. Mice stabilized their weight loss prior to beginning of task, and steadily maintained their weight during task at around 85% initial body weight (**Fig. 10**).

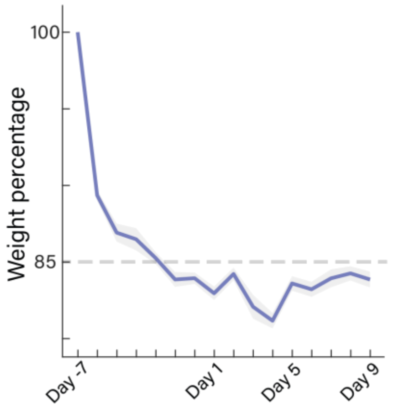

Figure 10 –Weight percentage of mice placed on a food deprivation schedule. Task trained mice were placed on a food deprivation schedule and were weighted and fed daily according to their weight loss, to maintain around 85% of their normal body weight. Mouse weight is normalized as percentage of the initial weight before food deprivation was initiated. The day the task started was defined as day 1. Data is presented as mean ± SEM (n=12).

Each chamber is equipped with one retractable lever on one side (right or left) of the magazine, and training starts with lever protruding into the box (**Fig. 11** – "out"). Animals were introduced to the task through a magazine training, in which 30 reinforcers (10% sucrose) were delivered at random times with no action contingency (i.e., no lever presses required). Animals were then trained for 5 sessions of continuous reinforcement (CRF), in which a reinforcer was delivered upon 1 lever press for a maximum of 5 and 15 presses (**Fig. 12.A** – blue). After, animals were trained in a fixed-ratio 4 (FR4) schedule for 14 sessions, where a reinforcer is delivered upon pressing 4 times, with no time contingency to do so, for a maximum of 30 reinforcers per session. After 2 sessions of FR4 with the lever "out" configuration (**Fig. 12.A** – green), the lever was retracted to its "mid" position for 2 sessions (**Fig. 12.A** – purple), in which the lever is leveled with the back opening of the lever window (**Fig. 10** – "mid"). After, the lever was retracted to the "in" position (**Fig. 11** - "in") until the end of training (**Fig. 12.A** – beige). The maximum session duration was set at 30 minutes, or until animals received all reinforcers available.

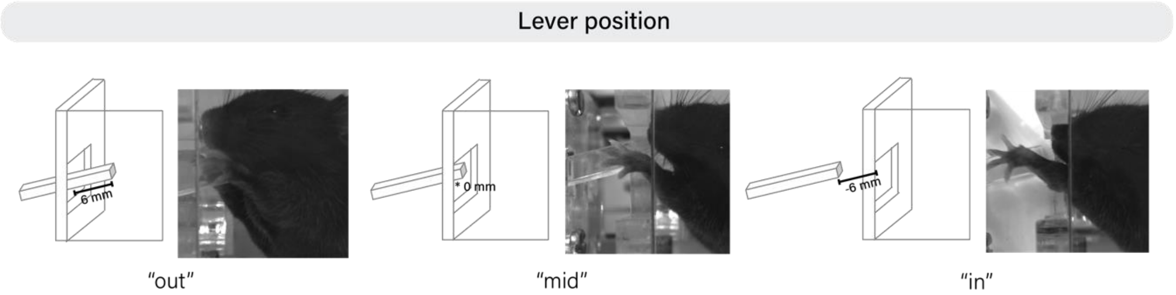

"out" "mid" "in"

Figure 11 – Schematics and images, of the first ("out"), middle ("mid"), and fully retracted ("in") lever position.

To evaluate task learning and motor performance, several aspects of the behavior were evaluated. Out of the 12 mice trained in the task, only one was unable to learn it: while it seemed to initially associate lever pressing to reward delivery, it never completed a CRF session and quickly lost motivation to press. The other 11 mice learned to perform the task, progressively adapting to changes in task difficulty. The number of animals performing at least one lever press progressively increases during the first sessions, and animals continue to engage in the task upon the first lever retraction to the 'mid' position. Lever retraction to the "in" position, led to a decrease in the number of animals performing at least one lever press and in the total number of presses, that then gradually recovered with training (**Fig. 12.B**). Likewise, mice start increasing the number of presses in FR4 schedule, but decrease upon full lever retraction, and progressively increase again until the end of training ($F_{17,170}=11.02$; $p<0.001$) (**Fig. 12.D**). The time needed until session completion decreased ($F_{17,170}=3.932$; $p<0.001$) with training, particularly in the sessions after the last lever retraction (**Fig. 12.C**). The intersequence interval, i.e., the interval between the completion of one sequence of 4 lever presses (or 1 press for CRF sessions) and the beginning of the next one, also decreased, with some variability until the end of FR4mid sessions, increased upon full lever retraction and decreased again on the last training sessions ($F_{17,145}=2.267$; $p=0.05$) (**Fig. 12.E**).

Examining sessions from FR4 schedule only, we observed that mice increased the number of sequences performed per minute ($F_{13,130}=5.889$; $p<0.001$) (**Fig. 13.A**). However, they did not significantly increase the number of presses per sequence, and most animals did not reach the desired criteria of sequences of four presses ($F_{13,118}=1.460$; $p=0.1427$) (**Fig. 13.B**). This means that to obtain a reward, most mice were performing more than one sequence of less than four presses. Taking a closer look at the inter-sequence interval, we observe considerable session-to-session variability and although there was a decreasing trend, it was not statistically significant ($F_{13,115}=1.515$; $p=0.1221$) (**Fig. 13.C**). Consistently, the coefficient of variation of the inter-sequence interval did not significantly decrease with training ($F_{13,115}=0.5460$; $p=0.8364$) (**Fig. 13.D**).

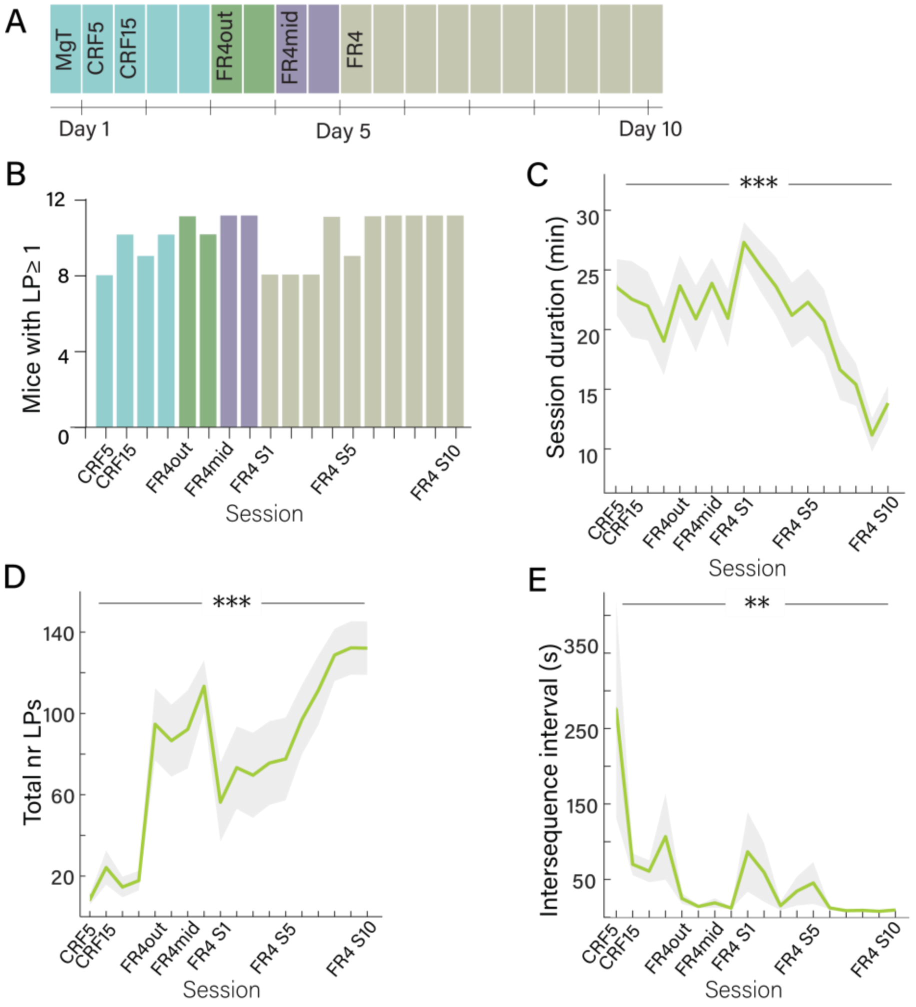

Figure 12 – Mice increase the number of presses and decrease the time needed to complete the task throughout training. **(A)** Diagram of training schedule. **(B)** Number of mice that pressed the lever one or more times during the corresponding session. **(C)** Total time until task completion was achieved. **(D)** Total number of lever presses (LPs) per session. **(E)** Median interval between two lever press sequences. In **(C)** and **(D),** data is presented as mean ± SEM, and in **(E)** as median ± SEM (n=11). Differences between sessions for each parameter were analyzed by performing a repeated measures one-way ANOVA for **(C-D)** (*** p≤0.001), and a Mixed-effects test for **(E)** (** p≤0.01). *MgT – magazine training; CRF – continuous reinforcement; FR4 – fixed-ratio 4; LP – lever press; S1-S10 – session 1 to 10.*

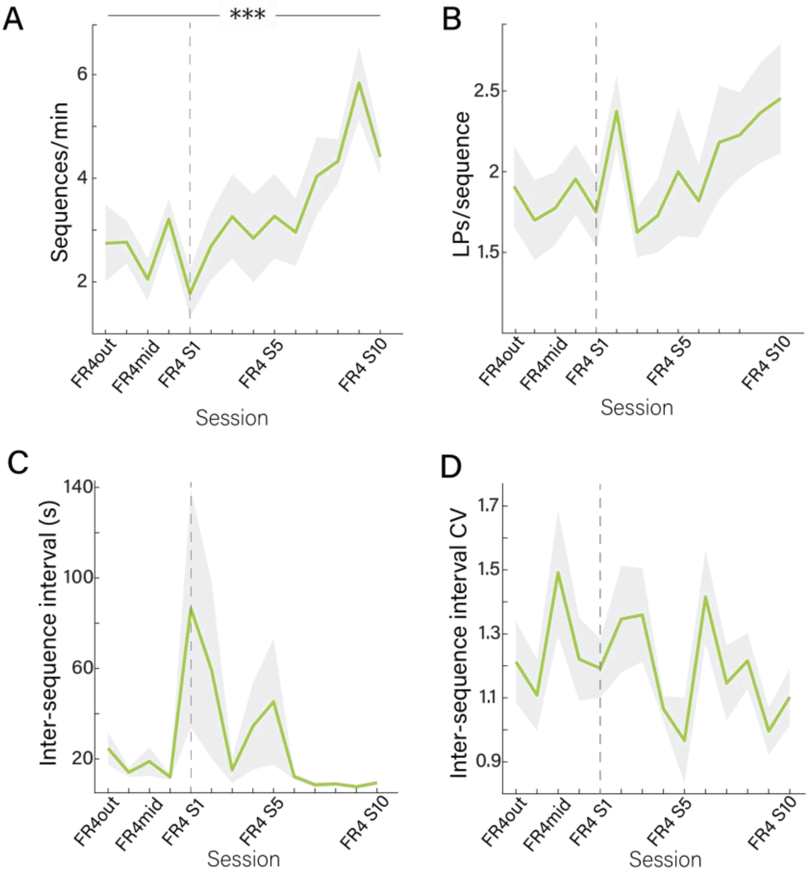

Figure 13 – Mice do not significantly increase the number of lever presses per sequence. (A) Number of sequences performed per minute. **(B)** Average of the median number of lever presses (LPs) per sequence for each mouse. **(C)** Intersequence interval for each session. **(D)** Intersequence interval coefficient of variation (CV) per session. Results are presented as mean ± SEM. Differences between sessions for each parameter were analyzed by performing a repeated measures one-way ANOVA for **(A)** (*** $p \leq 0.001$), and a Mixed-effects test for **(B-D)** (non-significant). Dashed lines mark the first session upon full lever retraction. *FR4 – fixed-ratio 4; LP – lever press; S1-S10 – session 1 to 10.*

Upon lever retraction, the percentage of non-isolated lever presses, i.e., presses in sequences, varies slightly across sessions, but does not significantly increase ($F_{9,79}=1.993$; $p=0.0510$) (**Fig. 14.A**). We observed that the within-sequence inter-press interval also did not significantly decrease with training ($F_{9,74}=1.867$; $p=0.0704$) (**Fig. 14.B**), neither did its coefficient of variation ($F_{9,74}=0.5460$; $p=0.8364$) (**Fig. 14.C**). At last, we looked at the distribution of sequences by the number of lever presses in that sequence. No significant difference was found in the overall distribution of presses in throughout sessions ($F_{2,200}<0.1$; $p>0.999$), but a significant difference was observed between groups of presses/sequence ($F_{7,200}=38.87$; $p<0.001$). The interaction between variables was found to be non-significant ($F_{14,200}=1.580$; $p=0.0871$). However, we observed that there was a significant decrease in the number of sequences containing a single lever press, when comparing the first to the last session ($p=0.0219$). A non-significant increase was also observed progressively through training in sequences containing 3-4 LPs (**Fig. 14.D**).

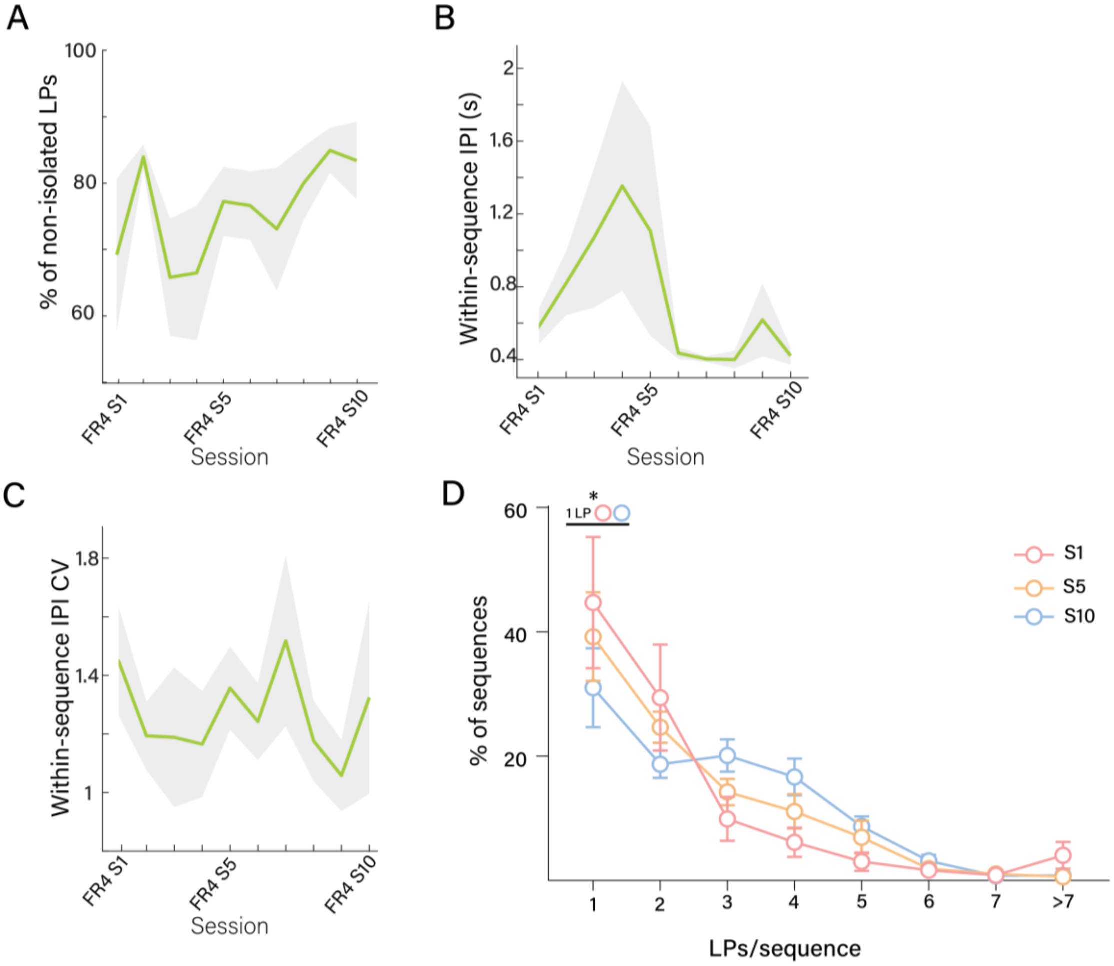

Figure 14 – Mice do not significantly decrease the number of isolated lever presses (LPs) and within-sequence variability. (A) Percentage of non-isolated presses. **(B)** Average within-sequence inter-press interval (IPI; seconds) per session. **(C)** Within-sequence IPI coefficient of variation (CV) per session. **(D)** Distribution of the percentage of sequences with different number of presses per sequence for sessions 1, 5 and 10. Values are presented as mean ±SEM. Differences between sessions for each parameter were analyzed by performing a Mixed-effects test for **(A-C)** (non-significant) and a two-way ANOVA for **(D)** (S1 vs S10 1-LP; * $p \leq 0.05$). *FR4 – fixed-ratio 4; IPI – inter-press interval; LP – lever press; S1-S10 – session 1 to 10.*

Overall, our results suggest that mice can learn a forelimb lateralized lever press task, adapting to task difficulty imposed by lever retraction. Animals increase the number of lever presses performed in a sequence, while decreasing the time they take to do so. Still, mice were not able to reach the four presses per sequence criteria in FR4 sessions, performing presses in smaller bouts to obtain 1 reinforcer. The within-sequence press inter-press interval did not decrease or reduce variability upon full lever retraction. Thus, under this schedule, although animals learn to perform the task, they do not reduce variability in some dimensions.

4.1.2. Shaping of movement kinematics with task learning

With learning, movements tend to get stereotyped, and variability reduced[55,127]. To examine whether mice in this task reduced movement variability, as a way of assessing skill development, we analyzed lever presses trajectories upon full lever retraction. We used DeepLabCut, a software that performs frame-by-frame labelling of body parts of interest, to analyze the high temporal resolution videos from the side cameras of the boxes (**Fig. 15.A**), enabling us to capture the trajectories with a good number of coordinates. DeepLabCut outputs a set of X and Y coordinates of each video frame, for the labeled body part, which in our case was the paw centroid.

We hypothesized that, with training, animals would reduce variability in lever pressing, while increasing the velocity at which they do so. Overall, mice increased the velocity at which they pressed the lever, as assessed by the mean pixel displacement of trajectories through sessions ($F_{1.538,\ 20.85}$= 6.268, p=0.0115), and a significant difference was found between the X and Y components ($F_{1,\ 18}$= 18.33, p<0.001) (**Fig. 15.B**). We quantified three different parameters as a measure of trajectory variability: the standard deviation (STD), the Frechet distance and the mean Euclidean distance. We found that the STD of trajectories within each session increased throughout training ($F_{2.016,\ 27.33}$= 4.687, p=0.0176), and was significantly different between axis components ($F_{1,\ 18}$= 11.66, p=0.0031) (**Fig. 15.C**). When analyzing trajectory variability within each session either through the Frechet distance or mean Euclidean distance, increasing trends were also observed throughout training, but these were not statistically significant (Frechet: $F_{1.815,\ 24.60}$= 3.305, p=0.0577; Euclidean: $F_{1.706,23.13}$=3.371, p=0.0586) (**Fig. 15.D-E**). No significant difference was found between the axial components of either measurement (Frechet: $F_{1,\ 18}$= 0.3663, p=0.5526; Euclidean: $F_{1,}$ 18=1.466, p=0.2416).

Given that animals did not significantly decrease the percentage of isolated lever presses upon full lever retraction (**Fig. 14.A**), we hypothesized that isolated (single) presses could be a source of press variability. To analyze whether there was a difference between variability within presses in sequences versus isolated presses, we analyzed a similar number of sequence presses vs isolated presses. For this, a smaller number of presses of the most abundant type of presses within a session was randomly selected to match the number of presses of the least abundant type (see **Section 3.6.2** for details). Indeed, when analyzing the same number of random sequence presses vs all isolated presses (or random isolated presses vs all sequence presses), we found that isolated presses have higher variability than sequence presses within each group in both X axis ($F_{1,\ 18}$=54.57, p<0.001) (**Fig. 16.A**) and Y axis components ($F_{1,\ 18}$=51.94, p<0.001) (**Fig. 16.B**). In addition, with this analysis we observed that neither single presses nor sequence presses decreased variability with time (X Axis: $F_{3.013,\ 36.38}$= 0.8218, p=0.4907; Y axis: $F_{2.860,\ 34.96}$=0.9498, p=0.4238).

Our results show that lever press velocity increases throughout training while trajectory variability does not change significantly, or at most, has a modest increase. Part of this variability could be due to the animals pressing isolated lever presses, which we found to have higher variability throughout sessions than presses in sequences. Interestingly, even though a decrease in trajectory variability was not found when looking at the mean of all mice throughout sessions, some animals were able to decrease press variability with training. Furthermore, each mouse developed a set of unique movement kinematics.

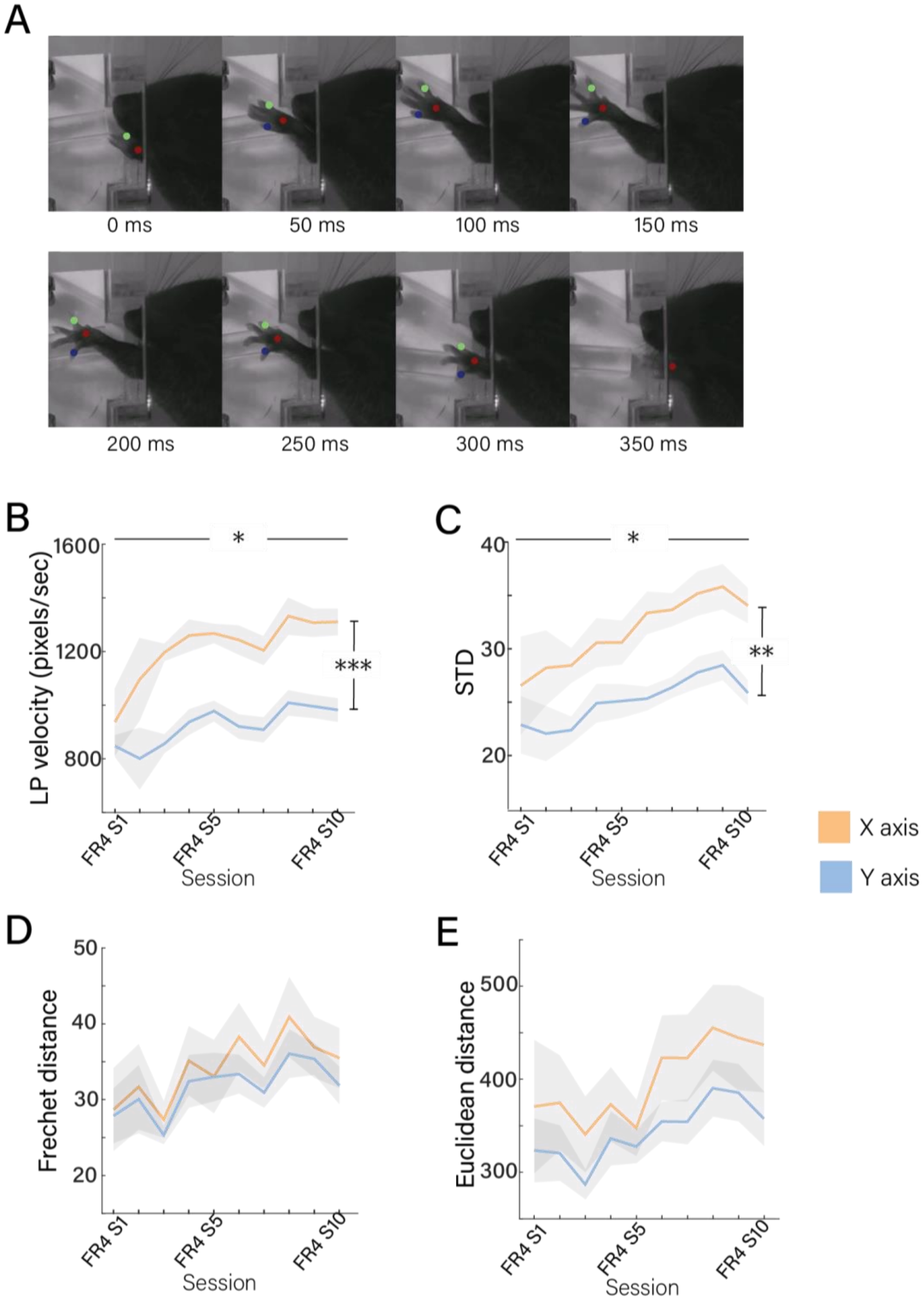

Figure 15 – Paw trajectory analysis during task learning. Paw trajectory analysis during task learning. **(A)** Representative frames collected during one lever press, with paw labelling achieved using an automated deep-learning tool; only the hand centroid (red) was used for further analysis. **(B)** Lever press (LP) velocity throughout FR4 training. **(C)** Standard deviation (STD) of paw trajectories throughout training. **(D)** Discrete Frechet distance between paw trajectories across sessions. **(E)** Mean sum of Euclidean distances of paw trajectories across sections. In **(B-E),** results are presented as mean ± SEM. Statistical significance of the differences between sessions for each parameter were analyzed by performing a Mixed-effects test (*** $p \leq 0.001$; ** $p \leq 0.01$; * $p \leq 0.05$); differences were nonsignificant if not reported. The number of videos (i.e., mice) analyzed within each session were, from S1 to S10, n=6, 7, 6, 8, 6, 9, 9, 10, 9, 10. *FR4 – fixed ratio 4; S1-S10 – session 1 to 10.*

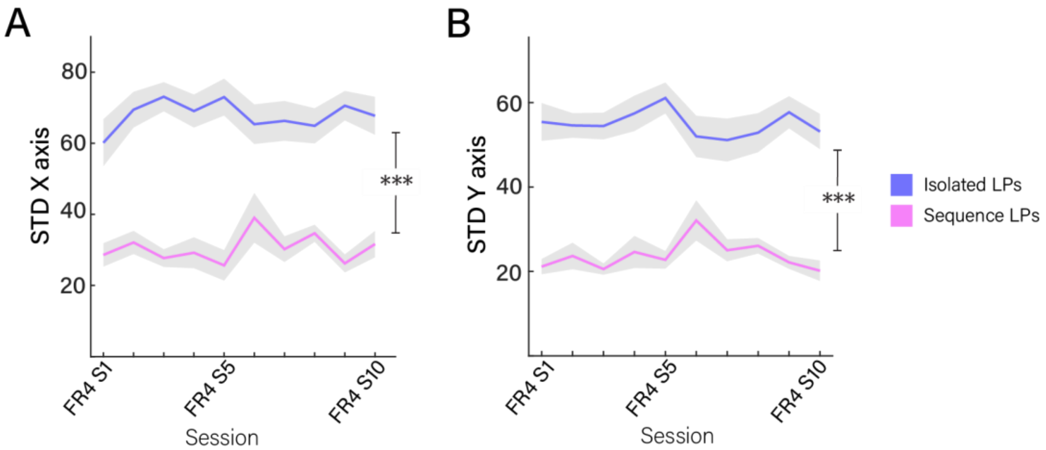

Figure 16 – Isolated presses have higher variability than presses in sequences. (A, B) Standard deviation (STD) of isolated and sequence presses in the X- **(A)** and Y-axis **(B)** component across training sessions. Values correspond to the mean ± SEM of all videos analyzed within a session. Statistical significance of the differences between isolated vs sequence presses was determined using Mixed-effects test (*** $p \leq 0.001$; session differences were non-significant). The number of videos (i.e., mice) analyzed within each session were, from S1 to S9, n=6,7,6,8,6,9,9,10,9 and 10. *FR4 – fixed ratio 4; S1-S10 – session 1 to 10.*

One example of a mouse that had high performance in this task is mouse 03. This mouse consistently decreased session duration, while increasing very early the number of lever presses per session and the number of presses in a sequence. Additionally, mouse 03 performed mainly multi-press sequences, with almost no isolated presses (**Fig. 17.A** – green). Throughout training, this mouse was able to decrease trajectory variability, as observed by the spatial clustering of total trajectories (**Fig. 17.B**). This was confirmed by analyzing the mean trajectory STD, which decreased with training (**Fig. 17.C**). Interestingly, mouse 04 had similar task performance results to mouse 03 in terms of session duration, total number of lever presses, presses per sequence, and percentage of non-isolated LPs (**Fig. 17.A** – blue). However, this mouse increased the mean trajectory STD throughout training (**Fig. 17.E**). Looking at the total trajectories plotted, one can observe that this mouse also seems to decrease variability to some extent, but seems to perform at least two types of lever presses, which are spatially distinct (**Fig. 17.D**).

Some animals, such as mouse 12, had a slower adaptation to the full lever retraction. This mouse could only achieve a notable number of presses (>50) by session 7, and only began to finish before time (i.e., obtain all rewards) in session 9. Additionally, it performed mostly isolated presses, showing a median value of one lever press per sequence (**Fig. 17.A** – purple). Its total lever press trajectory plots revealed that presses were still highly unorganized (**Fig. 17.F**), and trajectory variability decreased in the first sessions (particularly for the X axis component) but increased back in later sessions. (**Fig. 17.G**). These results suggest that this mouse was still in an initial phase of learning and would still need more sessions to plateau performance and movement kinematics.

In sum, our data shows that mice developed individual press strategies, which are refined through training. Indeed, while the mean session trajectory variability did not decrease, we show that some mice were able to significantly decrease trajectory variability with training. Our data suggest that some mice were still in the early phases of training, while others seem to develop more than one strategy when pressing the lever.

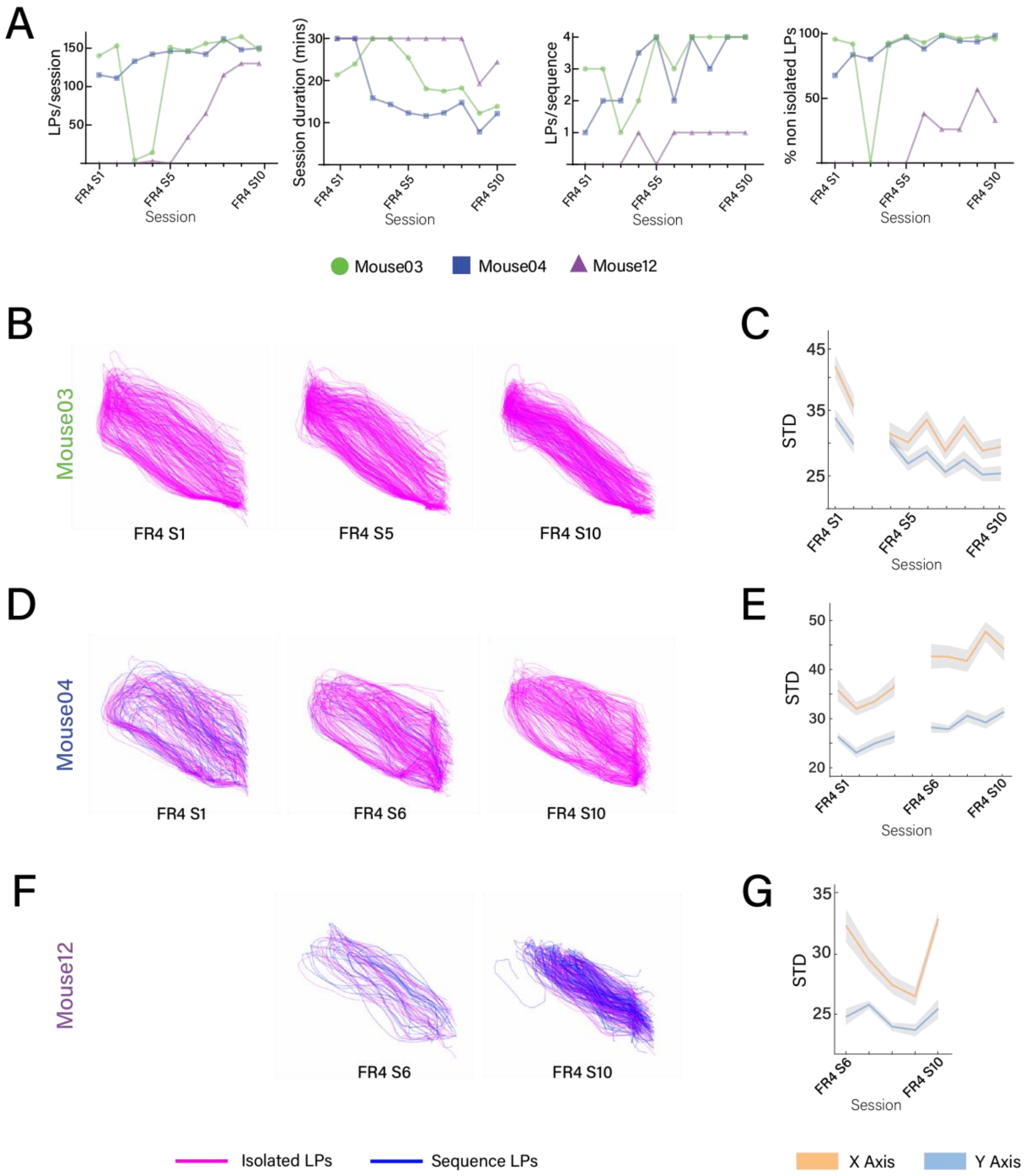

Figure 17 – Examples of individual mouse trajectory kinematics. **(A)** Total number of lever presses (LPs), session duration, number of LPs per sequence and percentage of non-isolated presses for mouse 3, 4 and 12. **(B)** Total individual lever press trajectories of the first, middle and last session upon full lever retraction, of mouse 03. **(C)** Mean standard deviation (STD) of trajectories per session of mouse 03. **(D)** Total individual lever press trajectories of the first, sixth and last session upon full lever retraction, of mouse 04. **(E)** Mean standard deviation (STD) of trajectories per session of mouse 04. **(F)** Total individual lever press trajectories of the sixth and last session upon full lever retraction, of mouse 12. **(G)** Mean standard deviation (STD) of trajectories per session of mouse 12. In **(B, D, F),** pink represents lever presses performed in sequences, while blue depicts isolated presses. For the STD graph, orange represents the STD value relative to the X axis, while pale blue depicts the value for the Y axis. Trajectories mean standard deviation values **(C, E, G)** are mean ± SEM.

4.2. Immediate early gene expression upon motor learning

4.2.1. Establishing a candidate immediate early gene as a marker of striatal neuronal activity

Immediate early genes are proteins used as markers of recent neuronal activity and/or plasticity. In the context of our work, identifying cells involved during task learning and performance allows us to study structural plasticity in task vs non-task related MSNs.

First, we sought to determine a marker that, under our experimental conditions, would achieve expression upon dopamine receptor stimulation, similarly to what we hypothesized would happen in the context of motor learning. In order to do this, we used apomorphine, a mixed D1/D2 agonist known to lead to robust increases in immediate early gene expression in the striatum[115,128]. It reaches the brain through systemic intraperitoneal injection (<30mins), and protein levels are already detectable at 1h post injection[115,116].

Different groups of mice (same mice used for the sparse labelling experiments, described in **Sections 3.2 and 3.3**) were subjected to either apomorphine or vehicle injections. Minutes after injection, apomorphine-injected animals started moving slower and their eyes became half-closed. Some mice also displayed a cage climbing behavior. These effects of apomorphine injections were previously described in mice[116]. On the other hand, vehicle-injected mice displayed normal behavior. To make sure that there was a robust induction of immediate early gene expression, we chose a 2h post-injection time point to sacrifice and perfuse mice[115,116]. The expression of two immediate early genes, Arc and c-Fos, were studied by immunofluorescence in brain slices of these animals. Different protocols and antibodies were tested to achieve good signal-to-noise ratio for Arc and c-Fos detection.

First, we co-stained slices for c-Fos and Arc. We observed that c-Fos expression was overall higher in animals injected with apomorphine, while Arc expression did not show an obvious difference between apomorphine- and vehicle-treated mice (**Fig. 18.A**). As expected, given the selective modulation of dopamine receptors by apomorphine, this difference in c-Fos expression was quite evident in the striatal region (**Fig. 18.C**), as well as in cortical (**Fig. 18.B**) and septal (**Fig. 18.A**) regions. Arc expression also seems to be increased in the striatum (**Fig. 18.C**) and cortex (**Fig. 18.B**) of apomorphine-treated mice, but this observation is less striking when compared with c-Fos. Further, we observed that far more cells within the same conditions were stained for Arc, in comparison to c-Fos. Some colocalization between the Arc and c-Fos signals was observed, particularly in cortical regions (**Fig 18.B**). Given the differences in signal localization of each protein, a different imaging approach (acquire image stacks, in a line-by-line approach) would be needed to further study co-localization of the two signals.

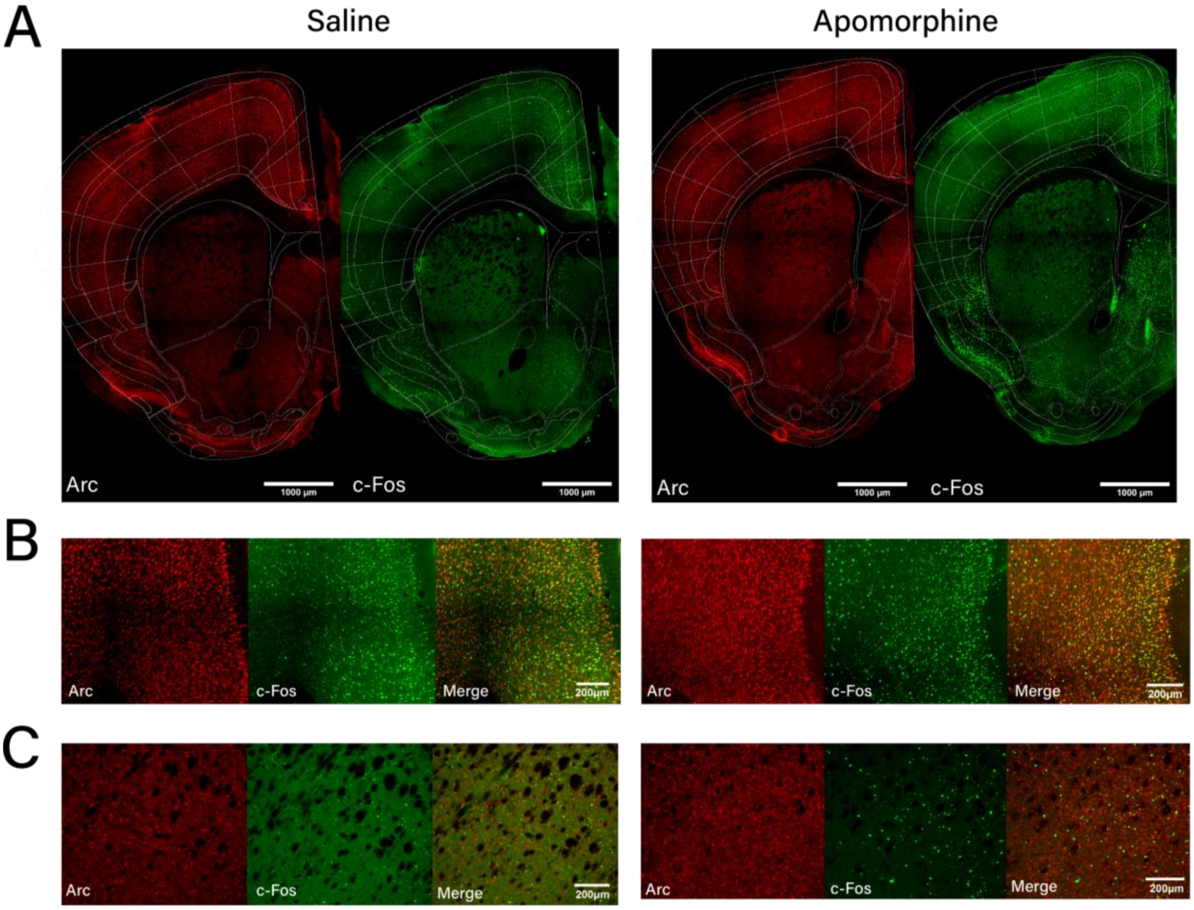

Figure 18 – Arc and c-Fos immediate early gene expression, in saline- and apomorphine-treated animals. For each condition, the staining for Arc and c-Fos using the two antibodies – mouse anti-Arc monoclonal from Santa Cruz and rabbit anti-c-Fos monoclonal from Cell Signalling - was simultaneously performed on the same slice. **(A)** Representative single plane brain slice overviews (10x objective) of Arc and c-Fos immunofluorescence, aligned to the reference atlas. **(B),(C)** Higher magnification images of cortical (anterior cingulate cortex region)**(B)** and striatal regions **(C),** depicting Arc, c-Fos and the merge of the two signals.

Still, the lack of signal differences in slices stained for Arc in apomorphine versus vehicle treated mice lead us to try a different antibody for Arc staining. Further, we were interested in determining whether a different antibody would also stain a similar number of cells. Under our experimental conditions, neither of the antibodies tested – one polyclonal and one monoclonal – seemed to show apomorphine specific increases in Arc expression (**Fig. 19.A**).

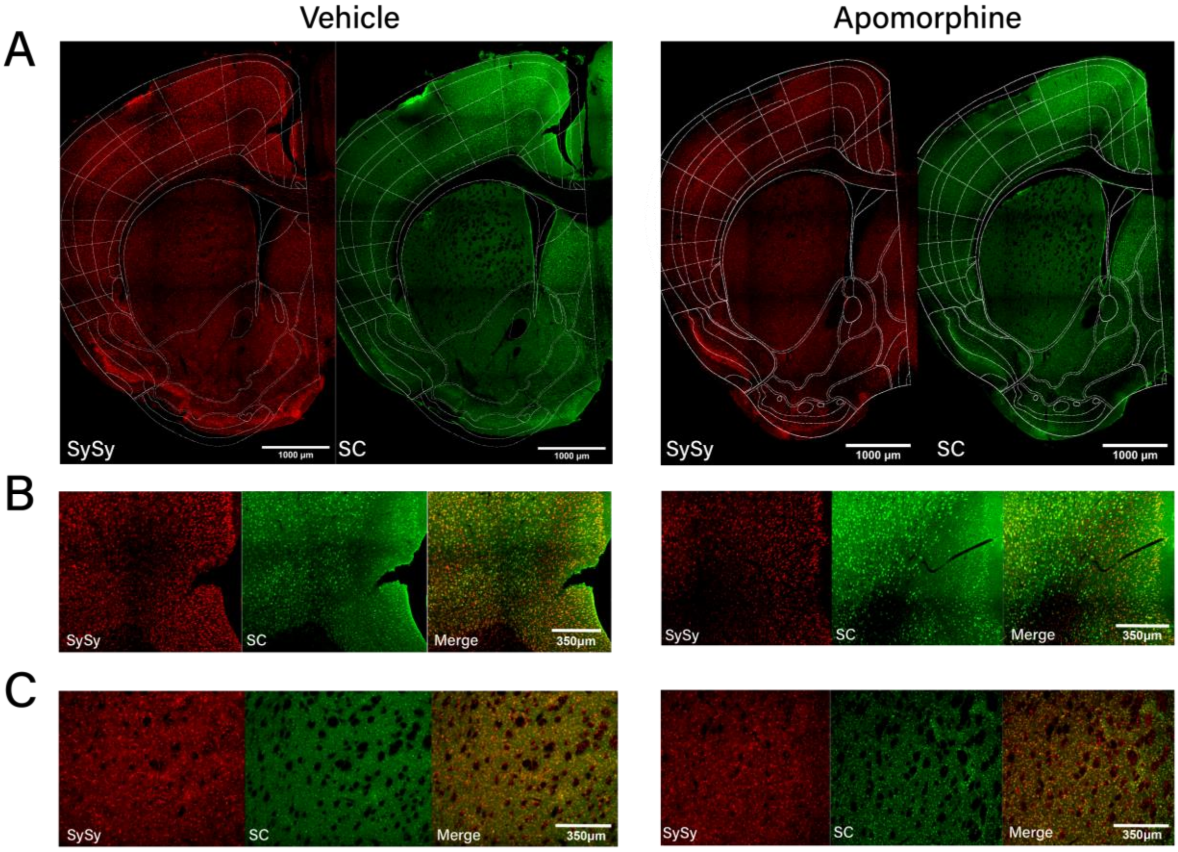

Figure 19 – Comparison of Arc immunofluorescence detection by two different antibodies, in saline- and apomorphine-treated animals. For each condition, the staining for Arc using the two antibodies -Synaptic Systems' (SySy) anti-Arc rabbit polyclonal pre-conjugated with AF647 and Santa Cruz's (SC) anti-Arc mouse monoclonal- was simultaneously performed on the same slice. **(A)** Representative single plane brain slice overviews (10x objective) of Arc immunofluorescence, aligned to the reference atlas. **(B)**,**(C)** Higher magnification images of cortical (anterior cingulate cortex region) **(B)** and striatal regions **(C)**, depicting the signal obtained with each antibody and the merge. *SySy – Synaptic Systems; SC – Santa Cruz.*

Due to the high numbers of cells expressing Arc in basal conditions and the apparent lack of an obvious effect of apomorphine in Arc expression, we decided to focus on c-Fos as a plasticity marker. We tested two antibodies against c-fos and observed that there were considerable differences in the number of cells stained by these two antibodies in consecutive slices of the same apomorphine-treated mice. The rabbit polyclonal antibody from Synaptic Systems (**Fig. 20.A**) labelled more cells than the rabbit monoclonal antibody from Cell Signaling (**Fig. 20.B**). This difference was particularly remarkable in the striatal region but was also observed in other regions. Additionally, this difference was consistently observed in vehicle-injected mice (not shown), while an increase in c-Fos signal was seen in the apomorphine condition using any of the two antibodies. We were also able to achieve a higher signal-to-noise ratio with the monoclonal antibody and clear labelling of cells at higher resolutions, with little background staining in the striatum of vehicle-treated animals (**Fig. 20.C**).

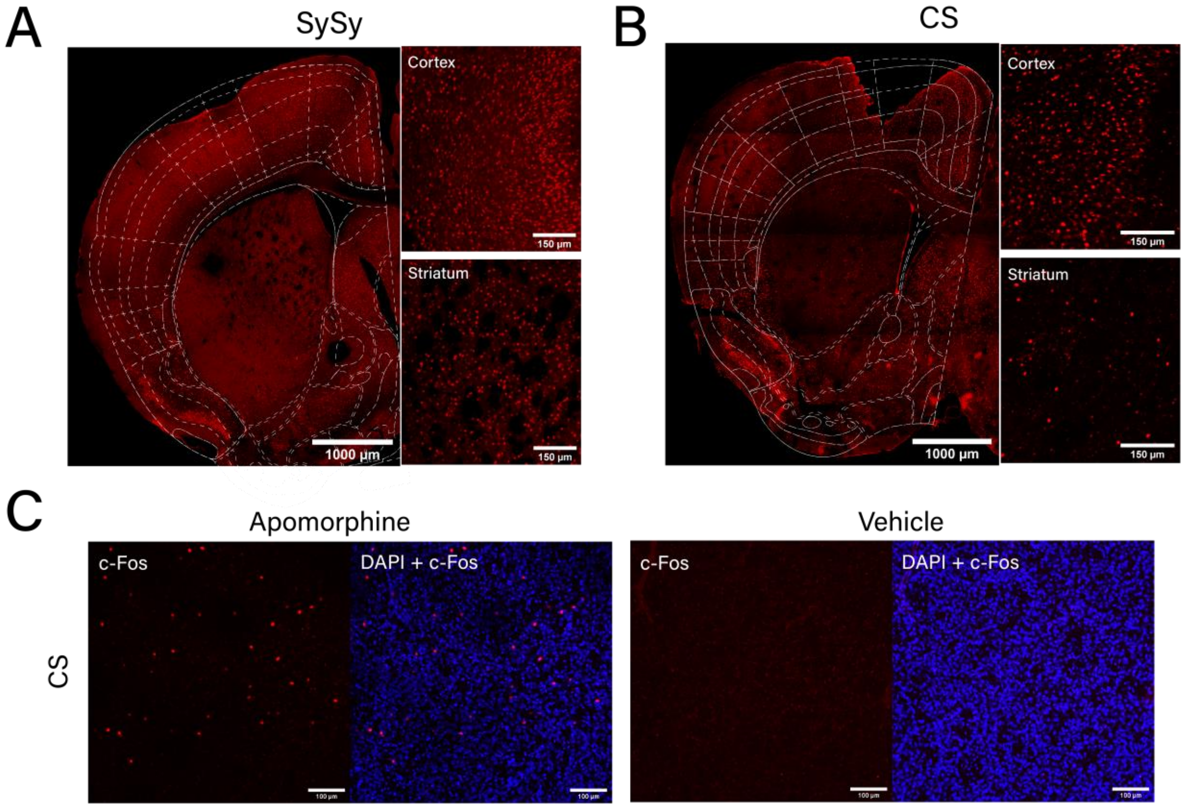

Figure 20 – Comparison of c-Fos immunofluorescence detection by two different antibodies. Detection of c-Fos in consecutive brain slices of the same mice were performed with a rabbit polyclonal anti-c-Fos antibody from Synaptic Systems and a rabbit monoclonal anti-c-Fos antibody from Cell Signaling. **(A-B)** Representative single plane brain slice overviews (10x objective) of c-Fos immunofluorescence detected by the polyclonal **(A)** and monoclonal **(B)** antibodies in apomorphine-treated animals; right insets depict higher magnifications of the respective brain slice in cortical (anterior cingulate cortex; top) and striatal areas, as indicated. **(C)** Representative maximum intensity projections of image z-stacks (20x objective) depicting c-Fos expression in the striatum of apomorphine- and vehicle-treated mice, as detected by the Cell Signaling monoclonal antibody. Merged imaged of c-Fos and DAPI are also shown. *SySy – Synaptic Systems; CS – Cell Signalling.*

Our results show that, under our experimental conditions, c-Fos is a better marker to evaluate recent neuronal activity than Arc, as increases in expression were observed in mice injected with a dopamine agonist, in comparison to vehicle-injected animals. Further, were able to optimize the staining protocol to achieve a good signal-to-noise ratio using a monoclonal antibody, which showed less stained cells than a polyclonal one.

4.2.2. c-Fos expression upon lateralized motor learning

One of the goals of this project was to characterize c-Fos expression upon learning of a lateralized motor task. In addition to the task-trained animals, a cohort of animals treated with apomorphine or vehicle, where used as positive and negative controls for c-Fos expression, respectively. Vehicle-injected mice were used as negative controls for the expression of c-Fos given that they should have only basal levels of expression of the protein. On the other hand, animals injected with apomorphine were used as positive controls for c-Fos expression, as apomorphine induces robust c-Fos expression[115]. Control mice were handled and habituated to intraperitoneal (IP) injections during 10 days before being treated with either an apomorphine or vehicle injection, as described in **Fig. 21**.

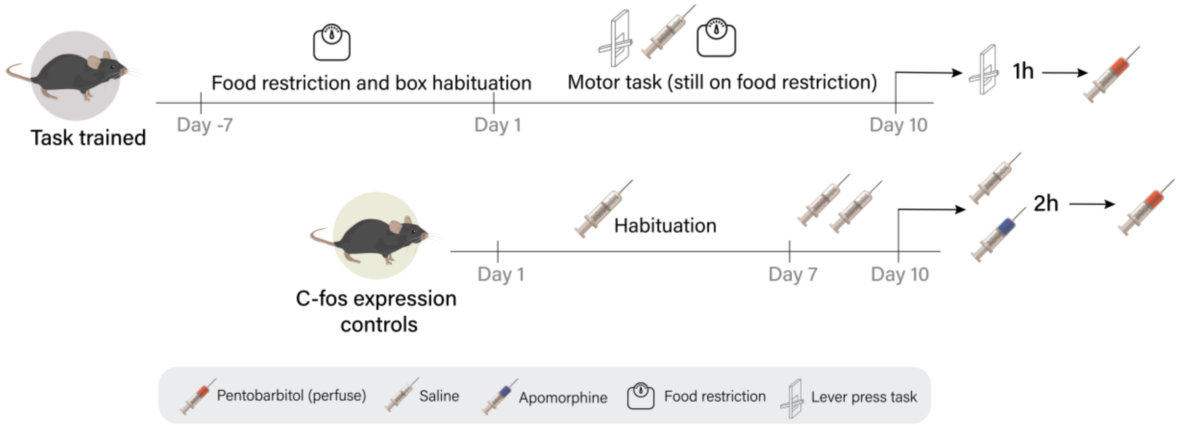

Figure 21 – Schedule overview of task trained and c-Fos expression controls. Task-trained mice were subject to 7 days of food restriction and habituation to the behavior boxes, prior to start of training. During training, mice were additionally treated with an IP saline injection, after the first daily training session, to habituate them to the final day lethal pentobarbital injection. c-Fos expression positive and negative control animals were subject to 10 days of handling and to a similar IP injection habituation. From the seventh day onwards, these controls received 2 injections to habituate them to the additional pharmacological treatment injection of the last day. Finally, on day 10, half of the control animals received an apomorphine injection (positive controls), while the other half received a vehicle injection (negative controls). Both task-trained and control mice received a terminal pentobarbital injection, 1h after the end of the last training session and 2h after the apomorphine/saline injection, respectively.

As observed in previous experiments, vehicle injected mice have visibly less expression than apomorphine injected ones (**Fig. 22**). Interestingly, this difference in expression was observable either at the number of stained cells (such as in the striatum), or at the intensity of expression, despite having a similar number of cells (such as in the cortex) (**Fig. 22.C-D**). For the brains of task-trained mice, we analyzed animals that performed the task with different levels of learning in different parameters. Additionally, we stained the brains of two task 'outliers' – one animal that did not learn the task, and one that learned the task with the opposite paw to that expected (i.e., it was trained on a box with the lever on the left corner but somehow learned to perform the task with its right paw). The brains of task-trained animals showed variable levels of signal intensity and pattern, but overall had more similar patterns of expression to brains of vehicle-injected mice (**Fig. 23** vs **Fig.22**).

Given the lateralization of the task, we were interested in studying whether there were evident contralateral increases in c-Fos expression upon training. In some mice, as the one shown in **Fig. 23**, a moderate contralateral difference was evident in the medial region of the striatum (**Fig. 23.C**), but not the DMS (**Fig. 23.B**). In other anterior-posterior regions, other patterns of striatal c-Fos expression were observed. For instance, in some anterior slices an obvious increase in c-Fos expression was observed contralaterally in the DMS (not shown). No remarkable differences were clearly visible at the level of the cortex contralaterally (**Fig. 23.D**), given the high number of cells stained in this region. Likewise, it was hard to visually assess obvious contralateral differences in regions such as the piriform cortex (**Fig. 23.E)**. Thus, to correctly assess the number of cells expressed in each region and in each hemisphere, a quantitative analysis was needed.

c-Fos-positive cell detection and atlas mapping was performed using the BrainJ pipeline[123]. Upon analysis through the pipeline, we were able to achieve accurate detection of whole brain c-Fos expression, despite the different levels of signal and background intensity in different areas (**Fig. 24**). Having c-Fos-positive cells mapped to its atlas location, we were able to study the number of cells expressing c-Fos in all the regions represented in the slices stained (covering 4-5mm in the anterior-posterior axis; mean=85±4 slices) and compare the contralateral and ipsilateral hemispheres to the trained paw.

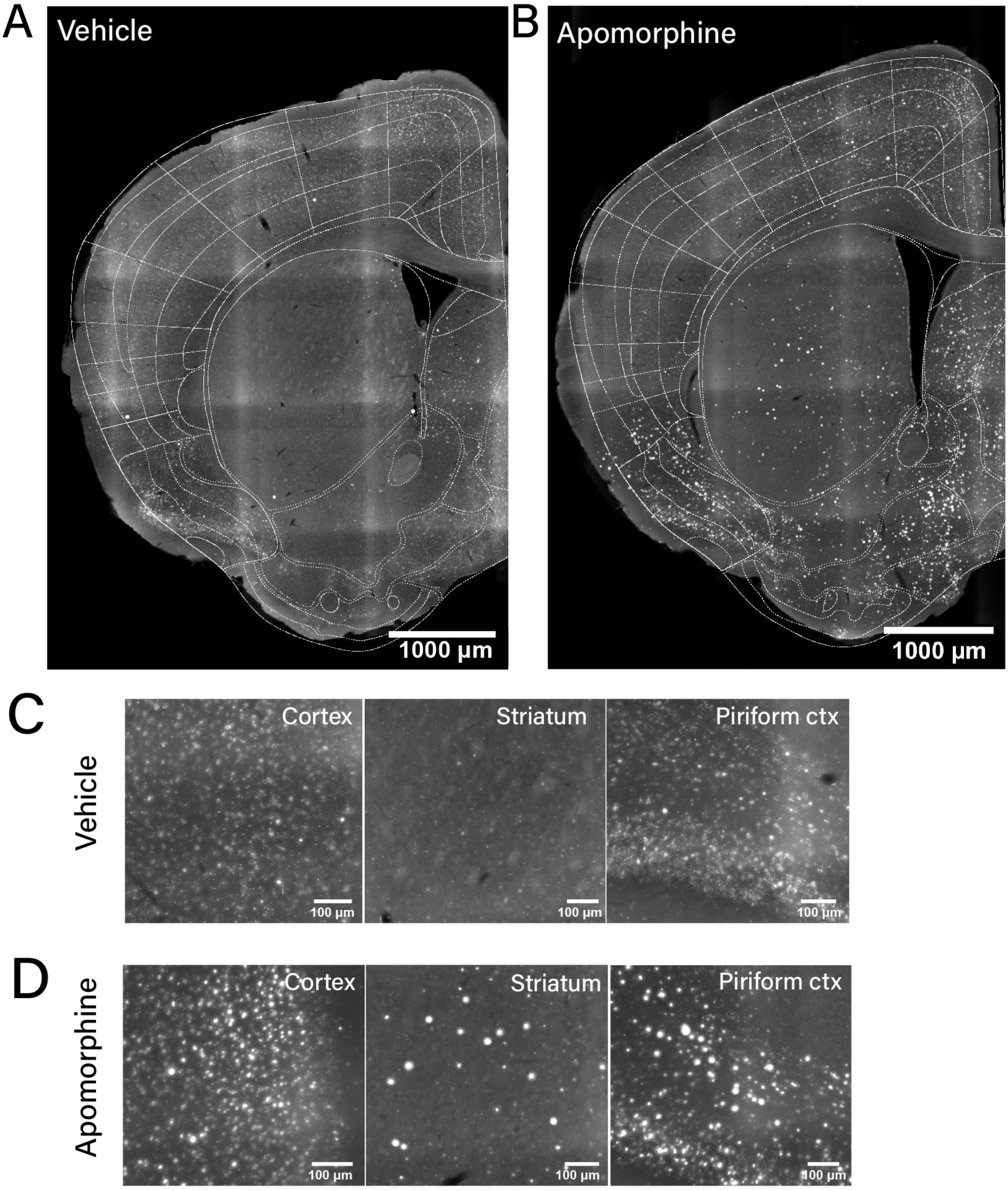

Figure 22 – c-Fos expression in apomorphine- and vehicle-injected mice. (A-B) Representative maximum intensity projections of brain slices reconstructed from image tiles (10x objective), depicting c-Fos expression in apomorphine- **(A)** and vehicle-injected **(B)** mice, aligned to the reference atlas. **(C-D)** High magnification images of cortical (anterior cingulate area region), striatal (medial region) and piriform cortex regions of the representative slices shown in **(A)** and **(B)**, respectively.

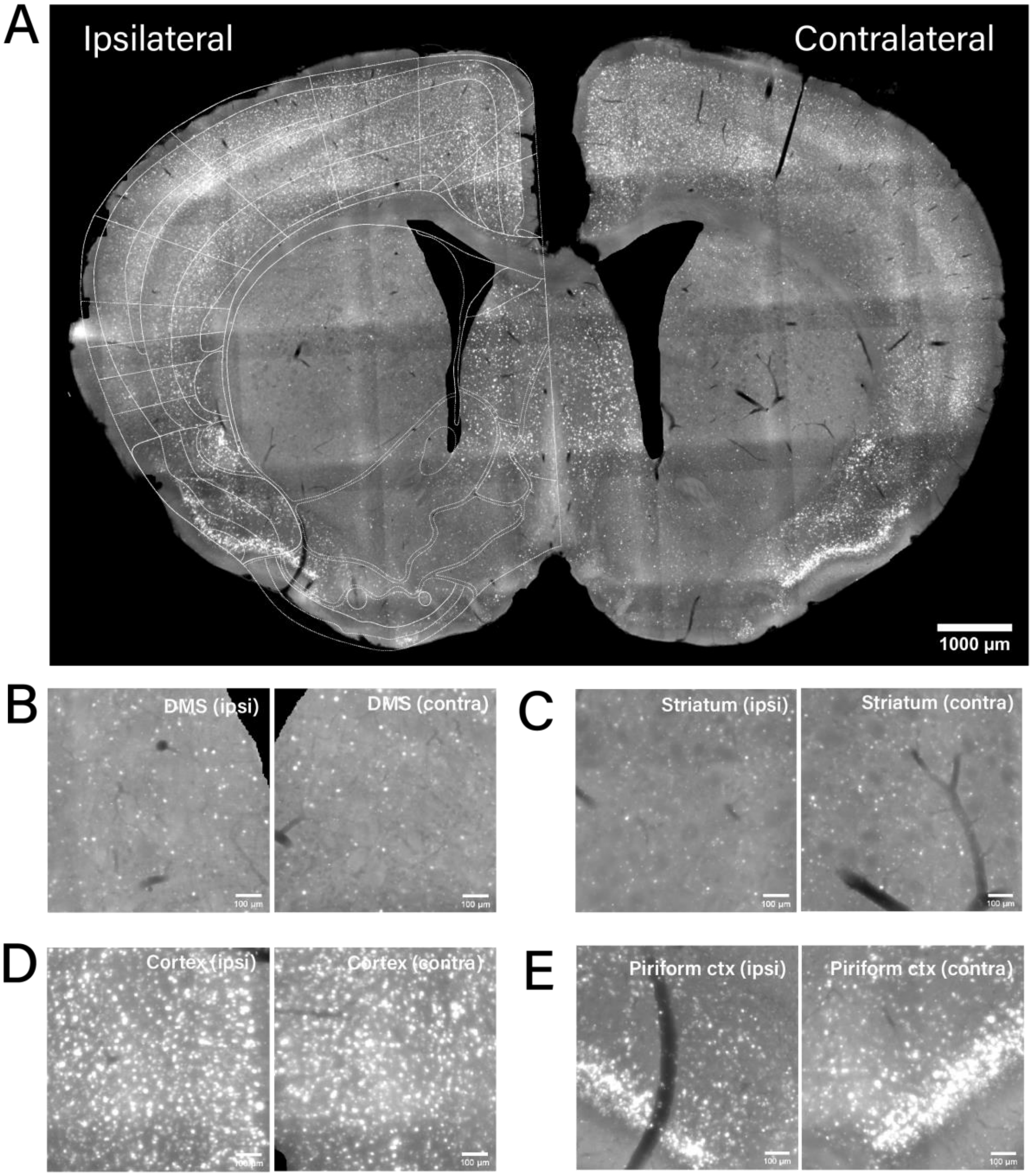

Figure 23 – c-Fos expression in a task trained animal. **(A)** Representative maximum intensity projection of one brain slice from one task-trained mouse, reconstructed from image tiles (10x objective) depicting c-Fos expression. **(B-E)** High magnification images of contralateral (‘contra’) and ipsilateral (‘ipsi’) of the medial striatum **(B),** dorsomedial striatum **(C),** cortical anterior cingulate region, and piriform cortex (E), of the slice shown in **(A).** *DMS – dorsomedial striatum.*

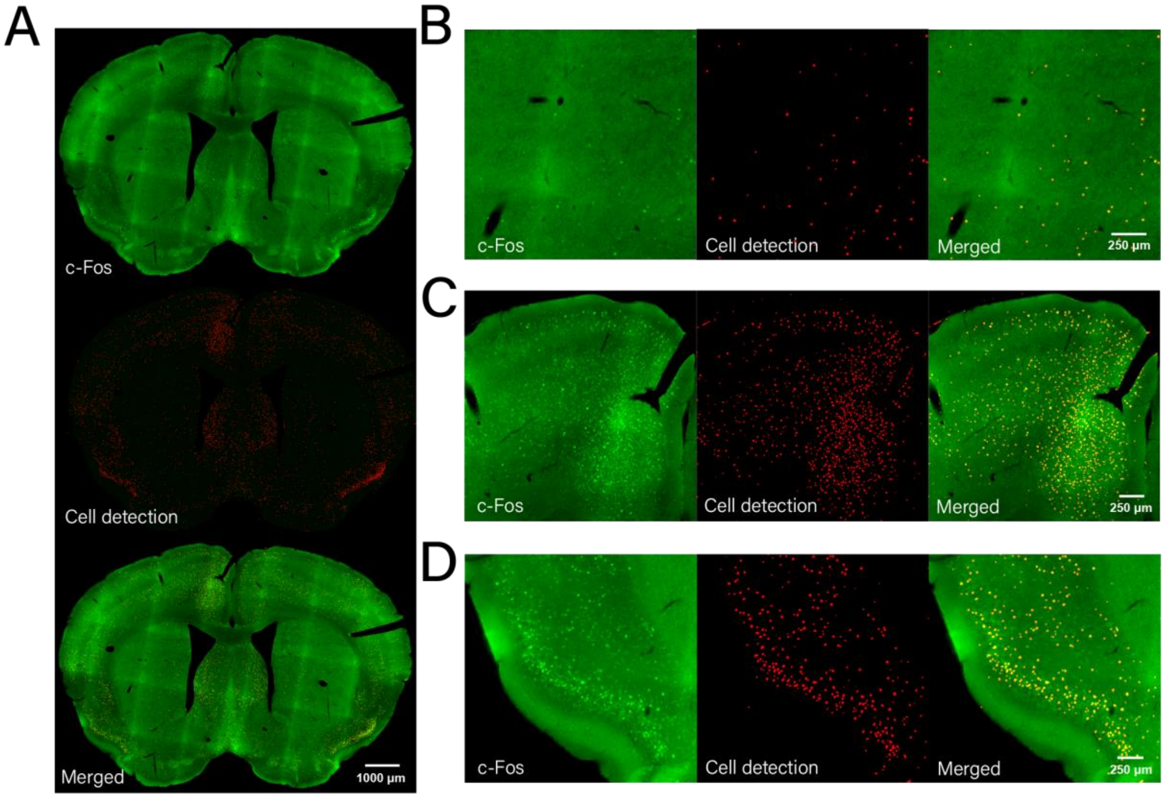

Figure 24 – Cell detection in the BrainJ pipeline, using Ilastik pixel classification. **(A)** Top panel: representative maximum intensity projection of a brain slice from a task-trained mouse reconstructed from image tiles (10x objective), depicting c-Fos expression; Middle panel: cell detection masks using BrainJ; Bottom panel: merged view. **(B-D)** High magnification images depicting c-Fos expression, respective cell detection masks, and merged views of striatal (medial region) **(B),** cortical (anterior cingulate area region) **(C),** and piriform cortex regions **(D)** of the same slice shown in **(A).**

As mentioned, due to the laterality imposed by the task, we hypothesized that there would be a specific increase in the number of cells expressing c-Fos in the contralateral hemisphere to the trained paw. Given that motor learning induces plasticity at corticostriatal synapses[2], we investigated whether there was an increased number of cells expressing c-Fos upon task training, in contralateral striatum and layer 5 of the motor cortex where a lot of the presynaptic partners of medium spiny neurons (MSNs) are located. First, we looked at the ratio between the number of cells in the contralateral vs ipsilateral hemisphere to the trained paw. We found that both the striatum (mean= +12.2%) and the layer 5 of the primary motor cortex (MOp5; mean=+11.1%) had increased percentage of cells expressing c-Fos in the contralateral hemisphere. We further investigated other motor-related regions of the cortex, namely the secondary motor cortex, and limb regions of the somatosensory cortex. We also found increases in the primary motor cortex (MOp; mean=+13.5%), upper limb region (SSpul; mean=+16.7%) and lower limb region (SSpll; mean=+8.9%) of the somatosensory cortex. Interestingly, the secondary motor cortex (MOs; mean=+3.8%) did not have a contralateral increase in the number of cells expressing c-Fos in all except for one animal (**Fig. 25.A**).

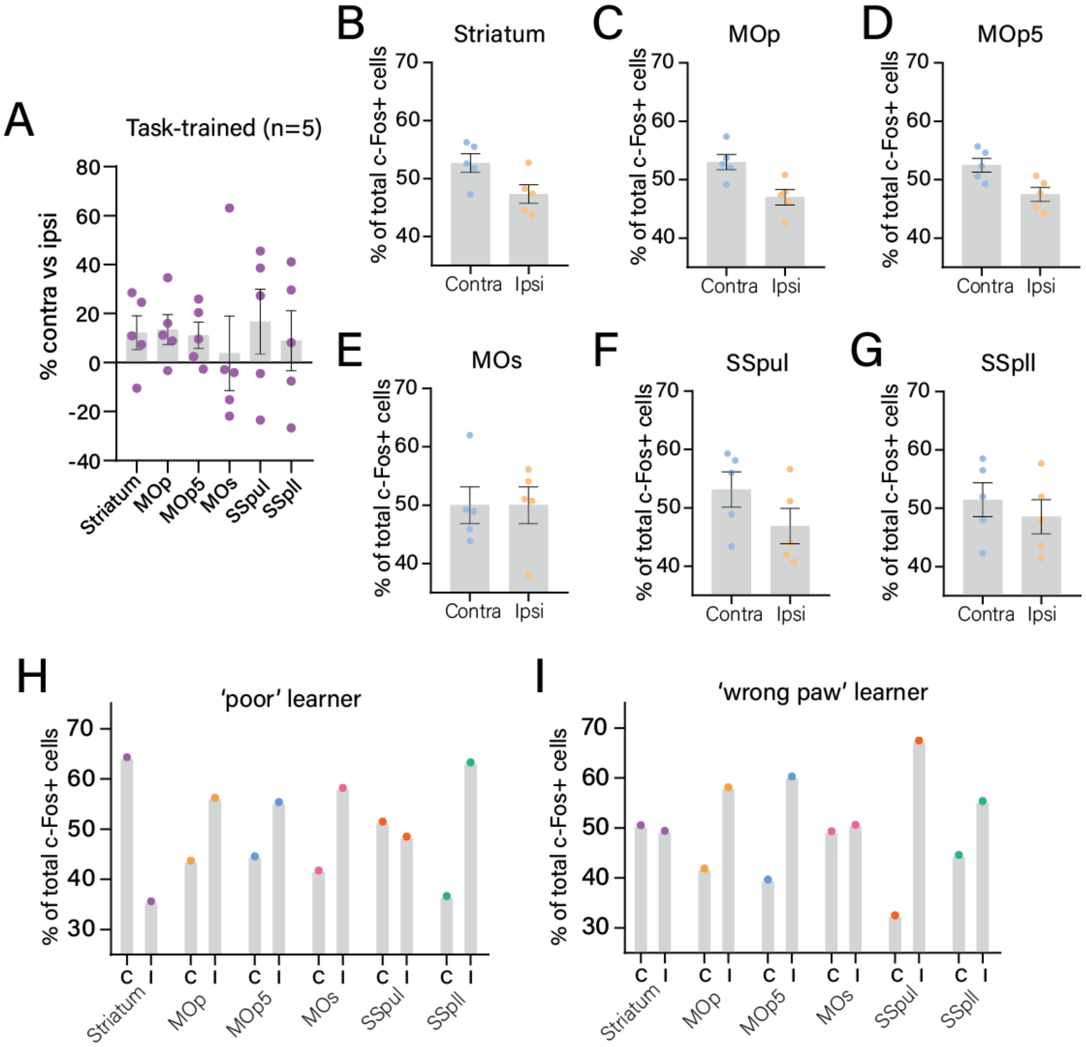

Figure 25 – Hemispherical difference of the number of cells expressing c-Fos detected in different brain regions of task-trained mice. (A) Percentage of contralateral difference in expression of c-Fos in task trained mice, for each of the regions in study. **(B-G)** Percentage of total cells expressing c-Fos in each hemisphere of task-trained mice in the striatum **(B),** primary motor cortex **(C),** primary motor cortex layer 5 **(D),** secondary motor cortex **(E),** primary somatosensory cortex upper limb region **(F),** primary somatosensory cortex lower limb region **(G). (H-I)** Percentage of total cells expressing c-Fos in each hemisphere of task-trained 'outliers' in each of the regions in study. Values are presented as mean ±SEM. Differences between the number of c-Fos positive cells in each hemisphere **(B-G)** were analyzed by performing a paired t-test, and all were found to be non-significant (ns). *MOs/p – primary/secondary motor cortex; SSpll/ul – primary somatosensory cortex lower/upper limb.*

We then calculated the percentage, for each animal, of c-Fos-positive cells detected in each hemisphere relative to the total number of c-Fos-positive cells. Task-trained mice showed a trend to higher percentages of c-Fos positive cells in the contralateral striatum (**Fig. 25.B**), primary motor cortex (**Fig. 25.C**) and primary motor cortex layer 5 (**Fig. 25.D**). The contralateral upper limb area of the primary somatosensory cortex also seemed to have an increased number of cells expressing c-Fos (**Fig. 25.F**), as well as the lower limb area (**Fig. 25.G**). However, upon statistical analysis neither of these values was found to be statistically significant. Interestingly, the secondary motor cortex did not have a contralateral difference in the number of cells expressing c-Fos (**Fig. 25.D**).

We analyzed separately the animals that did not achieve normal learning of the task, which we termed task-trained ‘outliers’. A difference in c-Fos expression between hemispheres was still hypothesized in the mouse that learned the task with the opposite paw to that expected, which we will subsequently refer to as ’wrong paw learner’. Surprisingly, we found almost no discernable difference in c-Fos-positive cells between the striata of the two hemispheres. Moreover, there were considerably more c-Fos expressing cells in the ipsilateral hemisphere to the lever-pressing paw in all other areas (**Fig. 25.I**). The mouse that did not learn the task, which we will term ‘bad learner’, only pressed the lever during CRF sessions and stopped pressing completely upon full lever retraction. Paradoxically, this animal revealed a high contralateral increase in the number of cells expressing c-Fos in the striatum, but not in other regions such as layer 5 of the primary motor cortex (**Fig. 25.H**).

In controls, we show inter-hemispherical differences in c-Fos expression as both the percentage in hemisphere relative to the total, as well as a ratio between the left vs right hemisphere. The 2 vehicle-injected mice showed increases in the number of cells expressing c-Fos specifically in the left hemisphere in most areas (**Fig. 26.A-B**). For the ratio between left vs right hemisphere, the striatum had both the lowest value and the lowest variability of the regions analyzed (mean=16.94±2.01%), while the upper limb region of the somatosensory cortex had both the highest value and highest variability (mean=48.72±55.04%) (**Fig. 26.B**). The apomorphine-injected animal showed less inter-hemisphere differences, and differences were not for the same hemisphere in all areas, as in vehicle-injected animals (**Fig. 26.C-D**). The highest difference between hemispheres was observed for the upper limb region of the somatosensory cortex, and the lowest for the lower limb region (**Fig. 26.D**). Nevertheless, a larger number of animals would be needed to study in extent what are the normal inter-hemispherical differences in both negative and positive controls.

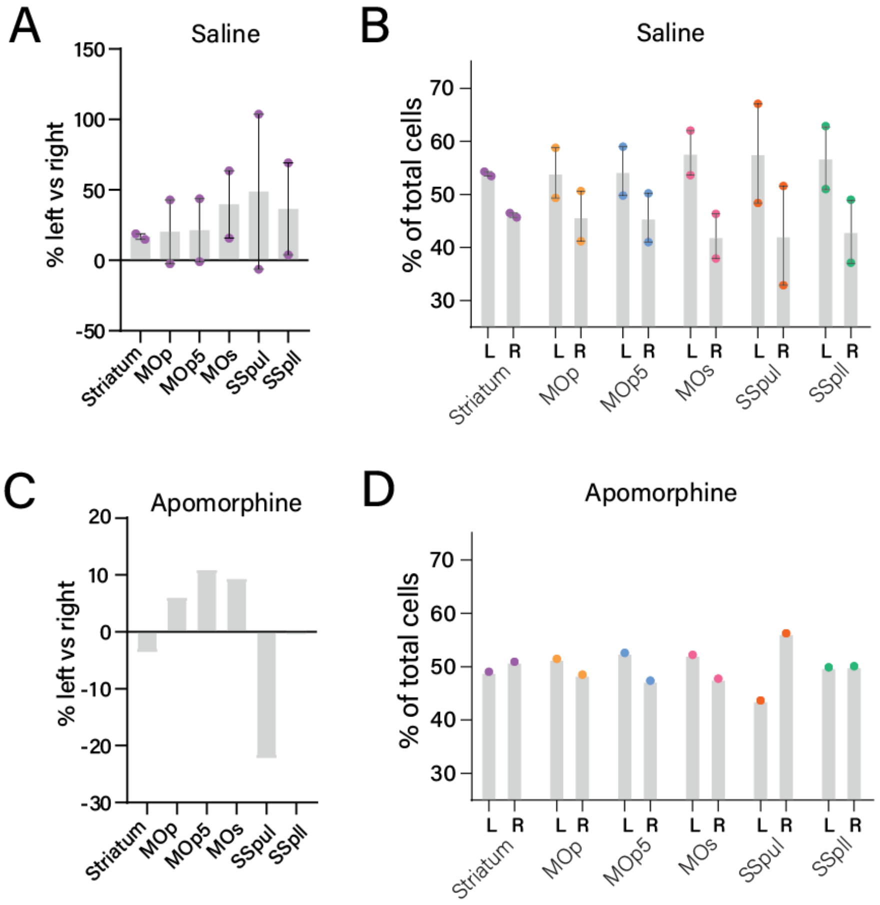

Figure 26 – Hemispherical difference of the number of cells expressing c-Fos detected in different brain regions of saline and apomorphine injected mice. (A, C) Percentage of total cells expressing c-Fos in each hemisphere of saline and apomorphine injected mice in each of the regions in study. **(B, D)** Percentage of difference in the number of cells expressing c-Fos in the left versus right hemisphere. Note that the low n precludes any statistical comparisons. Values are presented as mean ±SEM*. MOs/p – primary/secondary motor cortex; SSpll/ul – primary somatosensory cortex lower/upper limb.*

At last, we looked at the number of total cells expressed in different brain regions. In addition to the striatum and motor-related cortices, we were interested in other sensory related regions such as supplemental somatosensory cortex. While the number of control animals is small, hampering statistical comparisons between conditions, we found that task training did not seem to increase the number of cells expressing c-Fos in the striatum, when compared to negative controls. As expected, the brain of the apomorphine-injected mouse seemed to have a higher number of c-Fos positive cells in the striatum when compared with the other groups (**Fig. 27.B**). Both the primary (MOp) and secondary (MOs) motor cortices, and in particular layer 5 of the primary motor cortex (MOp5), appeared to show a trend for increased levels of c-Fos-positive cells when compared with the negative controls (**Fig. 27.C-E**). In addition, areas from the primary somatosensory cortex, such as the upper limb (SSpul) (**Fig. 27.F**), lower limb (SSpll) (**Fig. 27.G**), and barrel field (SSpbfd) (**Fig. 27.H**) areas, as well as the supplemental somatosensory cortex (SSs) (**Fig. 27.I),** also showed an increasing trend in the number of cells expressing c-Fos.

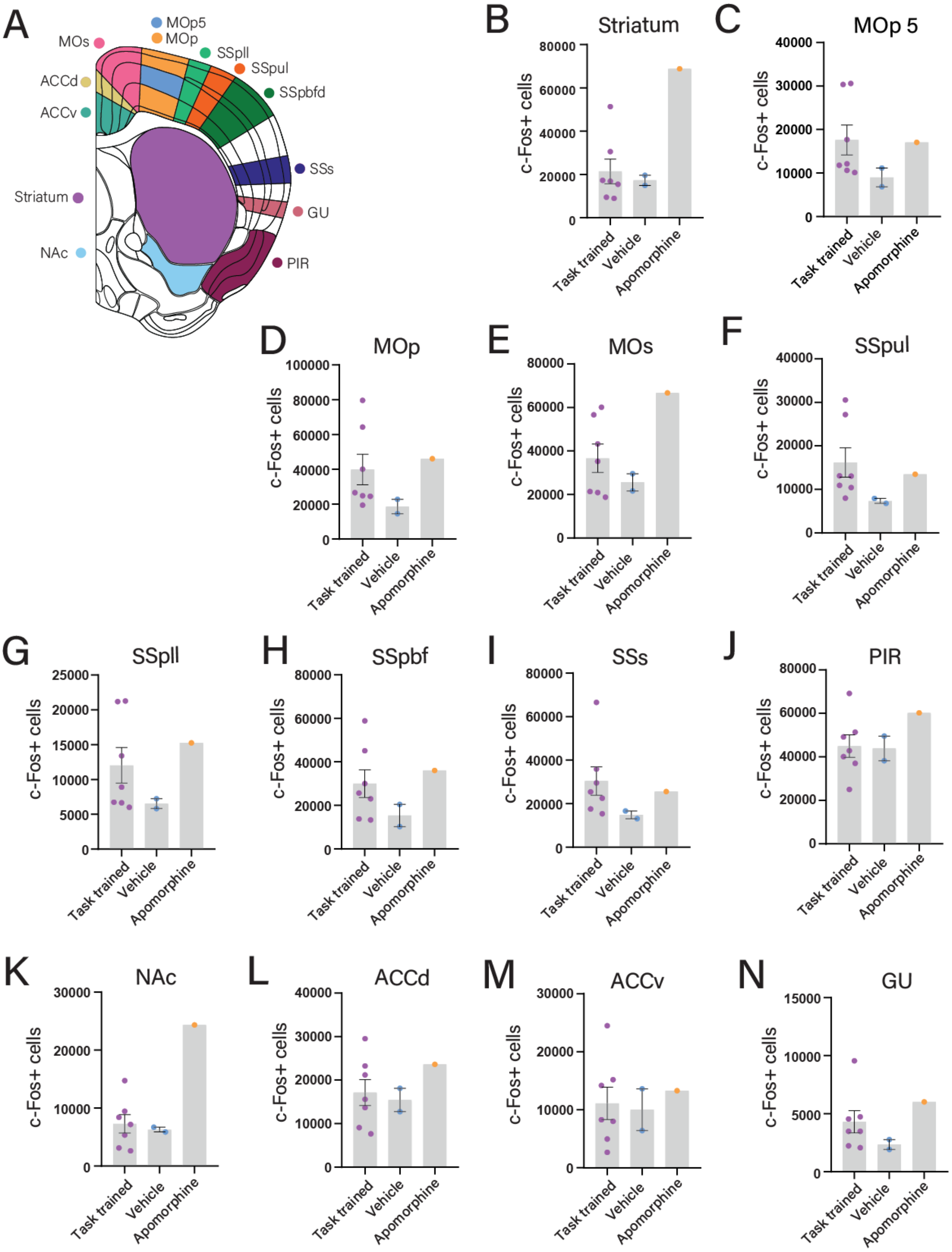

Figure 27 – Cell counting of the total number of cells expressing c-Fos in different brain regions of task-trained (n=7) and saline- (n=2) and apomorphine-injected (n=1) mice. (A) Diagram of coronal slice with different regions of interest shown in color. **(B-N)** Total number of cells detected per brain (sum of c-Fos-positive cells in the two hemispheres) in each condition, in the striatum **(B)**, primary motor cortex layer 5 **(C)**, primary motor cortex **(D)**, secondary motor cortex **(D)**, gustatory areas **(E)**, primary somatosensory cortex upper limb region **(F)**, primary somatosensory cortex lower limb region **(G)**, primary somatosensory cortex barrel cortex **(H)**, supplementary somatosensory cortex **(I)**, piriform cortex **(J)**, nucleus accumbens **(K)**, dorsal anterior cingulate cortex **(L)**, ventral anterior cingulate cortex **(M)**, and

gustatory areas **(N).** Note that the low n of vehicle and apomorphine conditions preclude any statistical comparisons. *ACCv/d – ventral/dorsal anterior cingulate cortex; MOs/p – primary/secondary motor cortex; SSpll/ul – primary somatosensory cortex lower/upper limb; SSpbfd – primary somatosensory cortex barrel field; SSs – supplemental somatosensory cortex; GU – gustatory areas; PIR – piriform cortex; NAc – nucleus accumbens.*

We also sought to look at other non-motor related areas. As expected, the nucleus accumbens (NAc), a ventral part of the striatum, also seemed to have increased number of cells expressing c-Fos in the apomorphine control (**Fig. 27.K**). Interestingly, we observed that the piriform cortex (PIR) and anterior cingulate cortex areas (dorsal and ventral; ACAd, ACAv), areas with numerous and intense c-Fos puncta in all groups (**Figs. 22 & 23**), did not seem to have differences in the number of cells expressing c-Fos between conditions. Thus, differences in c-Fos expression observed for instance in vehicle vs. apomorphine conditions, appear to be mostly due to increased levels of expression within the same cells (**Fig. 27.J, L, M**). We also observed that the gustatory areas (GU), previously shown to have increased levels of c-Fos positive cells upon learning of a reaching forelimb task[80], also showed and increasing trend in the levels of cells expressing c-Fos in task-trained animals, comparing to negative controls (**Fig. 27.N**).

Our preliminary data suggest that learning can lead to modest increases in the expression of the neuronal plasticity marker c-Fos. These seem to be reflected contralaterally in motor-related regions, including the striatum and motor cortical areas. Furthermore, task-trained animals seem to have an increase in the overall number of cells in these regions, as well as other non-motor regions previously suggested in a forelimb task[80], in comparison with vehicle-injected controls. However, these results need to be confirmed by increasing the number of animals analyzed, particularly those of control conditions.

4.3. Visualization and reconstruction of MSN dendritic spines

4.3.1. Optimization of a viral sparse labelling technique for visualization of MSNs

To assess changes in synaptic structural plasticity, resolution at the level of the single dendritic spine is needed. Labelling all neurons in a population would make it impossible to distinguish and reconstruct spines from specific dendritic segments and identify the somas these segments belong to. Thus, sparse labelling of neurons needs to be achieved. In order to do that, we adapted a viral approach already developed in the laboratory to express a fluorescent protein in a small subset of MSNs.

In our approach, an AAV mix is injected in the striatum of D1- or D2-MSN Cre-expressing mice. This mix contains two viral constructs, AAV-DIO-Flp and AAV-Con/Fon-EYFP, and the expression of a fluorescent protein, in our case EYFP, is only achieved in cells infected with both constructs. This occurs because the expression of EYFP is dependent on the Cre recombinase (expressed by the transgenic mouse) and Flp recombinase (expressed in the presence of the AAV-DIO-Flp construct). The construct encoding Flp is used in a diluted titer to allow for sparse labelling of a small subset of neurons. This dilution needed troubleshooting to achieve optimal sparseness.

Different titters of the viruses and injection sites were tested to achieve optimal sparse labelling of MSNs throughout the entire striatum. Two goals needed to be achieved:

1) The labelling needs to be sparse enough so that labeled neurons are relatively isolated from each other, but not too sparse as to lead to too few neurons being labeled;
2) The labelling needs to be spread out throughout the entire striatum, both dorsoventrally but also in the mediolateral (ML) axis, to achieve labelling of both DMS and DLS populations.

In the first group of viral injections, four D1-Cre animals were subject to one injection per hemisphere at one dorsoventral (DV) position. We injected the AAV mix, with a 1:400 dilution of the AAV-DIO-Flp, in the following set of coordinates: anteroposterior (AP) +0.8, ML +/-2.35, DV -2.0 mm **(Fig. 28.A)**. The viral injections revealed a clustered labelling of EYFP-expressing neurons mostly in the DLS region (**Fig. 28.B**). Even though a good spread of the virus was achieved dorsoventrally, its lateral spread was insufficient to target the DMS. Also, while some variability was observed, the sparseness achieved was insufficient to distinguish dendrites from individual neurons consistently (**Fig. 28.B –** right panel).

In order to efficiently label both the DMS and the DLS, we next tested another set of coordinates for a second injection per hemisphere. Four D1-Cre animals were injected in the following coordinates: AP +0.8, ML+/-1.2, to target the DMS, and AP+0.8, ML+/-2.4, to target the DLS (**Fig. 28.C**). We also tried to increase sparseness and achieve a bigger spread of the labeling on the DV axis, by dividing the injection at each ML coordinate by three DV locations: DV -2.0, -1.75, -1.5 for the DMS and DV -2.25, -2.0, -1.75 for the DLS **(Fig. 28.C)**. These new injection conditions allowed for good labeling of both DMS and DLS with a good DV spread **(Fig. 28.D)**. To further improve sparseness, we performed an additional dilution of AAV-DIO-Flp, so two mice were injected with a 1:800 dilution and two others were injected with the previous dilution of 1:400. Consistent with what was expected, the viral injections performed at the higher dilution (1:800) enabled sparser labelling (**Fig. 28.D-E**).

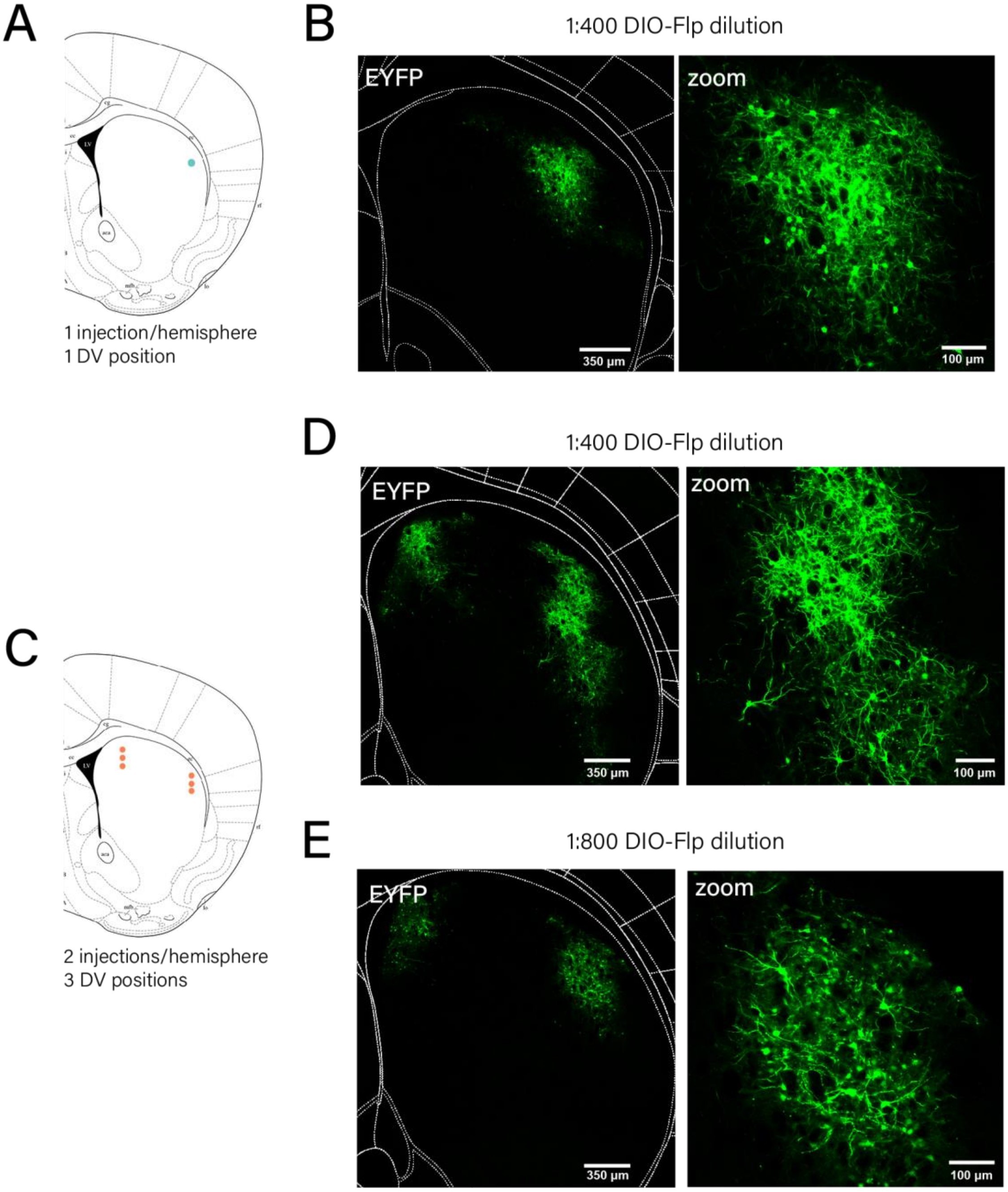

Figure 28 – Troubleshooting AAV injection conditions to achieve sparse labelling of striatal D1-MSNs with EYFP. (A) Coronal slice diagram depicting the location of the first group of injections (one injection and one DV location per hemisphere) at Bregma +0.8mm AP location. **(B)** Representative single plane brain slice overview, reconstructed from tiled confocal images (10x objective), showing the spread of the AAV-induced EYFP expression using the first set of injection conditions (1:400 dilution of AAV-DIO-Flp; one ML injection location). **(C)** Coronal slice diagram depicting the location of the second group of injections (three DV locations at two ML sites per hemisphere) at Bregma +0.8mm AP location. **(D,E)** Representative single plane brain slice overviews, reconstructed from tiled confocal images (10x objective), showing the spread of the AAV-induced EYFP expression, using 1:400 **(D)** and 1:800 **(E)** dilutions of AAV-DIO-Flp, injected at two ML locations. In **(B,D,E),** right images correspond to zoomed-in views of the DLS region in each slice. Images were aligned to the reference atlas.

Still, a higher sparseness of the signal was desired to have an adequate number of isolated neurons for dendrite imaging. Thus, we performed injections in a third group of animals, with higher AAV-DIO-Flp dilutions. In this case, A2A-Cre mice were used to test whether our viral approach would also efficiently label D2-MSNs, as expected. Four A2A-Cre animals were injected at different ML coordinates to the previous group: AP +0.8, ML+/-1.25, to target the DMS and AP+0.8, ML+/-2.35, to target the DLS. At each ML location, injections were again divided by the same 3 DV positions. Two of these animals were injected with a 1:1000 dilution of AAV-DIO-Flp and two others with 1:2000. Again, we observed that, despite individual variability, a higher dilution achieved a sparser labelling of neurons, although this not the case in the DLS region of the 1:1000 dilution but was observed in the DMS (**Fig. 29.B**). However, we found optimal labelling of neurons of both DMS and DLS populations with the 1:2000 dilution (**Fig. 2.9C**). Additionally, moving the DMS ML location allowed for a more efficient spread of the virus laterally in both dilutions (**Fig. 29**). We also confirmed that labelling of MSNs in A2A-Cre mice could be achieved similarly to the previous D1-Cre mice. (**Fig. 28 & 29**).

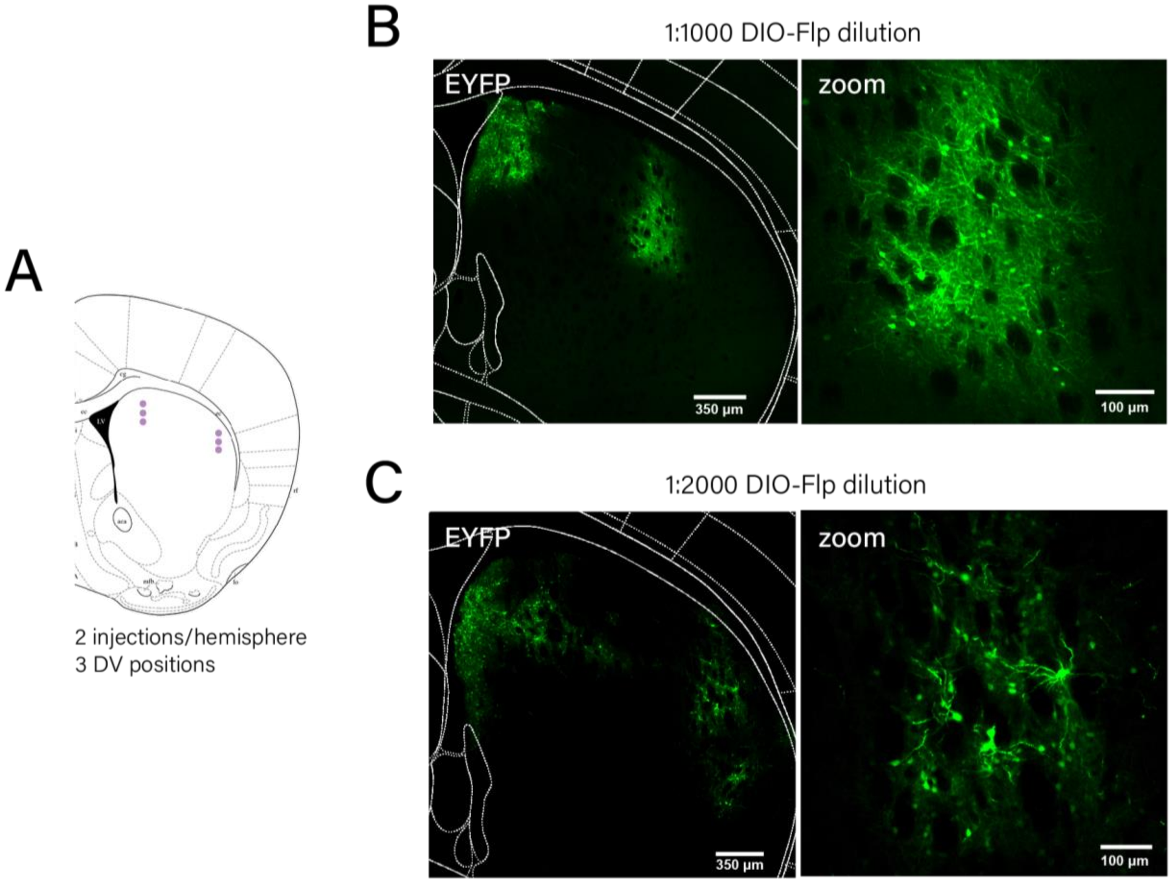

Figure 29 – Troubleshooting the AAV injection to achieve sparse labelling of striatal D2-MSNs with EYFP. (A) Coronal slice diagram depicting the location of the third group of injections (three DV locations at two ML sites per hemisphere) at Bregma +0.8mm AP location. **(B,C)** Representative single plane brain slice overviews, reconstructed from tiled confocal images (10x objective) of the spread of the AAV-induced EYFP expression, using a 1:1000 (**B**) and 1:2000 (**C**) dilution of AAV-DIO-Flp. In **(B,C),** right images correspond to zoomed-in views of the DLS region. Images were aligned to the reference atlas.

As the 1:2000 AAV-DIO-Flp dilution seemed to be the closest to achieve optimal signal sparseness, we imaged all slices containing EYFP signal in mice injected with this dilution. We observed that the signal was spread across 7-8 200µm slices, corresponding to a spread of approximately 1.4-1.6mm in the AP axis (**Fig. 30.A**), but found in optimal concentrations around the medial 4 slices (0.8mm in the AP axis). The slices containing the most adequate number of cells labelled are around the middle of this interval. We concluded that the 1:2000 dilution was sufficient to achieve an adequate sparseness of the signal, allowing for the visualization of individual dendrites and its tracing to the correspondent cell body (**Fig. 30.B**).

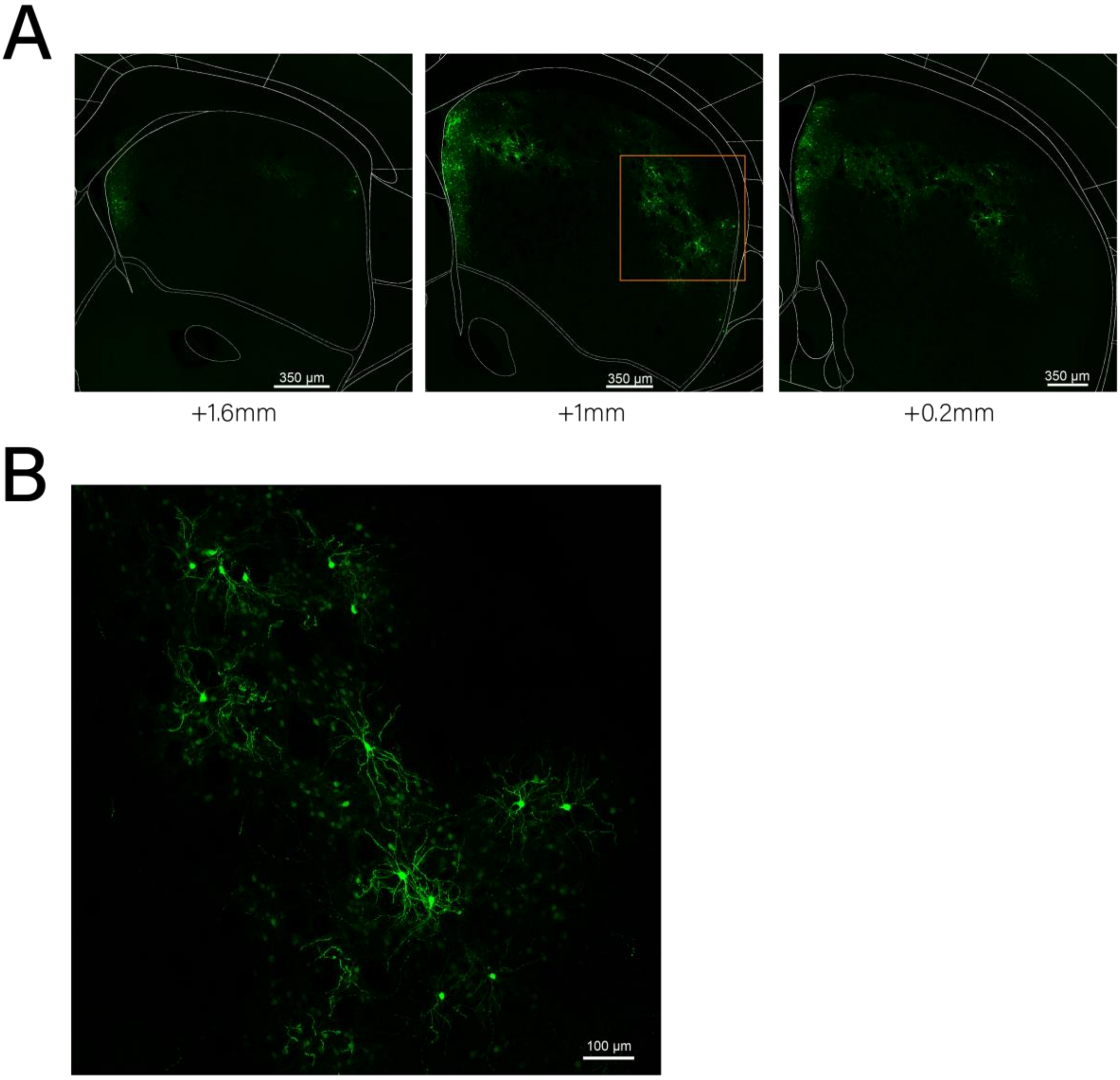

Figure 30 – Sparse expression of EYFP in striatal D2-MSNs using the 1:2000 dilution of AAV-DIO-Flp. (A) Single plane brain slice overviews, reconstructed from tiled confocal images (10x objective; aligned to the reference atlas) at the indicated proximal AP locations (relative to Bregma), showing the spread of EYFP expression. **(B)** Maximum intensity projection of high-resolution image z-stack (20x objective), of the DLS region delimited by the orange square in **(A).**

4.3.2. Detection and reconstruction of dendritic spines using high-resolution confocal microscopy

Morphological features of spines, including size, shape and density, reflect important synaptic functional attributes and the potential for plasticity. To examine the changes in structural plasticity upon motor learning, we first needed to establish the imaging and analysis protocol.

Having already established the labelling technique, we proceeded to optimize the imaging and post-processing of dendritic segments. We collected high-resolution confocal images of dendritic segments, and, prior to image analysis, those images were deconvolved with the Huygens software. The result was an increase in resolution and signal-to-noise ratio that improved spine reconstruction and analysis (**Fig.31;** spine detection using raw images not shown). We then compared the efficiency and limitations in spine detection and morphology analysis with Neurolucida360, a commercially available software, and Vaa3D, an open software with a recently described spine detection tool[124,129]. Example reconstructions achieved by each software are shown in **Fig. 31**.

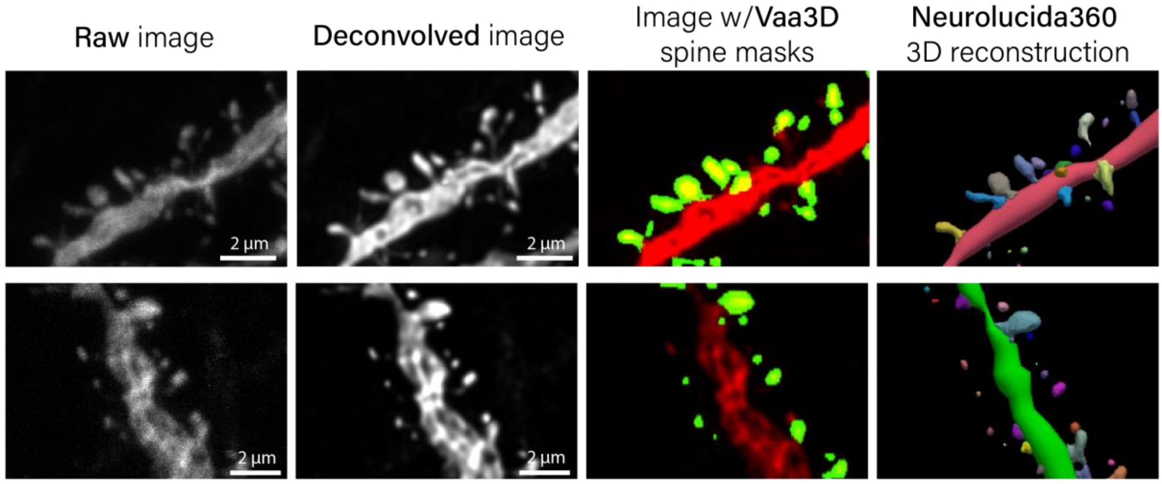

Figure 31 – Dendritic spine image processing and detection. Prior to analysis, images of dendritic segments were deconvolved to improve resolution and signal to noise ratio. Spine detection was done using Vaa3D and Neurolucida360. Shown are representative raw and deconvolved images of 2 different dendritic segments, the corresponding spine mask images obtained with Vaa3D and the full reconstruction with Neurolucida360. Vaa3D spine mask images show the accepted spine volume mask for each spine in green and the deconvolved EYFP signal in red. Neurolucida360 output images display 3D reconstructions of both dendritic shaft and spines.

We performed spine reconstruction and analysis of a set of dendritic segments from D1-MSNs sparsely labeled with EYFP, using both software. We found no significant differences ($p=0.6407$) between the length of the dendritic segments detected by each tool (**Fig. 32.A**), however, we observed that the values between the two software were not well correlated ($R^2=0.6371$; figure not shown). The total number of spines per segment obtained with Neurolucida360 and Vaa3D was well correlated ($R^2=0.87581$; **Fig. 32.B**). Interestingly, the spine density (given by the number of detected spines per µm) was significantly lower ($p=0.0113$) when using Vaa3D, in comparison with Neurolucida360 (**Fig. 32.C**), and the mean spine density for each segment was not well correlated between the two tools ($R^2=0.58919$; **Fig. 32.D**). On average, Vaa3D detected ~72% of the number of spines per segment that was detected by Neurolucida360. Interestingly, we observed that spine detection using Vaa3D was mostly affected in lower volume spines, with only 55% of spines being detected between an interval of 0-0.05µm^3, when comparing to the results achieved with Neurolucida360. These were most likely detected as having a higher volume, given the positive difference in the percentage of detected spines in the interval of 0.05-0.1 µm^3(148%) and 0.1-0.15 µm^3 (151%) (**Fig. 32.E**). On the other hand, the number of spines detected by Vaa3D above sizes of 0.15 mm^3 was consistently smaller than that detected by

Neurolucida360, except on two size bins (**Fig. 32.E**), indicating decreased spine detection at a large range of sizes.

Figure 32 – Vaa3D has a lower sensitivity for spine detection than Neurolucida360. (A) Total dendritic length detected for each segment. **(B)** Correlation between the total number of spines detected in each segment,

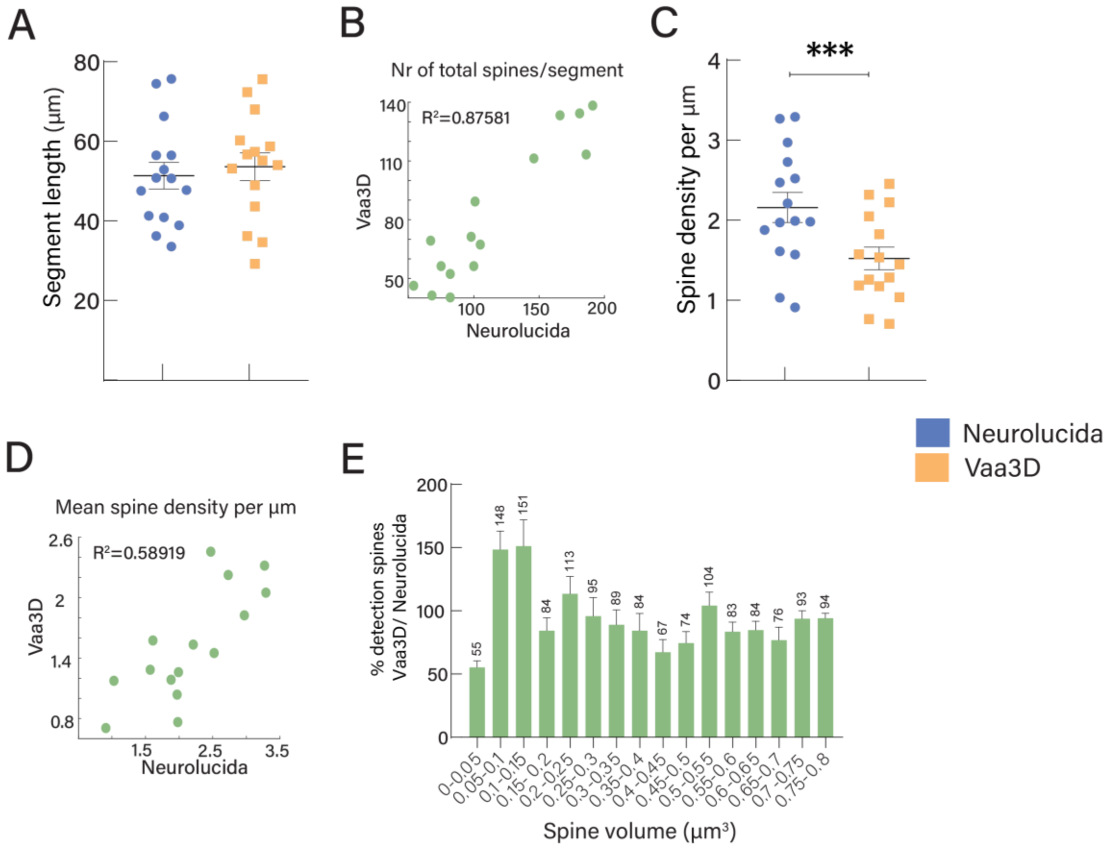

by Vaa3D vs. Neurolucida360. **(C)** Mean spine density per µm, calculated as the ratio of the total number of spines detected by the total segment length **(D)** Correlation between the mean spine density per µm, by Vaa3D vs. Neurolucida360. **(E)** Percentage of spines detected by Vaa3D as compared to Neurolucida360 at a range of different volume intervals; the mean value is shown above each bar. Differences between length of dendritic segment and spine density per segment detected by each software were determined by a paired t-test (*** - $p \leq 0.001$; non-significant for the segment length). n=15 segments; error bars=S.E.M.

To further dissect differences in spine detection between the two softwares, as well as characterize the normal range of MSN spine parameters, we analysed differences in spine morphology results. Despite differences in detection between the tools, we observed that the vast majority of spines have less than 0.3 µm^3 (**Fig. 33.A**, $\text{mean}_{\text{Neurolucida360}}=0.124\mu m^3$, $\text{mean}_{\text{Vaa3D}}=0.132\mu m^3$). Interestingly, Neurolucida360 detects spines as having smaller spine heads (**Fig. 33.B,** $\text{mean}_{\text{Neurolucida}}=0.325\mu m$, $\text{mean}_{\text{Vaa3D}}=0.57\mu m$) whereas Vaa3D detects smaller spine lengths (**Fig. 33.C,** $\text{mean}_{\text{Neurolucida}}=1.039\mu m$, $\text{mean}_{\text{V3D}}=0.841\mu m$). These differences could both be explained by differences in the calculation of each parameter. For example, while Vaa3D counts the length as a straight line between spine base and head limit, Neurolucida360 measures the length throughout the entire spine backbone (**Fig. 33.C,** top inset). Additionally, these differences could reflect the contribution of spines detected by Neurolucica360 that are not detected by Vaa3D. Our results suggest that Vaa3D seems to have lower sensitivity for spine detection, having a significantly lower number of spines detected, when compared with Neurolucida360, and which is mainly reflected in the detection of low volume spines.

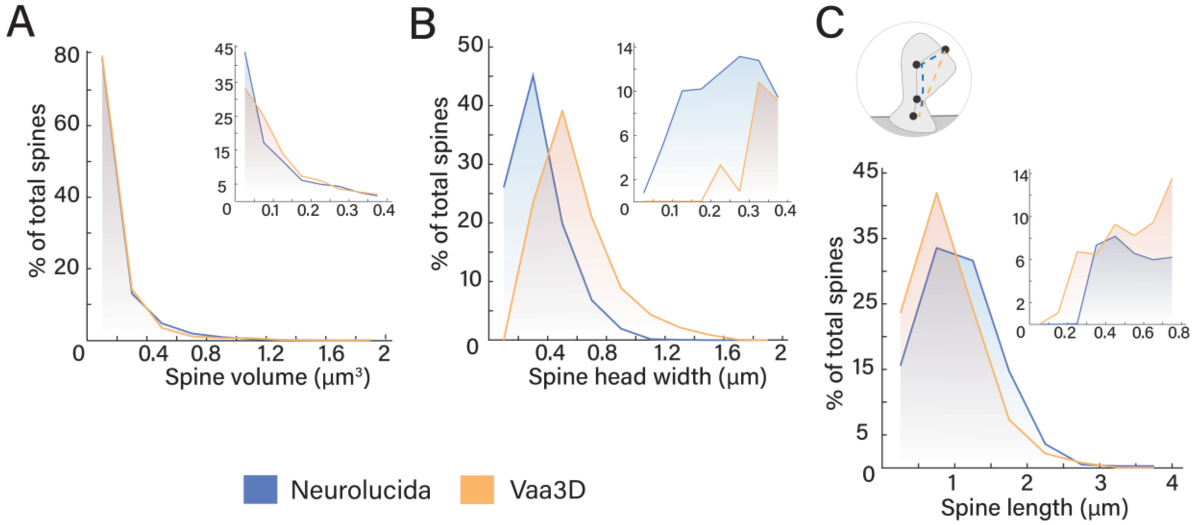

Figure 33 – Detection of different spine parameters highlights sensitivity and algorithm differences of Vaa3D and Neurolucida360. **(A-C)** Line histogram of the total distribution of spines per spine volume **(A),** spine head width **(B),** and spine length **(C).** Binning corresponds to 0.2 µm in the main plots of **(A)** and **(B)** and to 0.5 µm in **(C).** In the inset plots, binning is 0.05 µm in **(A)** and **(B),** and 0.1 µm in **(C).** In **(C)** the top inset depicting a spine diagram highlights differences in how the spine length parameter is calculated between Vaa3D (orange dashed line) and Neurolucida360 (blue dashed line).

Additional measurements of spine morphology, including size of the spine neck, head volume and distance to the soma, are important when studying structural plasticity. Spine classification has been previously performed taking into consideration 3 morphological parameters: spine length, head and neck size. Because spine parameters in Vaa3D are limited to volume, spine length and head width, we studied spine morphology using only data obtained by Neurolucida360. We performed this classification based on previously established ratios in hippocampal CA1 neurons[125], that have also been applied to studies in MSNs[105,126]. Filopodia were classified as any spine with a length bigger than 3µm (**Fig. 34.A**).

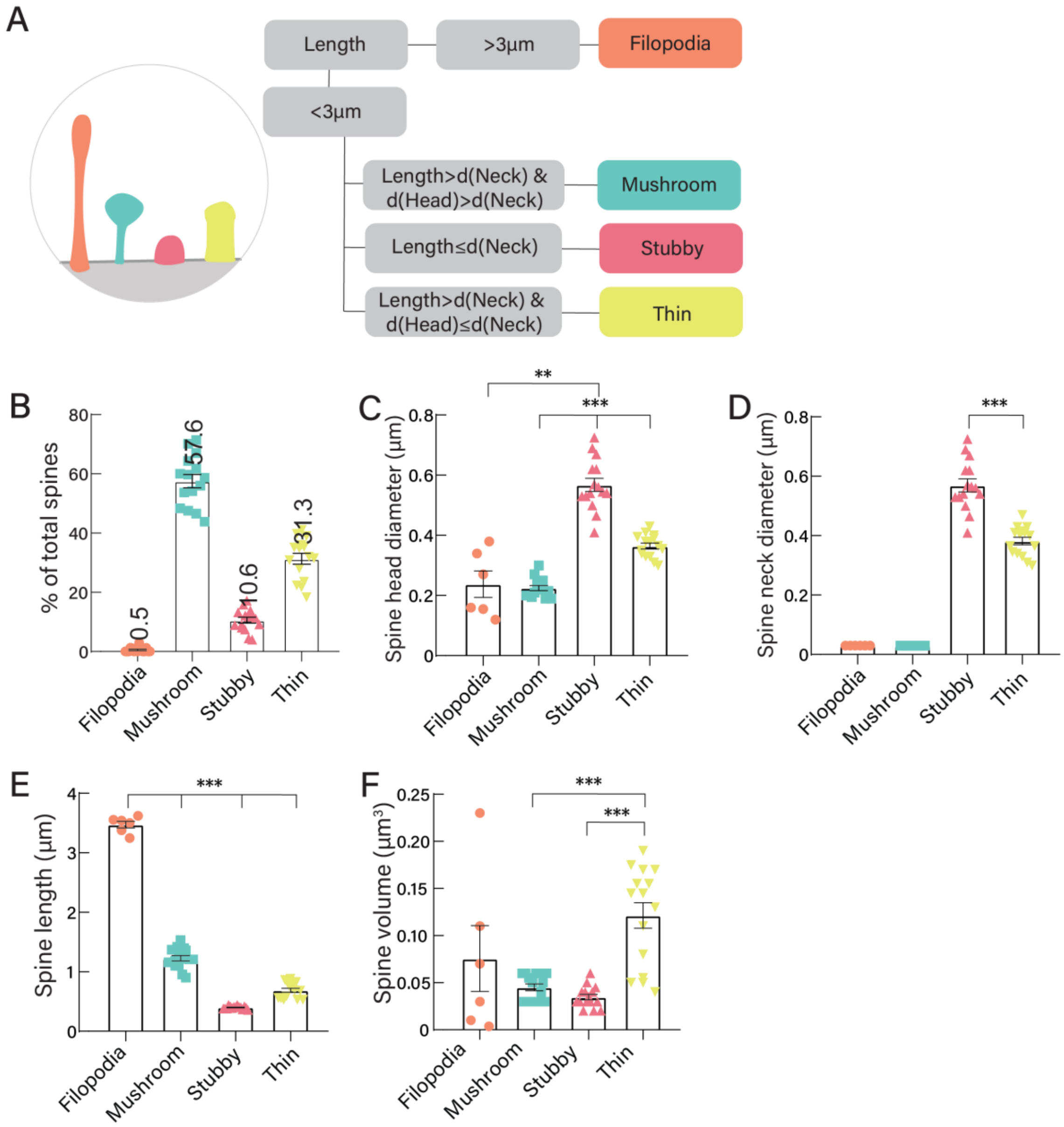

Figure 34 – Dendritic spine morphology of adult mouse D1-MSNs. (A) Spine classification was done by taking three measurements from each spine – length along the backbone, head width, and mean neck diameter – as shown in the diagram. Left inset depicts putative shape of each type of spine. **(B)** Percentage of spines of the indicated type per segment (n=15 segments; total spines analyzed: 8 filopodia, 968 mushroom, 185 stubby, and 541 thin). **(C)** Mean spine head width of each spine type. **(D)** Mean spine neck diameter of each spine type. **(E)** Mean spine length of each spine type. **(F)** Mean spine volume of each spine type. Differences between the spine morphological groups were analyzed by performing a Mixed effects test (***$p \leq 0.001$; ** $p \leq 0.01$); note that in **(D),** no statistical comparisons were performed for filopodia and mushroom spines. Multiple branched brackets represent statistical difference between all group combinations within the brackets. For **(C-F),** individual segment values represent the median. n=15 segments; error bars=S.E.M.

Under our experimental conditions and classification parameters, adult mouse D1-MSN dendritic segments were mostly composed of mushroom spines (57.6%), followed by thin spines (31.3%), and lastly by stubby spines (10.6%) and filopodia (0.5%) (**Fig. 34.B**). Interestingly, stubby spines showed significantly larger head widths, despite this not being a criterion for classification. Despite the name, thin spines had the second largest head width followed by mushroom spines and filopodia (**Fig. 34.C**) ($p<0.001$). Stubby spines also showed significantly larger necks

($p<0.001$). Mushroom spines and filopodia had the thinnest necks (**Fig. 34.D**). The shortest spines were the stubby spines, followed by the thin ones, which were both significantly smaller than the other two types ($p<0.001$). As expected, filopodia were found to be the longest type of dendritic protrusions, being significantly longer than mushroom spines ($p<0.001$) (**Fig. 34.E**). Lastly, we observed that thin spines have significantly more volume than the other spine types ($p<0.001$), followed by mushroom spines, stubby spines and filopodia. (**Fig. 34.F**).

Our data shows that D1-MSNs from vehicle-treated mice have high spine density (1.5-2.2 spines/μm). D1-MSNs are composed of different spine types, which can be characterized by their distinct morphological features. We found that these neurons are mainly composed of mushroom spines (>50% of all spines), i.e., mature-type spines composed of a distinguishable thin neck, in comparison to the head size. The least common spine types were filopodia and stubby spines (less than 12% of all spines).

5. Discussion

Learning to perform a new motor task involves different brain areas as well as the optimization of different behavioral features. It is known that changes in neural activity in the striatum occur during motor learning[2,47,52]. Changes in corticostriatal functional plasticity have been shown to occur in the dorsomedial striatum early in training, and later on in the dorsolateral striatum, as skills become habitual[2]. In this work, we set out to establish the tools and techniques needed to study dendritic spine plasticity upon motor task learning, using fixed brain slices. We trained wildtype mice in a lateralized lever pressing task for a 10-day schedule. Mice learned the action-outcome contingency, i.e., to press the lever to receive a reward, but did not reduce the variability in all measures of performance. Particularly, even though mice were trained in a FR4 schedule, most animals did not learn to press in sequences of 4 presses, and the inter-press interval (both inter-sequence and within-sequence) did not significantly decrease. We studied the expression of c-Fos, which we confirmed as marker for dopamine-induced neuronal activity, in the brain of pharmacologically treated animals. We found that some regions involved in motor behavior, including the striatum and the primary motor cortex, showed an increasing trend for the number of c-Fos positive cells in the contralateral hemisphere, as compared to the ipsilateral one. However, we need to analyze more animals before reaching definitive conclusions on the statistical significance of these trends. Additionally, the expression patterns of c-Fos in task-trained mice were compared to preliminary data on c-Fos expression in apomorphine- and vehicle-injected mice, acting as positive and negative controls for c-Fos expression, respectively. Task-training appeared to increase the number of cells expressing c-Fos in comparison to negative controls, in multiple brain areas, but, again, this needs confirmation by increasing the number of animals analyzed. Lastly, we established a viral sparse labelling technique that allows the visualization of individual dendritic segments, as well as their spines. With this labelling technique, we studied dendritic spine detection by two different software and characterized D1-MSN spine morphology in vehicle-injected controls. We found that Neurolucida360 has higher sensitivity to spine detection than Vaa3D, which is mainly reflected in the detection of low volume spines. Still, we found that D1-MSNs have an average spine density of 1.5-2.2 spines/µm, and that the most common type of dendritic spines were mushroom, followed by thin spines.

Here, we discuss the results obtained in this work as well as its limitations and propose potential ways of overcoming them. We also describe alternatives to some of the methods deployed and highlight important future experiments. Lastly, we discuss the impact that this ongoing work may have in our understanding of striatal MSN function, and its relevance in the field of basal ganglia and related motor circuitry.

5.1. Mice learn to press the lever for reward, but do not form long sequences

We showed that mice can learn a self-operant paradigm and refine specific behavior features. In this task, two features must be learned – animals need to learn to press the lever to achieve reward and be able to do it even after increased difficulty upon lever retraction. This can be divided into a motor skill component (pressing the lever after its retraction, which is challenging), and a cognitive component of learning to press in sequences of at least four lever presses. Mice progressively adapted to lever retraction, which imposes laterality in pressing and allows for pressing with only one forelimb, in most animals. At the same time, mice significantly decreased the time until session completion, while increasing the number of lever presses per session. The intersequence interval decreased significantly with training when looking at all sessions. Looking further into sessions of FR4 schedule, mice significantly increased press velocity. However, mice were unable to increase the number of presses per sequence up to the target value of four presses. Since this is a performance relevant feature, one could think that if an animal optimizes its lever presses to be performed in bouts, it could lead to a decrease in effort needed to obtain reward. However, this rationale may be incorrect; rather, performing lever presses in longer bouts may not be the most efficient strategy for every mouse.

In our schedule, there was no time contingency for the time the animal took to achieve four presses, and sequences were not reset if animals left the lever area. We hypothesize that, in the absence of a time contingency in this task and/or a (spatial) criteria the defines sequence during performance, animals will not be pressured to cluster presses in sequences of four to receive a reinforcer. This is further reinforced by the increase in task difficulty that the lever retraction represents. In previous papers from our lab and other groups, animals trained in a lever press task (which had two levers available) could achieve the desired sequence length, even in the absence of time contingency and for longer sequences, such as a FR8 schedule[40]. This highlights the difficulty of our lateralized motor learning task, and that, in the absence of a time restriction, each animal will develop different strategies. Still, other factors can come into play in determining whether an animal performs movements in longer bouts. These can include differences in schedule (including previous schedules of reinforcement, number of daily sessions, etc) and differences in box design (such as the floor, which in some boxes is composed of metal bars, and in our boxes is acrylic), and forelimb preference (which might be mitigated by the presence of two levers). Further, the distance between the lever and the magazine (where reward is delivered), which might differ between paradigms, can affect the effort needed for the animal to check the magazine for rewards between lever presses.

In a previous study using a lever pressing task in which mice were trained to press a lever at increasing frequency, animals reduced frequency variability but increased sequence duration. When trained to press an exact number of lever presses, the frequency increased. This demonstrates that there is a differential modulation of the components of the task space during learning, according to what is being reinforced[130]. This might explain why we did not observe a decrease in both inter-sequence and within-press interval, given that there was not a reinforcement (besides maximum session duration) that would modulate these parameters, i.e., there was not any restriction that would modulate a decrease in any of these measures.

Whether this component of the task (i.e., learning to perform longer sequences with a defined number of LPs) would be important in establishing a long-lasting motor skill is uncertain. It would be interesting to understand how plasticity upon task learning is modulated in animals trained for the same amount of time, with and without a time contingency, and whether learning this sequence contingency is important for maintaining a long-lasting skill.

One other important factor in a forelimb task, is that mice, as humans, display lateralization in terms of the preferred forepaw (i.e., handedness). In C57BL/6 male mice, this lateralization follows a U-shaped distribution, with only a small number of mice being ambidextrous in food retrieval procedures[131,132]. In our experimental conditions, there was no assessment of individual handedness prior to the start of the task, and animals were randomly chosen for training with either their left or right paw. This could entail that animals performing the task with their non-preferred paw have a harder time adapting to the task difficulty and this could differentially affect performance-relevant features and increase inter-subject variability. One can get a sense of how this may affect task performance by analyzing the one mouse in the cohort which performed the task with the opposite paw to what was expected. Despite the increase in difficulty, the animal continued to use its right paw on a “left paw” lever box. While it initially finished the sessions earlier (and obtained all reinforcers available), and before either lever retraction perform sequences containing a median of 3 presses, upon full lever retraction it performed mostly isolated presses (i.e., sequences of 1 lever press) until the last training session.

The variability in the speed at which different animals learn, is an important aspect that contributes to the overall variability of the behavior parameters. Two possible solutions could be used to overcome this issue. One is to train animals with a time restriction and for a longer period. The other, which can be combined with the previous one, is to define minimum performance criteria and only move animals forward in the task schedule upon completion of such criteria. In fact, other studies using lever pressing tasks frequently define criteria, which also helps to establish what is an early vs late time point in learning[43].This could entail for instance, only training animals in a FR4 schedule with time contingency after animals performed at least a certain number of lever presses without it. Particularly, it might be important to fully retract the lever only after animals have obtained a certain number of rewards in FR4mid sessions.

5.2. Most mice did not significantly decrease press trajectory variability

One dimension considered to be important in skill learning is the variability in the trajectory performed by an individual until it reaches the desired target. With time, trajectories should become less variable, as an outcome of optimization. Indeed, studies in rodents have reported decrease in variability of forepaw trajectories with learning in different paradigms, including lever pressing[55] and food reaching[127]. There are many possible trajectories that a mouse's paw can perform to press the lever. To analyze this component of skill learning, we looked at movement kinematics upon full lever retraction. We showed that when looking at the average variability of trajectories within each session for all animals, there was not a decrease in trajectory variability. We looked at different measures of trajectory variability, including the sum of Euclidean distances and discrete Frechet distance, measures of similarity between two sets of points (curves)[127]. The higher these distances are, the more dissimilar are the two trajectories being analyzed. We observed that these measurements varied very similarly throughout sessions, and neither of them showed a significant decrease in trajectory variability. Interestingly, looking at the mean standard deviation (STD) of trajectories point-by-point, we found that there was a significant increase in trajectory variability. These three measurements give us a depiction of movement kinematics at different dimensions. While the first two measurements give information about the similarity and distance between all points in a trajectory, the latter only takes into consideration how similar in space are two corresponding points of different trajectories. If the mean STD of trajectories decreases, the Euclidean and Frechet distance will decrease as well, while the opposite may not necessarily occur. And so, it is possible to have an increase in STD, which is not reflected in the other two measurements, which can indicate that animals perform similarly shaped trajectories (better measured with Euclidean and Frechet distance measurements) that are different (i.e., dislocated) in space (better measured by STD).

The absence of a decrease in trajectory variability could be expected if we take into consideration other performance results as well as the limitations of this analysis. First, some mice were still in an early stage of learning, even in later sessions, as measured by the low number of presses and/or high percentage of isolated lever presses. Some were already decreasing variability in different performance measurements while others were not. As mentioned before, defining task criteria that mice must complete to move forward into a more difficult training stage could be a way of reducing variability. Second, the issue of handedness can affect performance in different aspects, including press trajectories. It is very likely that mice performing the task with their non-preferred paw have more trouble decreasing variability in this dimension. Another interesting observation is that isolated presses are more dissimilar between each other (as measured by mean STD) than presses in sequences. At the same time, we observed that animals did not significantly increase the percentage of non-isolated LPs. We hypothesize that reducing the percentage of isolated presses to a residual value should have a positive effect in reducing trajectory variability. This could likely be achieved by implementing a gradually increasing time restriction on the FR4 schedule, as in previous studies[133,134].

As previously highlighted in **Section 4.1.2.,** some animals could develop more than one optimized lever press trajectory (i.e., different 'types' of lever presses). Because our analysis compares all trajectories as being the same, there can still be a decrease in variability occurring within each type of press, which we are not evaluating. Cluster analysis could potentially identify these different types of lever press trajectories and clarify whether variability is being decreased within each cluster or not. It would also be interesting to analyze whether different types of presses are performed in similar contexts. It could be possible, for instance, that the first or last press in a sequence represent a different spatial cluster than middle presses.

Lastly, it is important to note that raw trajectories corresponding to one press are usually composed of around 20-40 points in each axis. While we acquired videos at a rate of 100 frames per second, which means that we have a trajectory data point every 10 milliseconds, acquiring at even higher frame rates would allow for each raw trajectory to be composed of more points. We do not consider this to be a significant problem in our analysis, but it can potentially account for some of the variability observed.

5.3. The number of cells expressing c-Fos is increased upon task training

One of the objectives of this work was to study how motor learning modulates the number of cells expressing c-Fos, as a proxy for recent neuronal activity. Understanding whether motor task learning leads to differences in expression of this marker is important, as we plan to study structural plasticity specifically in MSNs that were active upon motor learning. We used a recently published whole-brain cell detection pipeline, BrainJ[123], to perform c-Fos-positive cell detection and atlas mapping in an unbiased manner, in task-trained, and apomorphine- and vehicle-treated animals. Given that we had data for all brain regions represented in the slices stained, we decided to study not only c-Fos expression in the striatum but also in other regions of interest. These included regions previously shown to have increased levels of c-Fos expression in a forelimb task[80], such as the primary and somatosensory motor cortex, and areas that were not related to motor behavior but had high basal levels of expression.

Even though a larger number of mice, especially controls, would be needed to take solid conclusions, our results seem to suggest that task training may lead to increases in c-Fos expression. We observed that task-trained animals appear to have higher numbers of cells expressing c-Fos when compared to vehicle-injected controls, and even resemble the apomorphine control in some brain regions. These include cortical motor areas, such as the primary and secondary motor cortex, as well as regions of the primary somatosensory cortex. Additionally, increases were found in non-motor areas, such as the gustatory areas (GU) and barrel field region of the somatosensory cortex. Our results seem similar to the results reported by M. Mathis for a head-fixed forelimb reaching task, in which increases in cortical motor (including forelimb somatosensory area) and GU areas, as well as posterior striatum, were found in task-trained animals versus controls[80]. Other non-motor related regions such as the anterior cingulate cortex (ACC) and the piriform cortex (PIR) seemed to have almost no difference in the number of cells expressing c-Fos between groups in our work. Likewise, Mathis also reports high basal levels of expression in the ACC and PIR, which in some regions are significantly higher in controls than task-trained mice[80]. However, we observed a notable difference in the intensity of c-Fos expression at the cellular level in the ACC and PIR between vehicle/task-trained and apomorphine mice. While we did not analyze expression levels, it is important to note that some regions could have further differences at this level. The regions that had a higher number of cells expressing c-Fos in the apomorphine-injected mice were the striatum and nucleus accumbens. This was expected given that both regions are composed mostly of MSNs, that have D1/D2-receptors through which apomorphine exerts its agonistic effect, and has been reported to lead to robust increases of c-Fos in comparison to saline controls[115].

As for the levels of c-Fos expression in control and pharmacologically treated mice, previous reports studying whole brain c-Fos expression in different contexts have found conflicting results. In one study, animals were subjected to either saline or haloperidol (an antipsychotic known to increase c-Fos expression in the striatum[135]) exposure[136]. Saline-injected animals had ~10 000 c-Fos positive cells in the striatum (caudoputamen), and haloperidol-injected animals had ~100 000 c-Fos positive cells in the same region[136]. These values are in the same range as our results regarding vehicle/apomorphine-injected mice. On a different report, researchers studied c-Fos expression upon saline or cocaine (a dopamine transporter blocker that leads to acute c-Fos expression[115]) injection, which were exposed to an open-field afterwards. Surprisingly, the authors describe only a total count in all brain regions of ~66 000 c-Fos positive cells in the saline mice, and ~97 500 nuclei in cocaine injected mice[137], for a similar span in the AP axis to our work. These results are very different both in comparison with our data, and the previously mentioned work[136]. This may reflect technical differences, which can include the software used for cell detection, the antibody used for staining of c-Fos-positive cells, as well possible differences in criteria for cell detection. Neither of these manuscripts address whether inter-hemispheric differences were observed in any of the conditions studied.

Analyzing differences in the number of c-Fos-positive cells in the contralateral and ipsilateral hemispheres to the trained paw, we found non-significant trends for higher c-Fos expression in multiple contralateral brain regions involved in motor output. These results are variable but are overall within the range of 10-20% when looking at the ratio of the number of c-Fos-positive cells in contra- vs ipsilateral hemisphere, and include the striatum, primary motor cortex and forelimb sensory motor cortex. While statistical significance was not reached in our work, possibly due to the reduced number of animals that we were able to analyze, these differences seem to be consistent between different mice. On the other hand, we were expecting to see a similar difference in the mouse that learned the task with the opposite paw to that expected, given that it still learned the task. However, this mouse had almost no inter-hemispheric differences in the number of c-Fos-expressing cells in the striatum, while all other regions showed a higher number of cells in the ipsilateral region to the lever pressing paw. Our results suggest that c-Fos levels are increased contralaterally upon task training, with some variability between animals, but other factors might come into play in this increase. Interestingly, in a recent preprint where rats were trained in a lateralized lever pressing task, increases were observed in the number of striatal D1-MSNs expressing the zif-268 marker[44]. This increase was around 5% when comparing the contra- vs ipsilateral hemisphere as a ratio of total number of cells, and was found to be statistically significant[44]. Even though the task and activity marker are different, these results seem to agree with our observations and may highlight that task-training only modestly increases the number of cells expressing an immediate early gene contralateral in a lateralized motor task.

Interestingly, the only motor-related area in our results which did not show contralateral increases was the secondary motor cortex (MOs). In our dataset, there is a higher representation of caudal slices versus rostral ones. In Mathis's work, for instance, the MOs shows a significantly higher value in task-trained mice in rostral slices and higher values in medial and caudal slices for controls[80]. Importantly, in Mathis's work there is no mention of whether the differences in expression are lateralized and whether these differences reflect changes in intensity and/or in the number of c-Fos expressing cell, preventing further comparisons with our results. Previous studies have shown that expression of the immediate early gene Arc in the MOs increases with motor learning in a rotarod task, and inactivation of this region disrupts learning[73]. However, another report has showed that secondary motor cortex lesions do not affect learning of the motor action itself, in that case lever pressing[138]. Rather, it affects the ability of the mice to adjust behavior upon outcome revaluation, i.e., to switch between automatic and goal-directed actions when prompted[138]. Thus, while this cortical region is involved in certain aspects of motor learning, it is unclear whether a contralateral increase in c-Fos expression with task learning would be expected.

We found that the two vehicle controls had a higher number of cells expressing c-Fos in the left hemisphere for almost all regions analyzed, while the apomorphine-treated mouse had lower inter-hemispheric differences. We interpret this result in the apomorphine individual as being a consequence of the robust increase in c-Fos upon apomorphine injection, which could attenuate hemispheric differences given that it is such a strong stimulus. We hypothesize that the differences observed in vehicle-injected animals, which show consistent increases on one hemisphere, may be due to lateralization. In addition, the degree of inter-hemispherical differences between vehicle-injected mice are quite similar to the ones observed in task-trained animals. It could be that in the absence of any training or pharmacological treatment, animals still have higher levels of c-Fos expression naturally on one side. This could reflect, for example, the contralateral representation of the preferred paw. Interestingly, in the preprint that observed small increases in the number of cells expressing Zif-268 contralaterally in task trained animals, yoked animals (exposed to the same number of rewards but did not perform the task) also had a small non-significant difference in the percentage of cells expressing the marker between hemispheres[44]. Analyzing more brains of both vehicle and apomorphine mice would be needed to confirm whether these inter-hemispheric differences are naturally occurring and what is its variability. If we would find a U-shaped distribution in inter-hemispheric differences in the number of cells expressing c-Fos, that would parallel the normal distribution in handedness[132]. We hypothesize that in task-trained mice contralateral differences should not be of random nature or reflect just handedness, given that we randomly analyzed a similar number of animals trained with their right and left paw and consistently observed contralateral differences. In addition, we hypothesize that the differences observed in controls, which could be of random nature and/or reflect handedness, could also explain the variability in percentage of contralateral modulation in task-trained animals.

Overall, our results seem to suggest that task training in the lateralized lever pressing task can increase the number of cells expressing c-Fos. We describe for the first time that motor related areas may have modest increases in contralateral expression of c-Fos, relative to the trained paw. In addition to the small sample size, there could be some other possible drawbacks to this conclusion. It is unclear how forelimb preference affects c-Fos expression in this task. We speculate that animals performing the task with their preferred forelimb have different levels of expression than animals performing the task with their non-preferred forelimb, increasing variability. It is also important to consider that animals were at different stages of motor learning, and this could also account for some of the variability observed. Early studies of c-Fos expression upon cocaine injection and motor learning show that the number of cells expressing c-Fos increases in striatal regions with training, peaking during early training and decreasing to control levels later in learning[70,77]. While it is unclear what is the role of cocaine in modulating c-Fos in the context of motor learning, these results may indicate that different levels of c-Fos expression occur with training and skill consolidation, as other studies using different markers of plasticity have highlighted[43]. Thus, it would be important to address whether c-Fos levels also change dynamically with learning stages in our lateralized motor learning task.

5.4. Studying structural plasticity in fixed brain slices

Previous work has demonstrated that corticostriatal synaptic plasticity occurs during motor skill learning[2,51,139], but it is unclear whether dendritic spine structural changes also occur in this context. Thus, the long-term goal of the project that this thesis is a part of is to determine whether motor skill learning induces changes in dendritic spine density and volume in D1- and D2-MSNs. First, we aimed at establishing a state-of-the-art viral approach to sparsely label MSNs with EYFP. This technique allows for visualization of the whole dendritic arbor of neurons and its spines. We show that with this technique, we were able to achieve sparse labelling of both dorsomedial and dorsolateral populations of D1- and D2-MSNs. Further, in this work we show that we can achieve spine imaging and reconstruction using high-resolution confocal microscopy and two different software tools.

We performed preliminary density measurements and a morphological classification of D1-MSN spines from dendritic segments of vehicle-treated animals. Our spine density results suggest that D1-MSNs have somewhat higher values of spine density than what some other works have previously reported[104,110]. In our study, we observed a mean spine density of ~1.5 spines/µm when using Vaa3D, and ~2.2 spines/µm when using Neurolucida360. Interestingly, previous studies analyzing MSN spine morphology have found a wide range of dendritic spine density, with the highest being ~1.5 spines/µm[102,104,105,110,111]. Among these studies, the ones using high-resolution confocal microscopy[104,105,111] show spine densities in the 1.1-1.5 range, close to the values we found using Vaa3D. In these papers, the two studies performed in rats[105,111] show a slight increase in density in the DMS (1.3 and 1.5 spines/µm [105,111]) in comparison to the DLS (1.1 and 1.2 spines/µm [105,111]), but no distinction between MSN-subtype is performed. On the other hand, in the study performed in mice, authors found a mean spine density of ~1.2 spines/µm in both D1- and D2-MSNs of the DMS[104]. Other studies, using brightfield microscopy (often paired with Golgi-cox staining)[102,110,126], report a range of spine density values between 0.5-1.3.

We argue that differences in spine density observed between the different studies are most likely due to methodological issues. Differences in tissue processing, imaging resolution and image processing and analysis can greatly influence spine detection. Lower resolution and/or undersampling, for example, might not capture all spines in a dendritic segment. As far as we could tell from the reported values, our study used the smallest XY pixel size and a deconvolution step that not all studies have used. These are factors that could improve spine detection. Moreover, our comparative study shows that different software like Vaa3D and Neurolucida360 can yield significantly different results on spine detection in the same dendritic segments, highlighting how different analysis methods can yield very different results. Still, our results may not accurately represent overall spine density in MSNs, given that we had a small sample size (15 segments total from 2 animals) and imaged mostly proximal dendritic segments at <100µm from the cell body. In fact, the distance of dendritic segments from the cell body[110], as well as DMS vs. DLS location[105,111] are also factors that determine spine density that may contribute to the variability between studies. Additionally, there could be species- and age-specific differences, as well as MSN type-specific differences.

As for spine morphological classification, we observed that the most common subtype of D1-MSNs were mushroom spines (~58% of all spines), followed by thin spines (~31% of all spines). Stubby spines accounted for a little over 10% while filopodia were less than 1% of all dendritic protrusions analysed. Our results seem to agree with previous studies describing spine morphology in striatal MSNs of control animals. In the two studies previously reported that used confocal microscopy in rats, both describe the most common type of spines as the mushroom type. One study describes ~30-40% of all spines as mushroom spines, and ~22% of both stubby, thin and filopodia spines, with no distinction between MSNs subtype[111]. The other describes 35-50% of all spines in D1-MSNs as being of the mushroom type, followed by 38-45% of thin spines, with the highest percentage of mushroom spines in the DMS, and lowest in DLS[104]. In the latter study, spines are further classified either into stubby or 'chubby', and both populations only make up to less than 18% of all spines in both the DMS and DLS[105]. Nevertheless, both studies used different criteria for spine classification. Other studies have also performed spine morphological classification based on other criteria, and often times, given that classification is often achieved semi-manually[105,111,140] or based on software criteria[104], it is unclear the exact criteria used. One study in rats, which studied spine density and morphology of MSNs (no distinction between subtype) with brightfield microscopy, used the exact same criteria for spine morphology classification[126]. However, this study only found an average spine density in both DMS and DLS of ~0.5 spines/μm, and as for spine subtypes, a higher ratio of thin spines (0.4 spines/μm), followed by stubby (0.3 spines/μm) and lastly by mushroom spines (0.1 spines/μm)[126]. Given the low spine density reported, it is unclear whether the values of the ratios of each spine subtype in this study accurately reflect the spine population.

Finally, we compared two software tools for spine reconstruction and analysis and although we could achieve reconstruction and analyze spine morphology, they both have limitations. First, we observed that Vaa3D had a lower sensitivity for spine detection, which is mostly attributed to lower detection of lower volume spines. Furthermore, Vaa3D was much more time consuming given the need to proofread every spine and the large number of false detections. Vaa3D also has several limitations regarding its outputs, given that it does not provide information on spine neck size, which precludes a morphological classification of spines as achieved with Neurolucida360. Neurolucida360, on the other hand, was faster and more unbiased, as the optimized parameters for spine detection often achieve accurate detection of all spines. Still, one parameter missing in Neurolucida360 analysis is the spine head volume, which is important since, in the hippocampus, changes in this parameter can be a proxy for synaptic strength[141].

Other limitations still exist in our current approach. Importantly, our imaging protocol could still be improved to achieve better results in the reconstruction of spine necks. We observed that in part of the spines detected, the spine neck was too dim to be efficiently detected. This might preclude an accurate morphological classification and could explain why spines classified in this work as thin spines have large head and neck diameters. We hypothesize that at least part of the spines classified as thin spines, due to incomplete neck detection throughout its length, might have larger neck diameter than expected. Enhancing the EYFP signal by performing an immunostaining against it will not only help achieve better detection of spine necks, but also allow for lower laser powers to be used during imaging. Additionally, deconvolution results can be made more accurate by measuring the actual point spread function of our setup, instead of using a theoretical one as we did, by imaging a small fluorescent bead of known dimensions[100]. This can be achieved through the software already used for deconvolution. We also speculate that the parameters used for classification might not accurately represent MSN dendritic spine morphology, despite previous studies using them[105,126], as they were achieved in hippocampal dendritic spines[125].

In this work, we show reconstruction of segments from proximal dendrites as a proof-of-concept that both the viral labelling technique, imaging and spine reconstruction can be achieved. For future experiments, ideally, we would like to image and reconstruct full neurons, or sample dendritic segments throughout the full length of the dendritic arbor, to get a complete view of spine density and morphology at both proximal and distal locations. While the first approach is possible, it is technically challenging and time consuming, and the number of neurons that can be reasonably analyzed is much lower. For instance, in the paper in which the Vaa3D spine detector plugin was published, authors reconstructed only 10 full neurons[124]. With the continuous development of better and faster confocal microscopes, whole-neuron morphological studies will be easier to perform, opening new possibilities for dendritic spine analysis.

5.5. Future perspectives

Our approach proposes a study of striatal structural plasticity upon motor skill learning, by studying dendritic spines in fixed slices of task-trained animals. With this approach, we will be able to achieve reconstruction of dendrites and/or full neurons, in both DMS and DLS populations, of c-Fos-positive and -negative neurons, in both D1- and D2-MSNs. In addition, given that the task is lateralized, we will be able to compare structural plasticity changes in the contralateral vs ipsilateral hemisphere. This will allow us to have a detailed view of spine morphology and changes upon learning in the entire dorsal striatum and infer whether motor skill learning produces changes at the spine level.

A limitation of the current approach, i.e., viral sparse labelling of MSNs only, is that we do not know what the identity of the presynaptic partner to each spine. Dorsal striatum receives input mainly from thalamical nuclei and cortical areas, such as the mediodorsal thalamic nucleus, the parafascicular thalamic nucleus, the motor cortex and the somatosensory cortex. Anatomical studies have also identified projections from secondary visual cortex, cingulate cortex, centrolateral/paracentral thalamic nucleus, external globus pallidus, and substantia nigra pars compacta[142]. Thus, it would also be important to know the origin of the presynaptic input, given that the majority of the previous studies addressing striatal inputs in skill learning have investigated the role corticostriatal connections[2,47,143], but recent evidence suggests an important role of thalamic inputs[53,54]. Different inputs should have different roles in task learning, from invigorating movement to providing information about desired outcomes.

In this current work, we describe modest increases in the number of striatal cells expressing c-Fos in task-trained animals. However, no distinction is made about D1- and D2-MSNs c-Fos-positive cells, but this could be achieved using the dopamine/ c-AMP modulated phosphoprotein Mr 32kDa (DARPP-32) and the nuclear stain TO-PRO-3. While the nuclear stain labels all cell nuclei, the DARPP-32 marker will only be expressed in MSNs. MSN population can be identified by DARPP-32 expression, and TO-PRO-3 can then be used to distinguish between D1-MSNs and D2-MSNs given that the two populations have distinct nuclear staining with this marker[144], and this approach is compatible with BrainJ.

The BrainJ pipeline also has some current limitations. While the long-term goal is to focus only on the striatal spine plasticity, whole-brain assessment of c-Fos-positive cells allows us to have a better picture of changes in plasticity upon task learning. One of the pipeline limitations is that it uses the Allen Brain Atlas Common Coordinate Framework, and thus no distinction between DMS and DLS is performed. Furthermore, the number of cells detected for each region is provided as a sum of all cells detected in that region for each hemisphere. It would be relevant to have these values for each brain slice, to further study signal distribution in the anterior-posterior axis. In the future, a more thorough study of striatal c-Fos plasticity could be achieved using semi-manual methods such as stereology, allowing for a segmentation between anterior-posterior and medial-ventral regions.

Other experiments would further complement our understanding of spine plasticity upon task learning. These could include *in vivo* approaches, such as two-photon imaging of dendritic spines in mice performing the task, which could be followed all throughout and upon training, allowing us to infer dynamic changes during task learning and skill consolidation[3]. *Ex vivo* experiments, such as acute brain slice experiments in slices from task-trained animals, would allow us to measure synaptic current amplitudes in MSNs and infer whether these correlate with spine structure, such as the spine head volume[141].

Lastly, while the work presented in this dissertation is a first step in assessing the role of striatal circuits in motor learning, it lacks evidence of what the nature of its contribution may be. Whether the striatum encodes vigor, movement kinematics, coordination, target accuracy, and/or procedural memory remains unclear. It is likely that the striatum, as well as other regions, compute in parallel different components of the skill, and different regions and molecular pathways are responsible for different aspects of it. Given the rapid expansion of tools at our disposable, more complex behaviors can now begin to be dissected using neural perturbations and recordings, as well as new behavioral analysis methods that can meaningfully organize large-scale behavioral data.

Our long-term project will provide new insights in basal ganglia circuits and how these could be modulated by and connect with other circuits, to establish, optimize and consolidate long-lasting motor skills. The importance of these underlying mechanisms is evident from neurological disorders that perturb self-initiated movements, ranging from neurodegenerative diseases such as Parkinson's and Huntington's disease, to psychiatric conditions such as obsessive-compulsive disorder. Understanding how striatal neurons compute motor skills in a normal context will allow us to further understand the circuit physiology upon dysfunction.

Bibliography

1. Gerfen, C. R. & Bolam, J. P. Chapter 1 - The Neuroanatomical Organization of the Basal Ganglia. in *Handbook of Behavioral Neuroscience* (eds. Steiner, H. & Tseng, K. Y.) vol. 24 3–32 (Elsevier, 2016).
2. Yin, H. H. *et al.* Dynamic reorganization of striatal circuits during the acquisition and consolidation of a skill. *Nat. Neurosci.* **12**, 333–341 (2009).
3. Yang, G., Pan, F. & Gan, W.-B. Stably maintained dendritic spines are associated with lifelong memories. *Nature* **462**, 920–924 (2009).
4. Kiehn, O. Decoding the organization of spinal circuits that control locomotion. *Nat. Rev. Neurosci.* **17**, 224–238 (2016).
5. Roh, J., Cheung, V. C. K. & Bizzi, E. Modules in the brain stem and spinal cord underlying motor behaviors. *J. Neurophysiol.* **106**, 1363–1378 (2011).
6. Ruder, L. & Arber, S. Brainstem Circuits Controlling Action Diversification. *Annu. Rev. Neurosci.* **42**, 485–504 (2019).
7. Klaus, A., da Silva, J. A. & Costa, R. M. What, If, and When to Move: Basal Ganglia Circuits and Self-Paced Action Initiation. *Annu. Rev. Neurosci.* **42**, null (2019).
8. Kim, J. J. & Thompson, R. F. Cerebellar circuits and synaptic mechanisms involved in classical eyeblink conditioning. *Trends Neurosci.* **20**, 177–181 (1997).
9. Bjursten, L.-M., Norrsell, K. & Norrsell, U. Behavioural repertory of cats without cerebral cortex from infancy. *Exp. Brain Res.* **25**, 115–130 (1976).
10. Arber, S. & Costa, R. M. Connecting neuronal circuits for movement. *Science* **360**, 1403–1404 (2018).
11. Parent, A. Chapter 2 - The History of the Basal Ganglia: The Nuclei. in *Handbook of Behavioral Neuroscience* (eds. Steiner, H. & Tseng, K. Y.) vol. 24 33–44 (Elsevier, 2016).
12. Wilson, C. J. Chapter 3 - The History of the Basal Ganglia: Cells and Circuits. in *Handbook of Behavioral Neuroscience* (eds. Steiner, H. & Tseng, K. Y.) vol. 24 45–62 (Elsevier, 2016).
13. Graybiel, A., Aosaki, T., Flaherty, A. & Kimura, M. The basal ganglia and adaptive motor control. *Science* **265**, 1826–1831 (1994).
14. Tepper, J. M., Abercrombie, E. D. & Bolam, J. P. Basal ganglia macrocircuits. in *Progress in Brain Research* vol. 160 3–7 (Elsevier, 2007).
15. Oorschot, D. E. Chapter 5 - Cell Types in the Different Nuclei of the Basal Ganglia. in *Handbook of Behavioral Neuroscience* (eds. Steiner, H. & Tseng, K. Y.) vol. 24 99–117 (Elsevier, 2016).
16. Joel, D. & Weiner, I. The connections of the dopaminergic system with the striatum in rats and primates: an analysis with respect to the functional and compartmental organization of the striatum. *Neuroscience* **96**, 451–474 (2000).
17. Cox, J. & Witten, I. B. Striatal circuits for reward learning and decision-making. *Nat Rev Neurosci* **20**, *482–494 (2019).*
18. Cowan, R. L. & Wilson, C. J. Spontaneous firing patterns and axonal projections of single corticostriatal neurons in the rat medial agranular cortex. *J. Neurophysiol.* **71**, 17–32 (1994).
19. Kita, T. & Kita, H. The Subthalamic Nucleus Is One of Multiple Innervation Sites for Long-Range Corticofugal Axons: A Single-Axon Tracing Study in the Rat. *J. Neurosci.* **32**, 5990–5999 (2012).
20. Jeong, M. *et al.* Comparative three-dimensional connectome map of motor cortical projections in the mouse brain. *Sci. Rep.* **6**, 20072 (2016).
21. Voorn, P., Vanderschuren, L. J. M. J., Groenewegen, H. J., Robbins, T. W. & Pennartz, C. M. A. Putting a spin on the dorsal–ventral divide of the striatum. *Trends Neurosci.* **27**, 468–474 (2004).
22. Xu, Z. C., Wilson, C. J. & Emson, P. C. Restoration of the corticostriatal projection in rat neostriatal grafts: electron microscopic analysis. *Neuroscience* **29**, 539–550 (1989).
23. Lacey, C. J. *et al.* GABAB receptors at glutamatergic synapses in the rat striatum. *Neuroscience* **136**, 1083–1095 (2005).
24. Freund, T. F., Powell, J. F. & Smith, A. D. Tyrosine hydroxylase-immunoreactive boutons in synaptic contact with identified striatonigral neurons, with particular reference to dendritic spines. *Neuroscience* **13**, 1189–1215 (1984).
25. Perrin, E. & Venance, L. Bridging the gap between striatal plasticity and learning. *Curr. Opin. Neurobiol.* **54**, 104–112 (2019).
26. Gerfen, C. R. & Scott Young, W. Distribution of striatonigral and striatopallidal peptidergic neurons in both patch and matrix compartments: an in situ hybridization histochemistry and fluorescent retrograde tracing study. *Brain Res.* **460**, 161–167 (1988).

27. Gerfen, C. *et al.* D1 and D2 dopamine receptor-regulated gene expression of striatonigral and striatopallidal neurons. *Science* **250**, 1429–1432 (1990).
28. Savasta, M., Dubois, A. & Scatton, B. Autoradiographic localization of D1 dopamine receptors in the rat brain with [3H]SCH 23390. *Brain Res.* **375**, 291–301 (1986).
29. Joyce, J. N., Loeschen, S. K. & Marshall, J. F. Dopamine D-2 receptors in rat caudate-putamen: the lateral to medial gradient does not correspond to dopaminergic innervation. *Brain Res.* **338**, 209–218 (1985).
30. Kawaguchi, Y., Wilson, C. J., Augood, S. J. & Emson, P. C. Striatal interneurones: chemical, physiological and morphological characterization. *Trends Neurosci.* **18**, 527–535 (1995).
31. Assous, M. & Tepper, J. M. Excitatory extrinsic afferents to striatal interneurons and interactions with striatal microcircuitry. *Eur. J. Neurosci.* **49**, 593–603 (2019).
32. da Silva, J. A., Tecuapetla, F., Paixão, V. & Costa, R. M. Dopamine neuron activity before action initiation gates and invigorates future movements. *Nature* **554**, 244–248 (2018).
33. Albin, R. L., Young, A. B. & Penney, J. B. The functional anatomy of basal ganglia disorders. *Trends Neurosci.* **12**, 366–375 (1989).
34. Chevalier, G., Vacher, S., Deniau, J. M. & Desban, M. Disinhibition as a basic process in the expression of striatal functions. I. The striato-nigral influence on tecto-spinal/tecto-diencephalic neurons. *Brain Res.* **334**, 215–226 (1985).
35. Alexander, G. E. & Crutcher, M. D. Functional architecture of basal ganglia circuits: neural substrates of parallel processing. *Trends Neurosci.* **13**, 266–271 (1990).
36. Kravitz, A. V. *et al.* Regulation of parkinsonian motor behaviours by optogenetic control of basal ganglia circuitry. *Nature* **466**, 622–626 (2010).
37. Cui, G. *et al.* Concurrent activation of striatal direct and indirect pathways during action initiation. *Nature* **494**, 238–242 (2013).
38. Tecuapetla, F., Jin, X., Lima, S. Q. & Costa, R. M. Complementary Contributions of Striatal Projection Pathways to Action Initiation and Execution. *Cell* **166**, 703–715 (2016).
39. Mink, J. W. The basal ganglia: focused selection and inhibition of competing motor programs. *Prog. Neurobiol.* **50**, 381–425 (1996).
40. Jin, X. & Costa, R. M. Start/stop signals emerge in nigrostriatal circuits during sequence learning. *Nature* **466**, 457–462 (2010).
41. Agostino, R., Berardelli, A., Formica, A., Accornero, N. & Manfredi, M. Sequential arm movements in patients with Parkinson's disease, Huntington's disease and dystonia. *Brain J. Neurol.* **115 (Pt 5)**, 1481–1495 (1992).
42. Geddes, C. E., Li, H. & Jin, X. Optogenetic editing reveals the hierarchical organization of learned action sequences. *Cell* **174**, 32-43.e15 (2018).
43. Matamales, M. *et al.* Local D2- to D1-neuron transmodulation updates goal-directed learning in the striatum. *Science* **367**, 549–555 (2020).
44. Peak, J., Chieng, B., Hart, G. & Balleine, B. W. Striatal direct and indirect pathway neurons differentially control the encoding and updating of goal-directed learning. *bioRxiv* 2020.02.18.955385 (2020)
45. Jurado-Parras, M.-T. *et al.* The Dorsal Striatum Energizes Motor Routines. *Curr. Biol.* **30**, 4362-4372.e6 (2020).
46. Karni, A. *et al.* The acquisition of skilled motor performance: Fast and slow experience-driven changes in primary motor cortex. *Proc. Natl. Acad. Sci.* **95**, 861 (1998).
47. Kupferschmidt, D. A., Juczewski, K., Cui, G., Johnson, K. A. & Lovinger, D. M. Parallel, but Dissociable, Processing in Discrete Corticostriatal Inputs Encodes Skill Learning. *Neuron* **96**, 476-489.e5 (2017).
48. Rueda-Orozco, P. E. & Robbe, D. The striatum multiplexes contextual and kinematic information to constrain motor habits execution. *Nat. Neurosci.* **18**, 453–460 (2015).
49. Vicente, A. M., Galvão-Ferreira, P., Tecuapetla, F. & Costa, R. M. Direct and indirect dorsolateral striatum pathways reinforce different action strategies. *Curr. Biol.* **26**, R267–R269 (2016).
50. Kravitz, A. V., Tye, L. D. & Kreitzer, A. C. Distinct roles for direct and indirect pathway striatal neurons in reinforcement. *Nat. Neurosci.* **15**, 816–818 (2012).
51. Shan, Q., Ge, M., Christie, M. J. & Balleine, B. W. The Acquisition of Goal-Directed Actions Generates Opposing Plasticity in Direct and Indirect Pathways in Dorsomedial Striatum. *J. Neurosci.* **34**, 9196–9201 (2014).
52. Lopez-Huerta, V. G. *et al.* Striatal bilateral control of skilled forelimb movement. *Cell Rep.* **34**, 108651 (2021).
53. Dhawale, A. K., Wolff, S. B. E., Ko, R. & Ölveczky, B. P. *The basal ganglia can control learned motor sequences independently of motor cortex. bioRxiv* 10.1101/827261 (2019)

54. Wolff, S. B. E., Ko, R. & Ölveczky, B. P. *Distinct roles for motor cortical and thalamic inputs to striatum during motor learning and execution*. *bioRxiv* 10.1101/825810 (2019)
55. Kawai, R. *et al.* Motor Cortex Is Required for Learning but Not for Executing a Motor Skill. *Neuron* **86**, 800–812 (2015).
56. Märtin, A. *et al.* A Spatiomolecular Map of the Striatum. *Cell Rep.* **29**, 4320-4333.e5 (2019).
57. Sheng, M. & Greenberg, M. E. The regulation and function of c-fos and other immediate early genes in the nervous system. *Neuron* **4**, 477–485 (1990).
58. Kelly, K., Cochran, B. H., Stiles, C. D. & Leder, P. Cell-specific regulation of the c-myc gene by lymphocyte mitogens and platelet-derived growth factor. *Cell* **35**, 603–610 (1983).
59. Greenberg, M. E., Ziff, E. B. & Greene, L. A. Stimulation of neuronal acetylcholine receptors induces rapid gene transcription. *Science* **234**, 80–83 (1986).
60. Yap, E.-L. & Greenberg, M. E. Activity-Regulated Transcription: Bridging the Gap between Neural Activity and Behavior. *Neuron* **100**, 330–348 (2018).
61. Murphy, H. & Worley, P. F. L-type Voltage Sensitive Calcium Channels Mediate Synaptic Activation of Immediate Early. *Neuron* **7(4)**, 625–635 (1991)
62. Malik, A. N. *et al.* Genome-wide identification and characterization of functional neuronal activity–dependent enhancers. *Nat. Neurosci.* **17**, 1330–1339 (2014).
63. West, A. E. & Greenberg, M. E. Neuronal Activity–Regulated Gene Transcription in Synapse Development and Cognitive Function. *Cold Spring Harb. Perspect. Biol.* **3**, (2011).
64. Morgan, J., Cohen, D., Hempstead, J. & Curran, T. Mapping patterns of c-fos expression in the central nervous system after seizure. *Science* **237**, 192–197 (1987).
65. Sagar, S., Sharp, F. & Curran, T. Expression of c-fos protein in brain: metabolic mapping at the cellular level. *Science* **240**, 1328–1331 (1988).
66. Lyford, G. L. *et al.* Arc, a Growth Factor and Activity-Regulated Gene, Encodes a Novel Cytoskeleton-Associated Protein That Is Enriched in Neuronal Dendrites. *Neuron* **14(2)**, 433–445 (1995)
67. Brakeman, P. R. *et al.* Homer: a protein that selectively binds metabotropic glutamate receptors. *Nature* **386**, 284–288 (1997).
68. Plath, N. *et al.* Arc/Arg3.1 Is Essential for the Consolidation of Synaptic Plasticity and Memories. *Neuron* **52**, 437–444 (2006).
69. Johnson, R. S., Spiegelman, B. M. & Papaioannou, V. Pleiotropic effects of a null mutation in the c-fos proto-oncogene. *Cell* **71**, 577–586 (1992).
70. Kleim, J. A., Lussnig, E., Schwarz, E. R., Comery, T. A. & Greenough, W. T. Synaptogenesis and FOS Expression in the Motor Cortex of the Adult Rat after Motor Skill Learning. *J. Neurosci.* **16**, 4529–4535 (1996).
71. Melia, K. R., Ryabinin, A. E., Schroeder, R., Bloom, F. E. & Wilson, M. C. Induction and habituation of immediate early gene expression in rat brain by acute and repeated restraint stress. *J. Neurosci.* **14**, 5929–5938 (1994).
72. Guzowski, J. F., Setlow, B., Wagner, E. K. & McGaugh, J. L. Experience-Dependent Gene Expression in the Rat Hippocampus after Spatial Learning: A Comparison of the Immediate-Early GenesArc, c-fos, and zif268. *J. Neurosci.* **21**, 5089–5098 (2001).
73. Cao, V. Y. *et al.* Motor Learning Consolidates Arc-Expressing Neuronal Ensembles in Secondary Motor Cortex. *Neuron* **86**, 1385–1392 (2015).
74. Hosp, J. A., Mann, S., Wegenast-Braun, B. M., Calhoun, M. E. & Luft, A. R. Region and task-specific activation of Arc in primary motor cortex of rats following motor skill learning. *Neuroscience* **250**, 557–564 (2013).
75. LaHoste, G. J., Yu, J. & Marshall, J. F. Striatal Fos expression is indicative of dopamine D1/D2 synergism and receptor supersensitivity. *Proc. Natl. Acad. Sci. U. S. A.* **90**, 7451–7455 (1993).
76. Keefe, K. A. & Gerfen, C. R. D1–D2 dopamine receptor synergy in striatum: effects of intrastriatal infusions of dopamine agonists and antagonists on immediate early gene expression. *Neuroscience* **66**, 903–913 (1995).
77. Willuhn, I. & Steiner, H. Motor Learning-Related Gene Regulation in the Striatum: Effects of Cocaine. in *The Basal Ganglia VIII* (eds. Bolam, J. P., Ingham, C. A. & Magill, P. J.) 197–207 (Springer US, 2005).
78. Willuhn, I., Sun, W. & Steiner, H. Topography of cocaine-induced gene regulation in the rat striatum: relationship to cortical inputs and role of behavioural context: Striatal gene regulation and cortical inputs. *Eur. J. Neurosci.* **17**, 1053–1066 (2003).
79. Clayton, A. L., Rose, S., Barratt, M. J. & Mahadevan, L. C. Phosphoacetylation of histone H3 on c- *fos* - and c- *jun* -associated nucleosomes upon gene activation. *EMBO J.* **19**, 3714–3726 (2000).

80. Mathis, Mackenzie. Prediction Errors Drive Learning in a Mouse Model of Motor Adaptation. Doctoral dissertation, Harvard University, Graduate School of Arts & Sciences (2017)
81.Yuste, R. *Dendritic spines*. (MIT Press, 2010).
82.Harris, K. M. & Kater, S. B. Dendritic Spines: Cellular Specializations Imparting Both Stability and Flexibility to Synaptic Function. *Annu. Rev. Neurosci.* **17**, 341–371 (1994).
83.Bernardinelli, Y., Nikonenko, I. & Muller, D. Structural plasticity: mechanisms and contribution to developmental psychiatric disorders. *Front. Neuroanat.* **8**, (2014).
84.Yuste, R. Electrical Compartmentalization in Dendritic Spines. *Annu. Rev. Neurosci.* **36**, 429–449 (2013).
85.Kennedy, M. B. Signal-Processing Machines at the Postsynaptic Density. *Science* **290**, 750–754 (2000).
86.Rao, V. R. & Finkbeiner, S. NMDA and AMPA receptors: old channels, new tricks. *Trends Neurosci.* **30**, 284–291 (2007).
87.Madison, D. V., Malenka, R. C. & Nicoll, R. A. Mechanisms Underlying Long-Term Potentiation of Synaptic Transmission. *Annu. Rev. Neurosci.* **14**, 379–397 (1991).
88.Bear, M. F. & Malenka, R. C. Synaptic plasticity: LTP and LTD. *Curr. Opin. Neurobiol.* **4**, 389–399 (1994).
89.Goldberg, J. H., Tamas, G., Aronov, D. & Yuste, R. Calcium Microdomains in Aspiny Dendrites. *Neuron* **40**, 807–821 (2003).
90.Arellano, J. I., Benavides-Piccione, R., DeFelipe, J. & Yuste, R. Ultrastructure of Dendritic Spines: Correlation Between Synaptic and Spine Morphologies. *Front. Neurosci.* **1**, 131–143 (2007).
91.Peters, A. & Kaiserman-Abramof, I. R. The small pyramidal neuron of the rat cerebral cortex. The perikaryon, dendrites and spines. *Am. J. Anat.* **127**, 321–355 (1970).
92.Matsuzaki, M. *et al.* Dendritic spine geometry is critical for AMPA receptor expression in hippocampal CA1 pyramidal neurons. *Nat. Neurosci.* **4**, 1086–1092 (2001).
93.Fifková, E. & Van Harreveld, A. Long-lasting morphological changes in dendritic spines of dentate granular cells following stimulation of the entorhinal area. *J. Neurocytol.* **6**, 211–230 (1977).
94.Araya, R., Vogels, T. P. & Yuste, R. Activity-dependent dendritic spine neck changes are correlated with synaptic strength. *Proc. Natl. Acad. Sci.* **111**, E2895–E2904 (2014).
95.Araya, R., Jiang, J., Eisenthal, K. B. & Yuste, R. The spine neck filters membrane potentials. *Proc. Natl. Acad. Sci.* **103**, 17961–17966 (2006).
96.Matsuzaki, M., Honkura, N., Ellis-Davies, G. C. R. & Kasai, H. Structural basis of long-term potentiation in single dendritic spines. *Nature* **429**, 761–766 (2004).
97.Gan, W.-B., Grutzendler, J., Wong, W. T., Wong, R. O. L. & Lichtman, J. W. Multicolor “DiOlistic” Labeling of the Nervous System Using Lipophilic Dye Combinations. *Neuron* **27**, 219–225 (2000).
98.O’Brien, J. A. & Lummis, S. C. R. Diolistics: incorporating fluorescent dyes into biological samples using a gene gun. *Trends Biotechnol.* **25**, 530–534 (2007).
99.Staffend, N. A. & Meisel, R. L. DiOlistic Labeling of Neurons in Tissue Slices: A Qualitative and Quantitative Analysis of Methodological Variations. *Front. Neuroanat.* **5**, (2011).
100. Dumitriu, D., Rodriguez, A. & Morrison, J. H. High-throughput, detailed, cell-specific neuroanatomy of dendritic spines using microinjection and confocal microscopy. *Nat. Protoc.* **6**, 1391–1411 (2011).
101. Jung, C. K. E. & Herms, J. Structural Dynamics of Dendritic Spines are Influenced by an Environmental Enrichment: An In Vivo Imaging Study. *Cereb. Cortex* **24**, 377–384 (2014).
102. Comery, T. A., Shah, R. & Greenough, W. T. Differential rearing alters spine density on medium-sized spiny neurons in the rat corpus striatum: evidence for association of morphological plasticity with early response gene expression. *Neurobiol. Learn. Mem.* **63**, 217–219 (1995).
103. Robinson, T. E. & Kolb, B. Alterations in the morphology of dendrites and dendritic spines in the nucleus accumbens and prefrontal cortex following repeated treatment with amphetamine or cocaine: Psychostimulant-induced changes in neuronal structure. *Eur. J. Neurosci.* **11**, 1598–1604 (1999).
104. Wang, J. *et al.* Alcohol Elicits Functional and Structural Plasticity Selectively in Dopamine D1 Receptor-Expressing Neurons of the Dorsomedial Striatum. *J. Neurosci.* **35**, 11634–11643 (2015).
105. Jedynak, J. P., Uslaner, J. M., Esteban, J. A. & Robinson, T. E. Methamphetamine-induced structural plasticity in the dorsal striatum: Structural plasticity in the striatum. *Eur. J. Neurosci.* **25**, 847–853 (2007).
106. Moser, M. B., Trommald, M. & Andersen, P. An increase in dendritic spine density on hippocampal CA1 pyramidal cells following spatial learning in adult rats suggests the formation of new synapses. *Proc. Natl. Acad. Sci. U. S. A.* **91**, 12673–12675 (1994).
107. Leuner, B., Falduto, J. & Shors, T. J. Associative Memory Formation Increases the Observation of Dendritic Spines in the Hippocampus. *J. Neurosci.* **23**, 659–665 (2003).
108. Frank, A. C. *et al.* Hotspots of dendritic spine turnover facilitate clustered spine addition and learning and memory. *Nat. Commun.* **9**, 422 (2018).

109. Hayashi-Takagi, A. *et al.* Labelling and optical erasure of synaptic memory traces in the motor cortex. *Nature* **525**, 333–338 (2015).
110. Hawes, S. L. *et al.* Multimodal Plasticity in Dorsal Striatum While Learning a Lateralized Navigation Task. *J. Neurosci.* **35**, 10535–10549 (2015).
111. Briones, B. A., Tang, V. D., Haye, A. E. & Gould, E. Response learning stimulates dendritic spine growth on dorsal striatal medium spiny neurons. *Neurobiol. Learn. Mem.* **155**, 50–59 (2018).
112. Paxinos, G. & Franklin, K. B. J. *The Mouse Brain in Stereotaxic Coordinates*. (Academic Press, 2001).
113. Zingg, B. *et al.* AAV-Mediated Anterograde Transsynaptic Tagging: Mapping Corticocollicular Input-Defined Neural Pathways for Defense Behaviors. *Neuron* **93**, 33–47 (2017).
114. Fenno, L. E. *et al.* Targeting cells with single vectors using multiple-feature Boolean logic. *Nat. Methods* **11**, 763–772 (2014).
115. Berke, J. D., Paletzki, R. F., Aronson, G. J., Hyman, S. E. & Gerfen, C. R. A Complex Program of Striatal Gene Expression Induced by Dopaminergic Stimulation. *J. Neurosci.* **18**, 5301–5310 (1998).
116. Baldessarini, R. J., Kula, N. S., Walton, K. G. & Borgman, R. J. Behavioral effects of apomorphine and diisobutyrylapomorphine in the mouse. *Psychopharmacology (Berl.)* **53**, 45–53 (1977).
117. Lopes, G. *et al.* Bonsai: an event-based framework for processing and controlling data streams. *Front. Neuroinformatics* **9**, (2015).
118. Ferster, C. B. & Skinner, B. F. *Schedules of reinforcement.* (Appleton-Century-Crofts, 1957).
119. Mathis, A. *et al.* DeepLabCut: markerless pose estimation of user-defined body parts with deep learning. *Nat. Neurosci.* **21**, 1281–1289 (2018).
120. Mathis, A., Schneider, S., Lauer, J. & Mathis, M. W. A Primer on Motion Capture with Deep Learning: Principles, Pitfalls, and Perspectives. *Neuron* **108**, 44–65 (2020).
121. Eiter, T. & Mannila, H. Computing Discrete Frechet Distance. Technical Report CD-TR 94/64, Christian Doppler Laboratory for Expert Systems 636-637 (1994).
122. Nyquist Calculator. *Scientific Volume Imaging B.V.* Available at: https://svi.nl/NyquistCalculator. (Accessed: 26th January 2021)
123. Botta, P. *et al.* An Amygdala Circuit Mediates Experience-Dependent Momentary Arrests during Exploration. *Cell* **183**, 605-619.e22 (2020).
124. Iascone, D. M. *et al.* Whole-Neuron Synaptic Mapping Reveals Spatially Precise Excitatory/Inhibitory Balance Limiting Dendritic and Somatic Spiking. *Neuron* **106**, 566-578.e8 (2020).
125. Harris, K. M., Jensen, F. E. & Tsao, B. Three-Dimensional Structure of Dendritic Spines and Synapses in Rat Hippocampus (CA1) at Postnatal Day 15 and Adult Ages: Implications for the Maturation of Synaptic Physiology and Long-term Potentiation. *J. Neurosci.* **12 (7)**, 2685-2705 (1992)
126. Bello-Medina, P. C., Flores, G., Quirarte, G. L., McGaugh, J. L. & Alcalá, R. A. P. Mushroom spine dynamics in medium spiny neurons of dorsal striatum associated with memory of moderate and intense training. *Proc. Natl. Acad. Sci.* **113**, E6516–E6525 (2016).
127. Li, Q. *et al.* Refinement of learned skilled movement representation in motor cortex deep output layer. *Nat. Commun.* **8**, 15834 (2017).
128. Steiner, H. & Kitai, S. T. Regulation of Rat Cortex Function by D1 Dopamine Receptors in the Striatum. *J. Neurosci.* **20**, 5449–5460 (2000).
129. Peng, H., Ruan, Z., Long, F., Simpson, J. H. & Myers, E. W. V3D enables real-time 3D visualization and quantitative analysis of large-scale biological image data sets. *Nat. Biotechnol.* **28**, 348–353 (2010).
130. Santos, F. J., Oliveira, R. F., Jin, X. & Costa, R. M. Corticostriatal dynamics encode the refinement of specific behavioral variability during skill learning. *eLife* **4**, e09423 (2015).
131. Signore, P. *et al.* An assessment of handedness in mice. *Physiol. Behav.* **49**, 701–704 (1991).
132. Collins, R. L. On the Inheritance of Handedness: I. Laterality in Inbred Mice. *J. Hered.* **59**, 9–12 (1968).
133. Jin, X., Tecuapetla, F. & Costa, R. M. Basal ganglia subcircuits distinctively encode the parsing and concatenation of action sequences. *Nat. Neurosci.* **17**, 423–430 (2014).
134. Galvão-Ferreira, P., Lipinski, M., Santos, F., Barco, A. & Costa, R. M. Skill Learning Modulates RNA Pol II Poising at Immediate Early Genes in the Adult Striatum. *eneuro* **4**, ENEURO.0074-17.2017 (2017).
135. Robertson, G. S. & Fibiger, H. C. Neuroleptics increase C-FOS expression in the forebrain: Contrasting effects of haloperidol and clozapine. *Neuroscience* **46**, 315–328 (1992).
136. Renier, N. *et al.* Mapping of Brain Activity by Automated Volume Analysis of Immediate Early Genes. *Cell* **165**, 1789–1802 (2016).
137. Fürth, D. *et al.* An interactive framework for whole-brain maps at cellular resolution. *Nat. Neurosci.* **21**, 139–149 (2018).
138. Gremel, C. & Costa, R. Premotor cortex is critical for goal-directed actions. *Front. Comput. Neurosci.* **7**, (2013).

139. Reynolds, J. N. J., Hyland, B. I. & Wickens, J. R. A cellular mechanism of reward-related learning. *Nature* **413**, 67–70 (2001).
140. Lee, K.-W. *et al.* Cocaine-induced dendritic spine formation in D1 and D2 dopamine receptor-containing medium spiny neurons in nucleus accumbens. *Proc. Natl. Acad. Sci.* **103**, 3399–3404 (2006).
141. Govindarajan, A., Israely, I., Huang, S.-Y. & Tonegawa, S. The Dendritic Branch Is the Preferred Integrative Unit for Protein Synthesis-Dependent LTP. *Neuron* **69**, 132–146 (2011).
142. Guo, Q. *et al.* Whole-brain mapping of inputs to projection neurons and cholinergic interneurons in the dorsal striatum. *PloS One* **10**, e0123381–e0123381 (2015).
143. Koralek, A. C., Jin, X., Long II, J. D., Costa, R. M. & Carmena, J. M. Corticostriatal plasticity is necessary for learning intentional neuroprosthetic skills. *Nature* **483**, 331–335 (2012).
144. Matamales, M. *et al.* Striatal Medium-Sized Spiny Neurons: Identification by Nuclear Staining and Study of Neuronal Subpopulations in BAC Transgenic Mice. *PLoS ONE* **4**, (2009).

Supplementary

Annex I

Mouse strains mentioned in this work:

Common name	**Reference**	**Strain name**	**Description (from JAX or MMRRC)**	**Alleles of interest**
C57BL6/J (wild-type)	www.jax.org/ strain/000664	C57BL/6J, also known as B6	*C57BL/6J is the most widely used inbred strain. It is commonly used as a general-purpose strain and background strain for the generation of congenics carrying both spontaneous and induced mutations. (…) C57BL/6J mice are used in a wide variety of research areas (…) C57BL/6J mice are also commonly used in the production of transgenic mice.*	Nnt$^{C57BL6/J}$
EY217 (D1-CRE)	www.mmrrc.org/ catalog/sds.php? mmrrc_id=30778	Drd1-Cre	*The transgenic mice have a modified BAC-cre injected into pronuclei of FVB/N fertilized oocytes. This transgene contains the coding sequence for Cre recombinase, followed by a polyadenylation signal to terminate the fusion transcript immediately after the recombinase gene, inserted into the mouse genomic bacterial artificial chromosome (BAC) RP23-47M2 at the ATG transcription initiation codon of the dopamine receptor D1A gene so that expression of the recombinase is driven by the regulatory sequences of the mouse gene.*	Cre
KG139 (A2A-CRE)	www.mmrrc.org/ catalog/sds.php? mmrrc_id=36158	Adora2a-Cre	*The transgenic mice have a modified BAC-cre injected into pronuclei of FVB/N fertilized oocytes. This transgene contains the coding sequence for Cre recombinase, followed by the SV40 polyadenylation signal to terminate the fusion transcript immediately after the recombinase gene, inserted into the mouse genomic bacterial artificial chromosome (BAC) RP24-238K3 at the ATG transcription initiation codon of the adenosine A2a receptor gene (Adora2a) so that expression of the reporter mRNA/protein is driven by the regulatory sequences of the mouse gene.*	Cre

Strain description information was transcribed from the The Jackson Laboratory (JAX) and/or from Mutant Mouse Resource & Research Centers (MMRRC).

Annex II

Brain regions studied in this work and their identification on the Allen Brain Atlas Common Coordinate Framework 2017:

Name	Atlas acronym	Region ID
Dorsal anterior cingulate cortex layer 1	ACAd1	935
Dorsal anterior cingulate cortex layer 2/3	ACAd23	211
Dorsal anterior cingulate cortex layer 5	ACAd5	1015
Dorsal anterior cingulate cortex layer 6a	ACAd6a	919
Dorsal anterior cingulate cortex layer 6b	ACAd6b	927
Ventral anterior cingulate cortex layer 1	ACAv1	588
Ventral anterior cingulate cortex layer 2/3	ACAv23	296
Ventral anterior cingulate cortex layer 5	ACAv5	772
Ventral anterior cingulate cortex layer 6a	ACAv6a	810
Ventral anterior cingulate cortex layer 6b	ACAv6b	819
Nucleus accumbens	ACB	56
Caudoputamen (striatum)	CP	672
Gustatory areas layer 1	GU1	36
Gustatory areas layer 2/3	GU23	180
Gustatory areas layer 4	GU4	148
Gustatory areas layer 5	GU5	187
Gustatory areas layer 6a	GU6a	638
Gustatory areas layer 6b	GU6b	662
Primary motor cortex layer 1	MOp1	320
Primary motor cortex layer 2/3	MOp23	943
Primary motor cortex layer 5	MOp5	648
Primary motor cortex layer 6a	MOp6a	844
Primary motor cortex layer 6b	MOp6b	882
Piriform cortex	PIR	961
Secondary motor cortex layer 1	SOp1	656
Secondary motor cortex layer 2/3	SOp23	962
Secondary motor cortex layer 5	SOp5	767
Secondary motor cortex layer 6a	SOp6a	1021
Secondary motor cortex layer 6b	SOp6b	1085
Primary somatosensory cortex barrel field layer 1	SSpbfd1	981
Primary somatosensory cortex barrel field layer 2/3	SSpbfd23	201
Primary somatosensory cortex barrel field layer 4	SSpbfd4	1047
Primary somatosensory cortex barrel field layer 5	SSpbfd5	1070
Primary somatosensory cortex barrel field layer 6a	SSpbfd6a	1038
Primary somatosensory cortex barrel field layer 6b	SSpbfd6b	1062
Primary somatosensory cortex lower limb layer 1	SSpll1	1030
Primary somatosensory cortex lower limb layer 2/3	SSpll23	113
Primary somatosensory cortex lower limb layer 4	SSpll4	1094
Primary somatosensory cortex lower limb layer 5	SSpll5	1128
Primary somatosensory cortex lower limb layer 6a	SSpll6a	478
Primary somatosensory cortex lower limb layer 6b	SSpll6b	510
Primary somatosensory cortex upper limb layer 1	SSpul1	450
Primary somatosensory cortex upper limb layer 2/3	SSpul23	854
Primary somatosensory cortex upper limb layer 4	SSpul4	577
Primary somatosensory cortex upper limb layer 5	SSpul5	625
Primary somatosensory cortex upper limb layer 6a	SSpul6a	945
Primary somatosensory cortex upper limb layer 6b	SSpul6b	1026
Supplemental somatosensory cortex layer 1	SSs1	873
Supplemental somatosensory cortex layer 2/3	SSs23	806

Supplemental somatosensory cortex layer 4	SSs4	1035
Supplemental somatosensory cortex layer 5	SSs5	1090
Supplemental somatosensory cortex layer 6a	SSs6a	862
Supplemental somatosensory cortex layer 6b	SSs6b	893